University of Tennessee, Knoxville
TRACE: Tennessee Research and Creative Exchange

Doctoral Dissertations | Graduate School

12-2016

Temperature Dependent Mechanical Behavior of Solid Acids

Ryan Scott Ginder
University of Tennessee, Knoxville, rginder@vols.utk.edu

Follow this and additional works at: https://trace.tennessee.edu/utk_graddiss

Part of the Other Materials Science and Engineering Commons

Recommended Citation

Ginder, Ryan Scott, "Temperature Dependent Mechanical Behavior of Solid Acids. " PhD diss., University of Tennessee, 2016.
https://trace.tennessee.edu/utk_graddiss/4136

This Dissertation is brought to you for free and open access by the Graduate School at TRACE: Tennessee Research and Creative Exchange. It has been accepted for inclusion in Doctoral Dissertations by an authorized administrator of TRACE: Tennessee Research and Creative Exchange. For more information, please contact trace@utk.edu.

To the Graduate Council:

I am submitting herewith a dissertation written by Ryan Scott Ginder entitled "Temperature Dependent Mechanical Behavior of Solid Acids." I have examined the final electronic copy of this dissertation for form and content and recommend that it be accepted in partial fulfillment of the requirements for the degree of Doctor of Philosophy, with a major in Materials Science and Engineering.

George M. Pharr, Major Professor

We have read this dissertation and recommend its acceptance:

Yanfei Gao, T.G. Nieh, Sudarsanam S. Babu

Accepted for the Council:

Carolyn R. Hodges

Vice Provost and Dean of the Graduate School

(Original signatures are on file with official student records.)

Temperature Dependent Mechanical Behavior of Solid Acids

A Dissertation Presented for the
Doctor of Philosophy
Degree
The University of Tennessee, Knoxville

Ryan Scott Ginder
December 2016

Copyright © 2016 by Ryan Scott Ginder
All rights reserved.

DEDICATION

God, family, country.

I dedicate my work to you.

ACKNOWLEDGEMENTS

None of this work would have been possible without the unwavering support of my wife Elizabeth and the invaluable guidance of my adviser Dr. George Pharr. I'd like to thank my committee members, Dr. Yanfei Gao, Dr. T. G. Nieh, and Dr. Sudarsanam Babu, for their important feedback and suggestions for the final version of this dissertation. I'd also like to thank the MSE department's Mechanical Systems Group, Doug Fielden, Larry Smith, and Danny Hackworth, and all of the many employees at Nanomechanics, Inc. for their invaluable assistance with the experimental work of this project. I'd also like to acknowledge my collaborators in Dr. Thomas Zawodzinski's Chemical and Biomolecular Engineering research group, Dr. Alexander Papandrew and David Wilson, for their assistance with raw material synthesis and sample preparation. This work was financially supported by the National Defense Science & Engineering Graduate Fellowship, the National Science Foundation through grant DMR-147812, the University of Tennessee's Bredesen Center, and the now defunct TN-SCORE center, Tennessee's former NSF EPSCoR program.

ABSTRACT

Existing literature data on the creep behavior of superprotonic solid acids, which is important for their use in fuel cell applications, is scant and unreliable. Steady state creep behavior for the model material system cesium hydrogen sulfate (CHS) is probed using nanoindentation and corroborated using uniaxial compression testing. To facilitate nanoindentation creep result interpretation, a radial flow model of power law indentation creep is developed. This model is compared with the related model from Bower, et. al. for several pre-existing literature datasets showing that the nonlinear, steady state creep law underpinning both appears valid for power law indentation creep.

TABLE OF CONTENTS

SOLID ACIDS – AN INTRODUCTION 1

Fuel Cells and their Connection to Solid Acids 1

What are Solid Acids? 5

CHS structure and conductivity 6

The importance of plastic deformation 8

Steady State Creep Deformation 10

Kislitsyn CHS Creep Study 12

Reported steady state, power law creep behavior 12

Kislitsyn creep experimental design flaws 14

References 19

CHAPTER I THE CHARACTERIZATION OF STEADY STATE CREEP VIA NANOINDENTATION 21

Abstract 22

Introduction to Nanoindentation 22

Early Experimental Measurement of Creep via Indentation 26

Radial Flow Model of Indentation Steady State Creep 27

Johnson elastic-perfectly plastic ECM theory 27

Multiaxial stress treatment of steady state creep 32

Thick-walled, creeping spherical pressure vessel 35

Indentation creep radial flow model 42

Bower's Analysis of Steady State Creep 43

Steady State Indentation Creep Theory Experimental Analysis 48
Flat punch experimental data treatment 48
Conical/Berkovich indenter experimental data treatment 52
The α/β parameter comparison 57
References 61
Appendix 63
CHAPTER II THE MEASUREMENT AND ANALYSIS OF SUPERPROTONIC CHS MECHANICAL PROPERTIES 65
Abstract 66
CHS Steady State Creep Experimentation 66
Material production and sample fabrication 67
Uniaxial compression experimental methodology 72
Nanoindentation experimental methodology 74
Uniaxial Compression Testing, Results, and Analysis 78
Preliminary testing 78
Variable displacement rate (VDR) tests 82
Constant displacement rate (CDR) tests 86
Nanoindentation Testing, Results, and Analysis 90
References 99
Appendix 100
FINAL CONCLUSIONS 110
CHS Mechanical Behavior 111

Steady State Theory of Indentation Creep 111

VITA.....113

LIST OF TABLES

Table 1. Numerical results reported by Bower [7]. 46

LIST OF FIGURES

Figure 1. Hydrogen fuel cell schematic diagram [1]. 2

Figure 2. Fuel cell operating temperature ranges [2]. 3

Figure 3. Solid acid proton conductivity jump [3].....4

Figure 4. CHS superprotonic phase transition [4]. 7

Figure 5. Kirpichnikova, et. al. CHS compression test results [9].....9

Figure 6. Schematic strain vs. time curve of creep deformation stages [10]. 11

Figure 7. Thermomechanical analyzer schematic diagram [11].....13

Figure 8. Example strain vs. time curve reported by Kislitsyn [12].....15

Figure 9. CHS power law creep (a) stress exponent and (b) relative activation energy results reported by Kislitsyn [12]. 16

Figure 10. Kislitsyn's specimens' approximate aspect ratio relative to an appropriate aspect ratio for uniaxial compression testing. 18

Figure 11. Comparison of uniaxial and nanoindentation test geometries.....25

Figure 12. Steady state impression creep measured in succinonitrile crystals using a cylindrical flat punch [5]. 28

Figure 13. ECM theory constructed from (a) Hill's expanding elastic-perfectly plastic spherical cavity then (b) cut into a hemisphere similar in geometry to indentation. 29

Figure 14. Johnson's (a) final ECM geometry used to develop equation 5 and (b) plotted against experimental indentation results [2]. 31

Figure 15. Finne and Heller's creeping spherical pressure vessel with infinite outer radius. 40
Figure 16. Geometry of a conical indent [8]. 45
Figure 17. Bower tabulated results from Tab. 1 (a) plotted as a function of inverse stress exponent (b) with polynomial fitted expressions. 47
Figure 18. Chu and Li's succinonitrile indentation data [5]. 49
Figure 19. Chu and Li's succinonitrile uniaxial compression data [5]. 50
Figure 20. Plot of succinonitrile steady state creep results: uniaxial, indentation, and indentation predicted uniaxial. 51
Figure 21. Su, et. al. amorphous selenium (a) Berkovich indentation data and (b) uniaxial compression data [8]. 53
Figure 22. Amorphous selenium creep results: uniaxial, indentation, and indentation predicted uniaxial. 54
Figure 23. Uniaxial creep experimental results in pure indium from Weertman [9]. 55
Figure 24. Indentation creep results in pure indium from Lucas and Oliver [10]. 56
Figure 25. High purity indium creep results: uniaxial, indentation, and indentation predicted uniaxial. 58
Figure 26. Plot of Bower versus radial flow model α/β parameter ratios for both a cylindrical flat punch and a 70° conical indenter. 60
Figure 27. Uniaxial test specimen cylinders, aspect ratio 2.5. 68

Figure 28. Example micrograph of polished CHS indentation specimen surface. 70
Figure 29. Thermogravimetric analysis of CHS in flowing argon corresponding to superprotonic phase decompositon [1]. 71
Figure 30. MTS 10/GL screw driven uniaxial tension and compression load frame with attached environmental chamber. 73
Figure 31. Fused silica (a) load-displacement curves, (b) Young's modulus using the calibrated area function, and (c) stiffness squared over load data. 75
Figure 32. Polycarbonate (a) load-displacement curves, (b) Young's modulus data, and (c) stiffness squared over load data. 76
Figure 33. Measured area function versus manufacturer reported. 77
Figure 34. CHS sub-superprotonic phase II stress-strain curve uniaxial CDR method measured data. 79
Figure 35. Examples in CHS below superprotonic transition of (a) double-barreling and (b) fracture. 80
Figure 36. Initial CDR measured uniaxial stress-strain data in superprotonic CHS for (a) strain rate variation and (b) temperature variation. 81
Figure 37. Initial CHS CDR creep results for (a) stress exponent with example FC compressive load and (b) activation energy with shift at superprotonic phase transition. 83
Figure 38. VDR measured uniaxial stress-strain curves for (a) 145°C, (b) 150°C, and (c) 160°C. 84

Figure 39. CHS uniaxial VDR method (a) measured creep results for stress exponent and (b) relative activation energy normalized creep results. 85

Figure 40. CDR measured uniaxial stress-strain curves for (a) 145°C, (b) 150°C, and (c) 160°C.....87

Figure 41. CHS uniaxial CDR method (a) measured creep results for stress exponent and (b) relative activation energy normalized creep results. 88

Figure 42. Phase II sub-superprotonic deutrated CHS NMR measured self-diffusion energies for hydrogen and cesium [4]. 89

Figure 43. 145°C CSR indentation $(\boldsymbol{dP/dt})/\boldsymbol{P} = \mathbf{0.200}\ \boldsymbol{s} - \mathbf{1}$: (a) $(\boldsymbol{dP/dt})/\boldsymbol{P}$, (b) load-displacement curves, (c) $(\boldsymbol{dh/dt})/\boldsymbol{h}$, and (d) nominal hardness. 91

Figure 44. Indentation versus CDR uniaxial superprotonic creep stress exponent results at (a) 145°C, (b) 150°C, and (c) 160°C. 93

Figure 45. Superprotonic CHS indentation (a) measured relative activation energy normalized results (b) compared with CDR uniaxial data using both radial flow and Bower models. 94

Figure 46. Superprotonic CHS creep relative activation energy normalized results compilation.....95

Figure 47. Superprotonic CHS indentation measured Young's modulus for (a) 145°C, (b) 150°C, and (c) 160°C. 96

Figure 48. CHS room temperature indentation measured Young's modulus. 97

Figure 49. CHS Young's modulus shift with temperature and superprotonic phase change. 98

Figure 50. 170°C stress-strain curve results for (a) the VDR method and (b) the CDR method. 101

Figure 51. 145°C CSR indentation $(\boldsymbol{dP/dt})/\boldsymbol{P} = \mathbf{0.020}\ \boldsymbol{s} - \mathbf{1}$: (a) $(\boldsymbol{dP/dt})/\boldsymbol{P}$, (b) load-displacement curves, (c) $(\boldsymbol{dh/dt})/\boldsymbol{h}$, and (d) nominal hardness. 102

Figure 52. 145°C CSR indentation $(\boldsymbol{dP/dt})/\boldsymbol{P} = \mathbf{0.002}\ \boldsymbol{s} - \mathbf{1}$: (a) $(\boldsymbol{dP/dt})/\boldsymbol{P}$, (b) load-displacement curves, (c) $(\boldsymbol{dh/dt})/\boldsymbol{h}$, and (d) nominal hardness. 103

Figure 53. 150°C CSR indentation $(\boldsymbol{dP/dt})/\boldsymbol{P} = \mathbf{0.200}\ \boldsymbol{s} - \mathbf{1}$: (a) $(\boldsymbol{dP/dt})/\boldsymbol{P}$, (b) load-displacement curves, (c) $(\boldsymbol{dh/dt})/\boldsymbol{h}$, and (d) nominal hardness. 104

Figure 54. 150°C CSR indentation $(\boldsymbol{dP/dt})/\boldsymbol{P} = \mathbf{0.020}\ \boldsymbol{s} - \mathbf{1}$: (a) $(\boldsymbol{dP/dt})/\boldsymbol{P}$, (b) load-displacement curves, (c) $(\boldsymbol{dh/dt})/\boldsymbol{h}$, and (d) nominal hardness. 105

Figure 55. 150°C CSR indentation $(\boldsymbol{dP/dt})/\boldsymbol{P} = \mathbf{0.002}\ \boldsymbol{s} - \mathbf{1}$: (a) $(\boldsymbol{dP/dt})/\boldsymbol{P}$, (b) load-displacement curves, (c) $(\boldsymbol{dh/dt})/\boldsymbol{h}$, and (d) nominal hardness. 106

Figure 56. 160°C CSR indentation $(\boldsymbol{dP/dt})/\boldsymbol{P} = \mathbf{0.200}\ \boldsymbol{s} - \mathbf{1}$: (a) $(\boldsymbol{dP/dt})/\boldsymbol{P}$, (b) load-displacement curves, (c) $(\boldsymbol{dh/dt})/\boldsymbol{h}$, and (d) nominal hardness. 107

Figure 57. 160°C CSR indentation $(\boldsymbol{dP/dt})/\boldsymbol{P} = \mathbf{0.020}\ \boldsymbol{s} - \mathbf{1}$: (a) $(\boldsymbol{dP/dt})/\boldsymbol{P}$, (b) load-displacement curves, (c) $(\boldsymbol{dh/dt})/\boldsymbol{h}$, and (d) nominal hardness. 108

Figure 58. 160°C CSR indentation $(\boldsymbol{dP/dt})/\boldsymbol{P} = \mathbf{0.002}\ \boldsymbol{s} - \mathbf{1}$: (a) $(\boldsymbol{dP/dt})/\boldsymbol{P}$, (b) load-displacement curves, (c) $(\boldsymbol{dh/dt})/\boldsymbol{h}$, and (d) nominal hardness. 109

NOMENCLATURE

A	true projected area of contact under indentation accounting for sink-in/pile-up
A_{cavity}	cross-sectional area of expanding cavity hemispherical core
$A_{indenter}$, A_{nom}	nominal projected area of contact under indentation
a	true contact radius accounting for sink-in/pile-up
a_{nom}	nominal contact radius
α	uniaxial power law creep pre-exponential
α_1	uniaxial power law creep pre-exponential without temperature dependence
β	indentation power law creep pre-exponential
β_1	indentation power law creep pre-exponential without temperature dependence
c	Bower sink-in/pile-up parameter
D	spherical indenter diameter
E, G, W	placeholder integration constants
F	Bower dimensionless contact pressure parameter
$\dot{\gamma}$	shear-strain rate
J	ratio of shear-strain rates to shear stresses
L	load on the indenter
dh	indentation depth differential
dr	radial differential

dV_{cavity}	expanding cavity hemispherical core volume differential
$dV_{indenter}$	indentation volume differential
E	Young's modulus
$\dot{\epsilon}_i$	strain rate under indentation loading
$\dot{\epsilon}_r$	radial strain rate
ϵ_t, $\epsilon_{\varphi\varphi}$	tangential strain
$\dot{\epsilon}_t$, $\dot{\epsilon}_\varphi$, $\dot{\epsilon}_\theta$	tangential strain rate
$\dot{\epsilon}_u$	strain rate under uniaxial loading
$\dot{\epsilon}_1$, $\dot{\epsilon}_2$, $\dot{\epsilon}_3$	principal axes creep strain rates
$\dot{\epsilon}^*$	von Mises characteristic creep strain rate
h	indentation depth
h_c	true indentation depth accounting for sink-in/pile-up
$\dot{h}$	indenter penetration velocity
k_B	Boltzmann's constant
m	Chu and Li model constraint factor
n	power law creep stress exponent
$\bar{p}$	uniform internal hydrostatic core pressure
p_m	indentation true mean pressure (true hardness) accounting for sink-in/pile-up
p_{nom}	indentation nominal mean pressure (nominal hardness)
Q	power law creep relative activation energy
R_i	inner cavity (core) radius

R_o	outer cavity (core) radius
r	radius
σ	true stress
σ_r	radius stress
σ_t, σ_φ, σ_θ	tangential stress
$\sigma_1, \sigma_2, \sigma_3$	principal axes stresses
σ^*	von Mises characteristic creep flow stress
T	temperature
τ	shear stress
u_r	radial displacement vector
$\dot{u}_r$	radial displacement vector time differential
u_φ	tangential displacement vector
θ	conical indenter centerline to face angle
ν	Poisson's ratio
Y	yield strength

SOLID ACIDS – AN INTRODUCTION

Fuel Cells and their Connection to Solid Acids

Fuel cells (FCs) are an active area of research and development in science and engineering. These devices convert the energy released during the formation of water into direct current electricity. The resulting clean power can be used for both stationary and mobile applications. In most FCs, a hydrogen source is flowed against the FC's internal membrane assembly where the hydrogen proton is separated from its electron by a catalyst, typically platinum. The proton proceeds through a proton only conducting electrolyte separator while the electron proceeds through an external electrical circuit. The proton and electron meet again on other side of FC membrane and combine with oxygen to produce water. This process is illustrated in Fig. 1 [1].

Today's devices, listed in Fig. 2, are classified by the conductive active layer separating the hydrogen and oxygen sources that fuel the device. Intermediate operating temperature range FCs traditionally use phosphoric acid as that layer [2]. However, solid acids could potentially replace this corrosive liquid technology with an inert, solid state device. In this operating temperature range, certain solid acids undergo a phase change into a "superprotonic" phase with substantially elevated proton conductivity. Figure 3 illustrates this dramatic, sudden jump in proton conductivity in cesium hydrogen phosphate [3]. However, only a subset of these materials actually exhibit the superprotonic phase. To understand why, it is necessary to understand what exactly solid acids are.

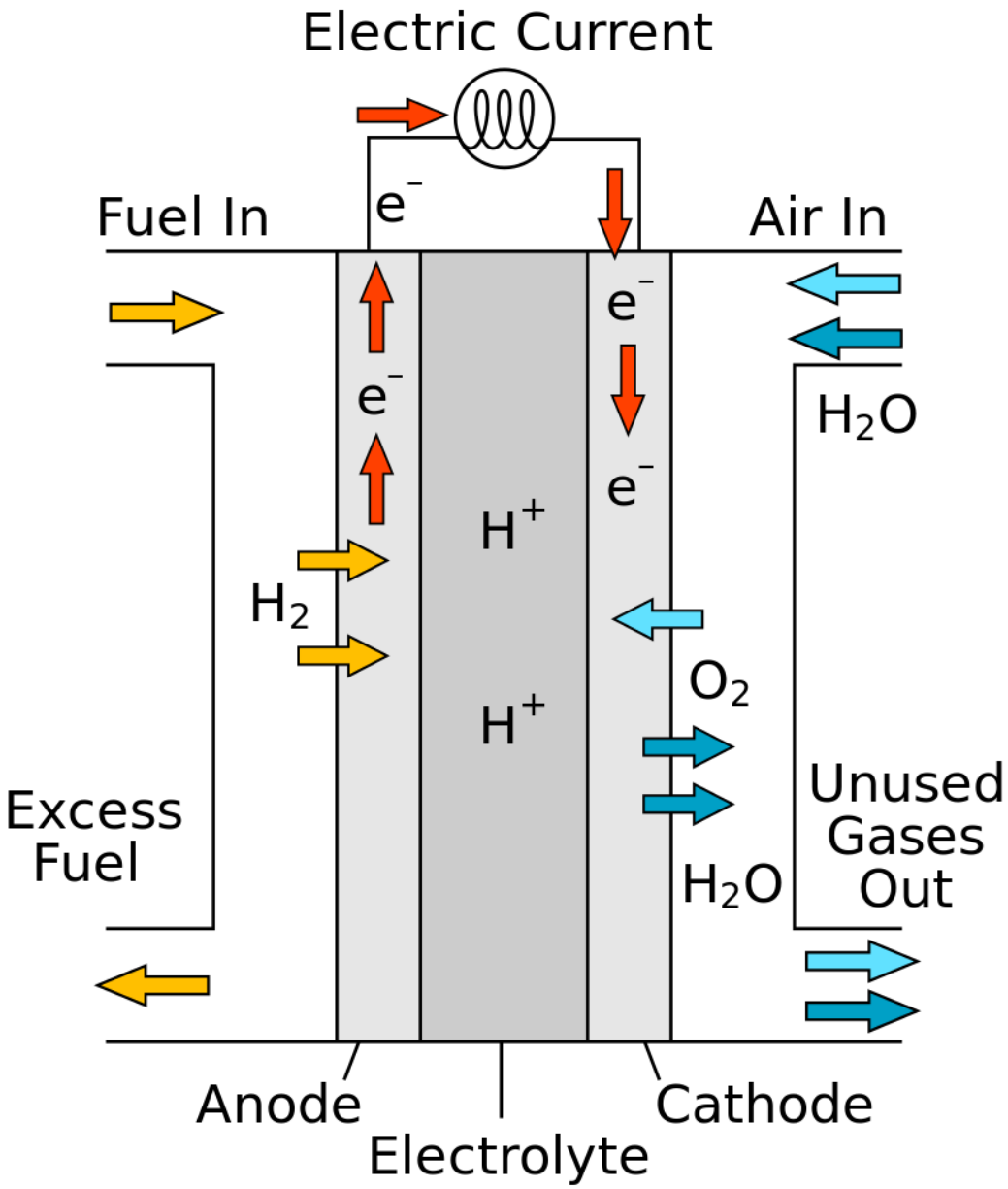

Figure 1. Hydrogen fuel cell schematic diagram [1].

Fuel Cell Type	Common Electrolyte	Operating Temperature
Polymer Electrolyte Membrane (PEM)	Perfluorosulfonic acid	<120°C
Alkaline (AFC)	Aqueous potassium hydroxide soaked in a porous matrix, or alkaline polymer membrane	<100°C
Phosphoric Acid (PAFC)	Phosphoric acid soaked in a porous matrix or imbibed in a polymer membrane	150 - 200°C
Molten Carbonate (MCFC)	Molten lithium, sodium, and/or potassium carbonates, soaked in a porous matrix	600 - 700°C
Solid Oxide (SOFC)	Yttria stabilized zirconia	500 - 1000°C

Figure 2. Fuel cell operating temperature ranges [2].

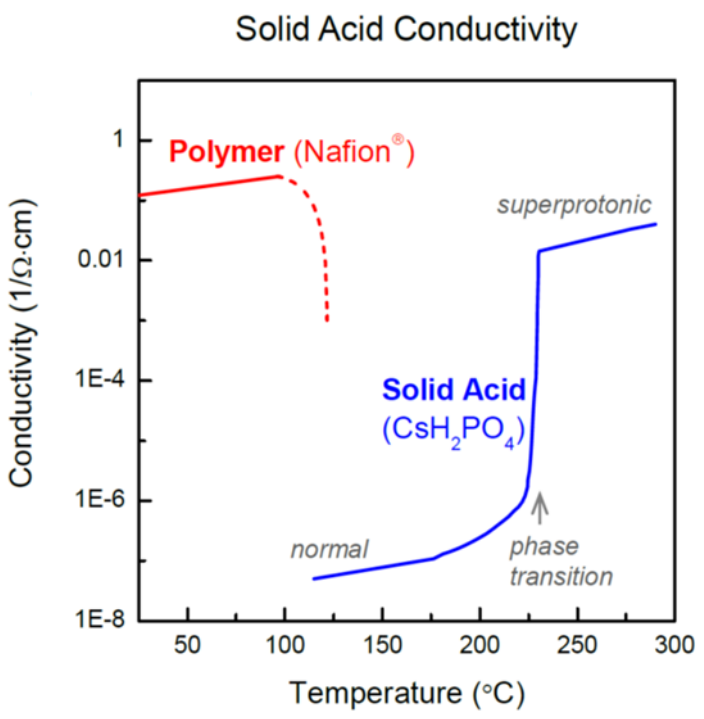

Figure 3. Solid acid proton conductivity jump [3].

What are Solid Acids?

Solid acids are, in essence, cation stabilized acids – that is salts still containing some of the hydrogen from the original acid. These materials are generally formed from acids with oxyanions and have chemical formulas such as $MHXO_4$, MH_2ZO_4, and $MHXO_4$ - MH_2ZO_4 mixtures. Typically, X = S, Se; Z = P, As; and M = Li, Na, K, NH_4, Rb, Cs [4]. In these materials a solid crystal structure is formed by a reacting acid's anion and base's cation while a secondary, ordered hydrogen bond sublattice is formed by the acid's remaining protons. The primary cation-anion lattice of solid acids with small cations (Li, Ca, etc.) generally melts before the hydrogen bond sublattice preventing the formation of a stable, solid superprotonic phase. In larger cation solid acids (Cs, Rh, etc.) though, the primary lattice bonds are strong enough that the ordered hydrogen sublattice "melts" first allowing the superprotonic phase to manifest [5]. Intermediate sized cation solid acids, such as those containing ammonium, can also potentially exhibit the superprotonic phase if the primary crystal lattice is prevented from melting by pressurizing the surrounding environment [4].

Of all of these materials, cesium hydrogen sulfate (CHS) is the most heavily studied and is used as the initial model system for superprotonic solid acids. For example, the existence of superprotonic conductivity in solid acids was first demonstrated with this material [6]. Additionally, one of the first successful demonstrations of a solid acid fuel cell was also accomplished with this material

[7]. It is fitting then that the initial quantification of solid acids' creep behavior be done using CHS as the model system.

CHS structure and conductivity

Two room temperature phases exist in CHS, both of which are monoclinic with negligible proton conductivity. When initially produced from the usual aqueous chemistry route, the heavily hydrated Phase III is produced. This phase is stable under ambient conditions and brittle in most crystallographic orientations. Phase III can however exhibit ferroplasticity under specific crystal orientations [8]. Heating above 100°C removes the excess water in Phase III leaving the dry Phase II which lacks Phase III's ferroplasticity and is completely brittle [4,9]. Phase II will reabsorb water from the air slowly converting back to Phase III if lowered back to room temperature under ambient atmosphere. If instead heated past 141°C, the Phase II hydrogen bond sublattice rapidly disorders resulting in the formation of a tetragonal superprotonic phase with high proton conductivity. The crystal structure change is illustrated in Fig. 4. This proton conductivity is achieved through a Grotthus mechanism. First, hydrogen forms a temporary bond to a sulfate tetrahedron. Second, the tetrahedron rotates dragging the proton with it. Third, the proton breaks off from current tetrahedron and binds to an adjacent one allowing for net proton translational movement through the crystal structure [4].

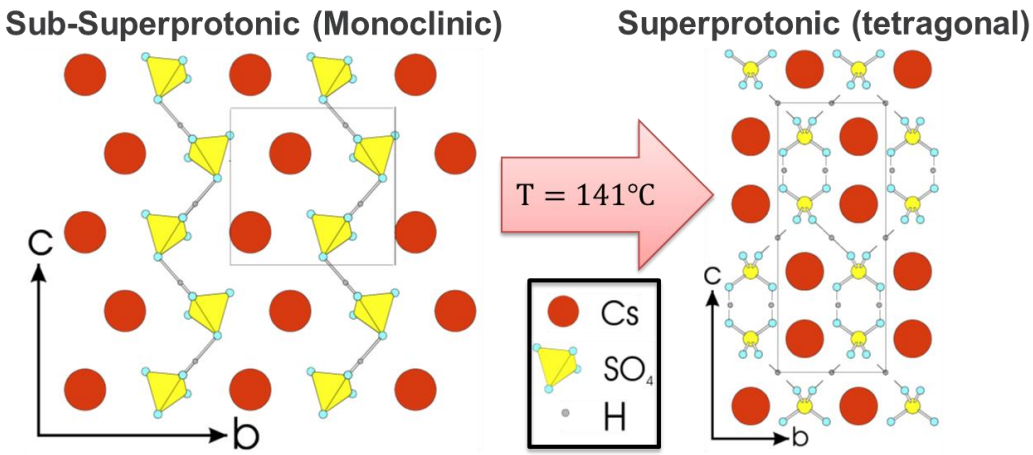

Figure 4. CHS superprotonic phase transition [4].

The importance of plastic deformation

Time dependent plasticity (i.e. creep) can pose significant problems for FCs, which usually operate under compressive loading. In a typical cell, the internal membrane assembly center containing the electrolyte layer is sandwiched between two flow plates. If able to noticeably creep, the electrolyte layer can rapidly deform during device operation resulting in regions where the fuel gases can slip through the membrane shorting the device. If severe enough, one could even blow the membrane assembly right out of the device fixture. Creep also presents issues for the electrodes at the membrane assembly surface. To operate effectively, FC electrodes are structured to maximize triple phase boundary sites where the catalyst, electron conductor, and proton conductor meet. If the proton electrolyte can easily deform over time, the percentage of triple phase boundary sites at the electrodes will decline lowering device performance.

Of all the solid acids known to have a superprotonic phase, only CHS has any published mechanical data, and even that is extremely limited. Of those few publications in existence, one of the first was performed by Kirpichnikova, et. al in 1995. In their experiments, 2.5 x 3 x 10 mm CHS Phase III single crystals grown from aqueous solution were compressed at a constant strain rate of 10^{-4} s^{-1} after heating past the superprotonic transition to 147°C. The resulting stress-strain curves in Fig. 5 provided the first quantitative evidence of large plasticity at low

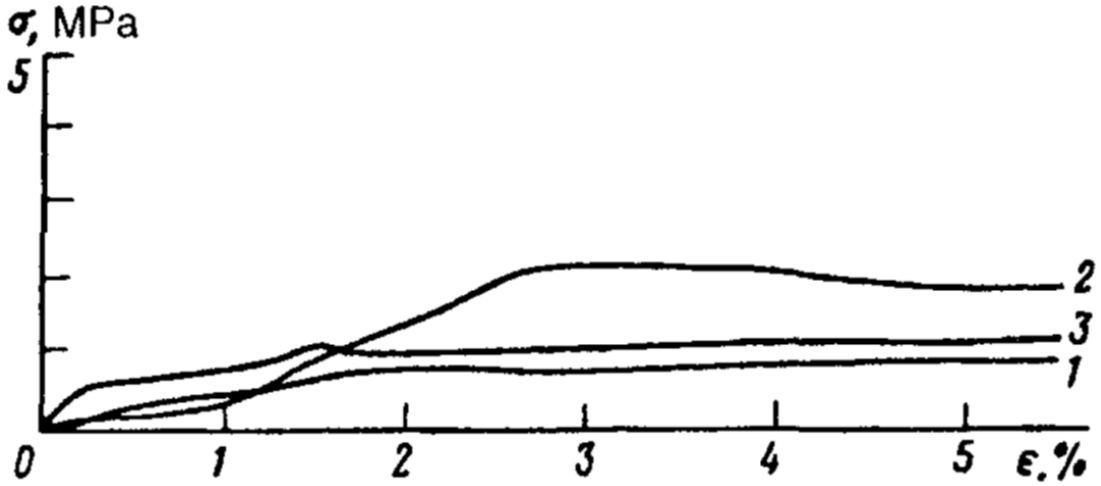

Figure 5. Kirpichnikova, et. al. CHS compression test results [9].

flow stress in solid acids [9]. This suggests time dependent plasticity could be problematic when using solid acids in engineering applications.

Steady State Creep Deformation

When one applies stress to a material, it will immediately exhibit an elastic deformation response. Once this deformation mode is exhausted however, the material can continue deforming plastically provided the applied stress is maintained for a prolonged period of time. This time dependent creep plasticity comes in three phases, as shown in Fig. 6, when under tensile loading conditions [10]. Initially, primary creep occurs where the material's strain rate starts off relatively high but rapidly declines as the material hardens. When the material's hardening processes reach equilibrium with its recovery processes, strain rate levels off, and the steady state secondary creep stage is reached. In this regime, the strain rate is a fixed number dictated by the applied stress, system temperature, and material microstructure. Secondary creep is typically the largest component of a material's time dependent strain and so a proper description of this deformation regime can be used to approximately predict material plastic deformation with time. At sufficiently low applied stresses, the relationship between strain rate and its controlling variables is well behaved and easily described using a simple power law relation of the form

$$\dot{\epsilon}_u = \alpha\sigma^n. \tag{1}$$

Here the uniaxially measured steady state strain rate $\dot{\epsilon}_u$ is controlled by the applied true flow stress σ, a pre-exponential constant α, and the creep

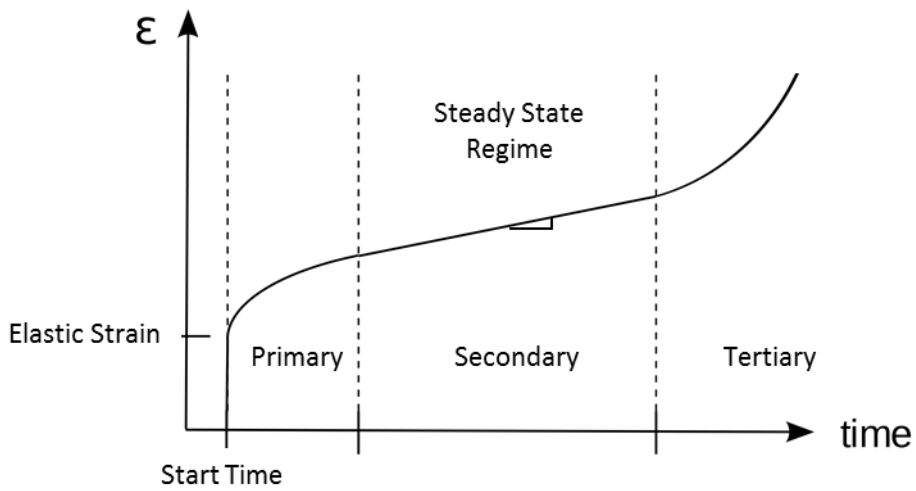

Figure 6. Schematic strain vs. time curve of creep deformation stages [10].

mechanism determined stress exponent n. The temperature dependence can be included by pulling an Arrehenius relation, dependent on relative activation energy Q, out of α leaving a primarily microstructure and testing geometry dependent pre-exponential α_1. By measuring $\dot{\epsilon}_u$'s dependence on stress and temperature, α, n, and Q can be determined through the relation

$$\dot{\epsilon}_u = \alpha_1 \sigma^n e^{-Q/k_B T}. \quad (2)$$

As the loading conditions of interest in this work are compressive only, tertiary creep can be ignored as it will not manifest under these loading conditions.

Kislitsyn CHS Creep Study

Reported steady state, power law creep behavior

The issue of creep was initially explored quantitatively by Kislitsyn in his 2009 doctoral dissertation on solid acid properties. As part of his research, Kislitsyn took several thin disc CHS specimens, similar in aspect ratio to those used for making FC membrane assemblies, and attempted to conduct traditional constant stress creep experiments using a thermomechanical analyzer, the basic design of which is shown in Figure 7 [11]. To make the test specimens, CHS powder produced via aqueous chemistry was pressed into 5.16 mm diameter by 2 - 4 mm thick discs and then thermally cycled between room temperature and 160°C to ensure all of the CHS was solely Phase II, ensuring no complications could arise from the Phase III to Phase II transition.

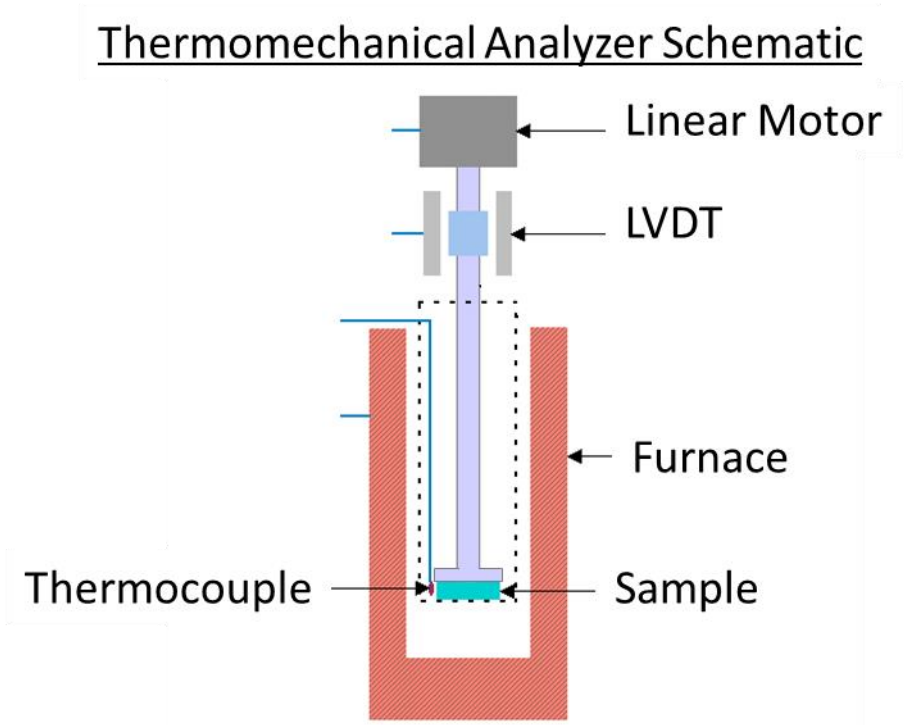

Figure 7. Thermomechanical analyzer schematic diagram [11].

The fully prepared CHS disc specimens were then loaded by the thermomechanical analyzer pusher rod with the rod's resulting displacement measured over time. An example of the resulting stress-strain curves is included in Fig. 8. Specimens were tested at a variety of loads and temperatures allowing Kislitsyn to apply a power law creep analysis to his data. While the creep data plots in the dissertation lack important information such as units, the best interpretation based on the surrounding text has been used to plot his results in Fig. 9. These plots show a stress exponent $n \cong 2.14$ and relative activation energy of $Q = 2.0\ eV$ for the superprotonic phase. Below the transition, the stress exponent was found to be $n \cong 1.01$ and the process an essentially athermal $Q \cong 0.1\ eV$. From this information, Kislitsyn suggests that grain boundary sliding is the dominate creep mechanism present in superprotonic CHS [12]. It is worth noting that by independently fitting Kislitsyn's temperature data, noticeably different answers were found from his reported activation energies. From the refitting, the sub-superprotonic monoclinic phase data yielded a small, nonsensical, positive value for activation energy slope implying tests in these region were inconclusive, and the superprotonic phase data yielded a substantially lower $Q = 0.87\ eV = 84\ kJ/mol$.

Kislitsyn creep experimental design flaws

Unfortunately, due to several unorthodox experimental design choices the interpretation of Kislitsyn's results is highly questionable. To begin with, the range of tested conditions does not even cover one order of magnitude of steady state

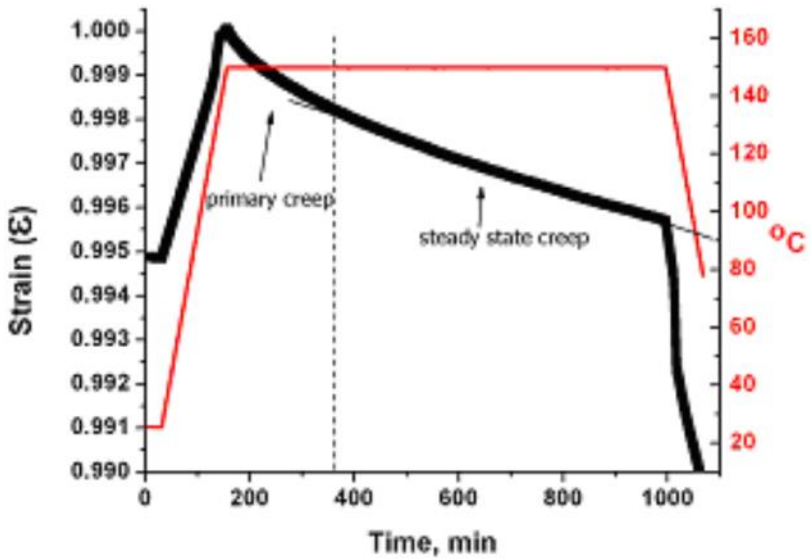

Figure 8. Example strain vs. time curve reported by Kislitsyn [12].

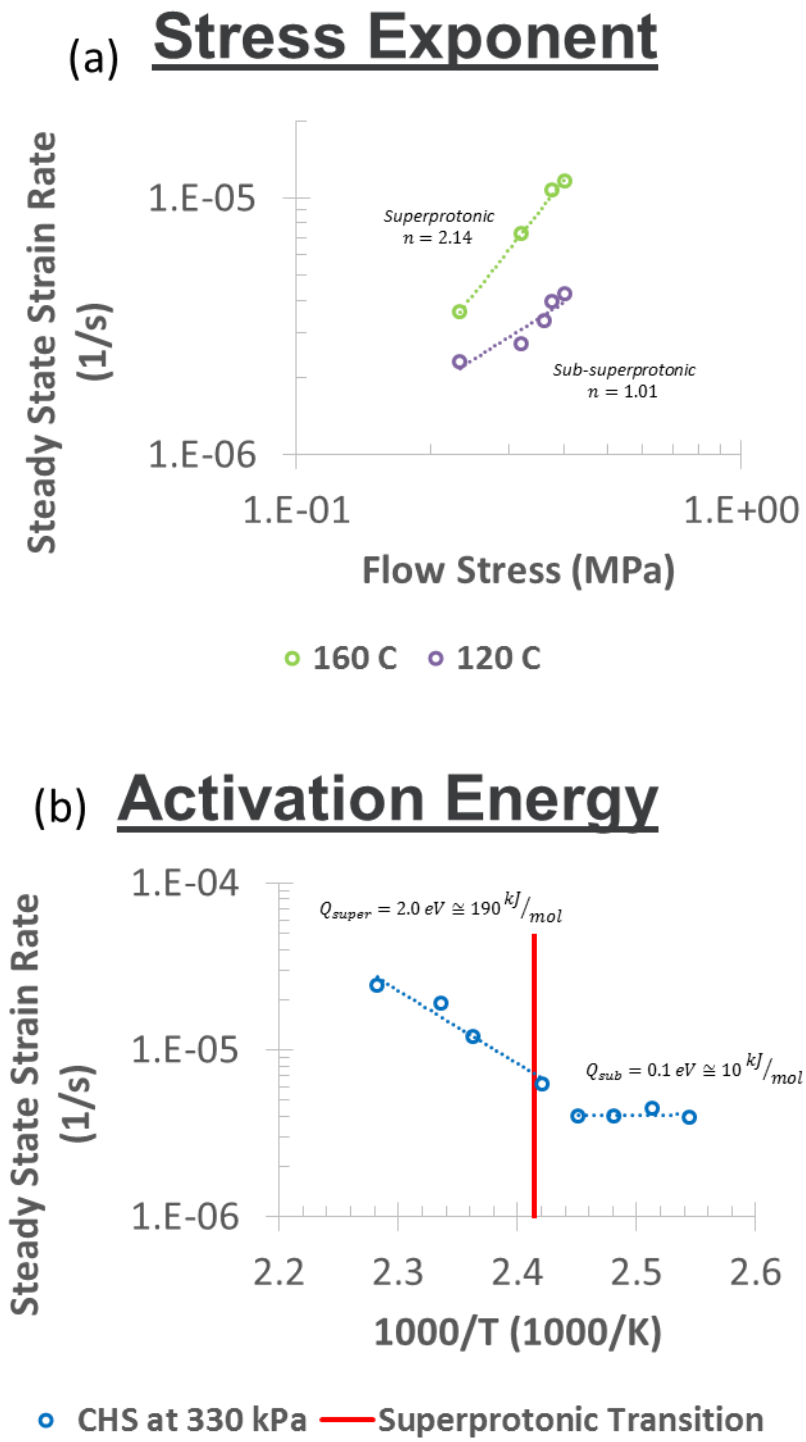

Figure 9. CHS power law creep (a) stress exponent and (b) relative activation energy results reported by Kislitsyn [12].

strain rates. Additionally, from the reported stress-strain curve in Fig. 8 it is clear the tested samples never even reached 1% strain. At such small strains, claims of steady state being achieved are inherently suspect. However, even if the samples had been allowed to further deform, Fig. 10 shows that their aspect ratios would ensure frictional forces between the platens and specimen would result in complex, nonuniform stresses dominating specimen deformation. This means a uniaxial stress analysis would be inappropriate for the resulting data. This last point of contention also means traditional uniaxial testing cannot be used to accurately measure the steady state creep behavior of the small pressed disc specimens normally used in FCs. To measure this behavior, a different characterization technique such as nanoindentation is required, or different CHS specimens with the correct aspect ratio must be manufactured.

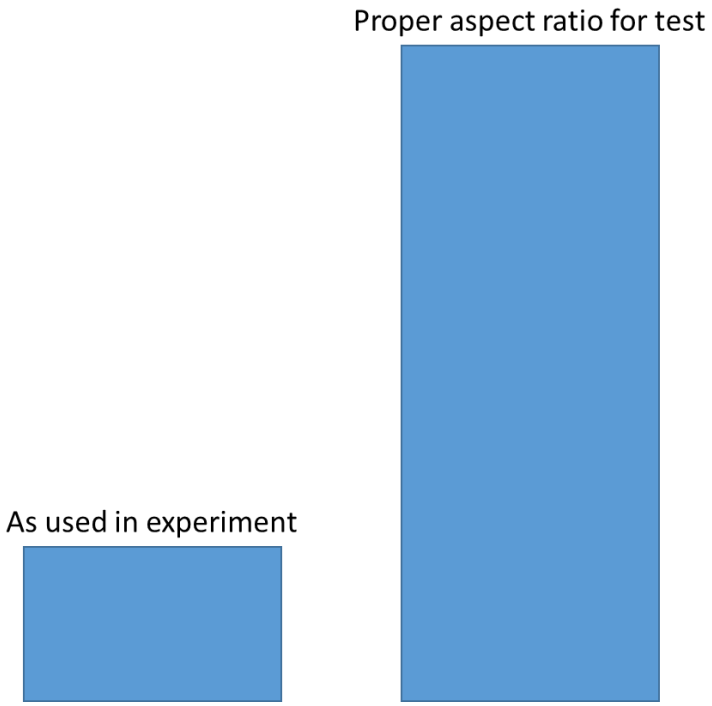

Figure 10. Kislitsyn's specimens' approximate aspect ratio relative to an appropriate aspect ratio for uniaxial compression testing.

References

[1] Dervisoglu, R. (2012). "Solid oxide fuel cell." 2016, from https://commons.wikimedia.org/wiki/File:Solid_oxide_fuel_cell_protonic.svg.

[2] Energy, U. S. D. o. (2015). "Comparison of Fuel Cell Technologies." 2016, from http://energy.gov/sites/prod/files/2015/06/f23/fcto_fuel_cells_comparison_chart.pdf.

[3] Duong, H. H. (2009). Solid Acid Fuel Cell Stack for APU Applications. 2009 DOE Hydrogen Program and Vehicle Technologies Program Annual Merit Review and Peer Evaluation Meeting. Washington, DC, U.S. Department of Energy**:** 1-30.

[4] Chisholm, C. R. I. (2003). Superprotonic Phase Transitions in Solid Acids: Parameters affecting the presence and stability of superprotonic transitions in the MHnXO4 family of compounds (X=S, SE, P, AS; M=Li, Na, K, NH4, Rb, Cs). Materials Science. Pasadena, CA, California Institute of Technology. **Ph. D.:** 290.

[5] Mhiri, T., et al. (1992). "SUPERPROTONIC PHASE-TRANSITION IN MIXED AMMONIUM CESIUM ACID SULFATE CS0.9(NH4)0.1HSO4." Journal of Alloys and Compounds 188(1-2): 215-220.

[6] Baranov, A. I., et al. (1982). "SUPERION CONDUCTIVITY AND PHASE-TRANSITIONS IN CSHSO4 AND CSHSEO4 CRYSTALS." Jetp Letters **36**(11): 459-462.

[7] Haile, S. M., et al. (2001). "Solid acids as fuel cell electrolytes." Nature **410**(6831): 910-913.

[8] Ozaki, T., et al. (1982). "PLASTIC-DEFORMATION BY TWINNING IN CSHSO4 SINGLE-CRYSTAL." Journal of the Physical Society of Japan **51**(1): 213-218.

[9] Kirpichnikova, L. F., et al. (1995). "SUPERPLASTICITY OF CSHSO4 CRYSTALS IN THE SUPERIONIC PHASE." Jetp Letters **62**(8): 638-641.

[10] Strafpeloton2 (2009). "3StageCreep." 2016, from https://commons.wikimedia.org/wiki/File:3StageCreep.svg.

[11] Cjp24 (2008). "Thermomechanical analyzer." 2016, from https://commons.wikimedia.org/wikiFile:Thermomechanical_analyzer.png.

[12] Kislitsyn, M. N. (2009). Materials Chemistry of Superprotonic Acids. Materials Science. Pasadena, CA, California Institute of Technology. **Ph. D.:** 181.

CHAPTER I

THE CHARACTERIZATION OF STEADY STATE CREEP VIA NANOINDENTATION

Abstract

K. L. Johnson's expanding cavity model (ECM) theory for elastic-perfectly plastic indentation is modified to describe power law creep of a pressurized expanding cavity and relate is to indentation. The same volume differential relation is used to derive a steady state, power law indentation creep expression valid when radial flow dominates deformation. The model is compared with the related numerical model developed by Bower, et. al. derived from the same underlying nonlinear creep law. The discussed creep models are used to predict uniaxial creep behavior from experimental indentation tests using either a cylindrical flat punch or conical equivalent Berkovich indenter. Both the radial flow and Bower models approximately match experimental data for stress exponents $n = 1 - 8$ suggesting radial flow dominates over surface flow for creep in this stress exponent regime. Although not as accurate as Bower's model, the new model has the advantage of having a simple mathematical closed form and requires no numerical approximations.

Introduction to Nanoindentation

Faster, smaller, cheaper is quickly becoming the mantra for today's material testing. With the strong push for more characterization of materials, replacing traditional uniaxial mechanical testing with more efficient methods has become an area of active interest. One prime candidate for this is nanoindentation. Nanoindentation, otherwise known as load and depth sensing

indentation, relies upon a device that applies a controlled load to drive an indenter tip into a material and measures the resulting displacement of the tip into the material's surface. Indenter shaft loading is tightly controlled by electromagnets, and displacement is precisely measured using a capacitive displacement gauge. Specialized leaf springs, stiff in the xy plane but compliant in the z direction, suppress horizontal plane motion ensuring all displacement measured is solely vertical. The indented sample is typically mounted to a motorized stage attached to the load frame assembly that also supports the indenter column. Indenter tips come in a variety of different geometries, but the most prevalently used is the triangular pyramid Berkovich tip because of its axisymmetric indent geometry and minimal surface friction.

Existing indentation deformation models center around time independent deformation. When elasticity controls deformation, indentation is described by Sneddon's theoretical equations. Sneddon used Hankel transforms of polar coordinate elastic stress equations to derive relationships connecting indenter tip profiles and elastic surface displacements. However, Sneddon's results become insufficient when plasticity becomes a significant contributor to total deformation [1]. To describe the transition region where both elastic and plastic effects are active, Johnson's expanding cavity model (ECM) theory is used. This model applies Hill's formulae for an elastic-perfectly plastic expanding spherical cavity to indentation [2]. Once plastic deformation becomes fully dominate, indentation is described through the use of slip line field theory models. Solutions are based

on the assumption of material flow along lines of maximum shear stress and exist for several indenter geometries, developed by authors such as Prandtl [3].

The most heavily used of these models for experimental science are Sneddon's elastic solutions which form the basis of the well-known Oliver-Pharr method. This method allows the use of nanoindentation load-displacement data to back out accurate measurements for both Young's modulus and hardness. Material hardness is calculated by dividing the indenter applied load by the projected area of contact between the indenter tip and the tested material's surface. This projected area of contact is not a directly measurable quantity though, so an area function connecting a tip's measurable displacement into the material's surface and its contact area at that depth must be determined first. For an initial approximation, one could use the ideal area function calculated straight from the geometry of a perfect tip. However, manufacturing defects from tip grinding/fabrication and small angular misalignments when mounting the tip usually mean the theoretical area function is not good enough for accurate results. To overcome this problem, a tip is driven into a material with well-known properties, such as fused silica, and the area function back calculated from the already known final hardness and modulus results [4].

But what of time dependent deformation such as steady state creep? Indentation tests on very small amounts of material would appear to be an attractive option for identifying and quantifying steady state creep regimes. Unfortunately, as shown in Fig. 11, the geometry of indentation tests means the

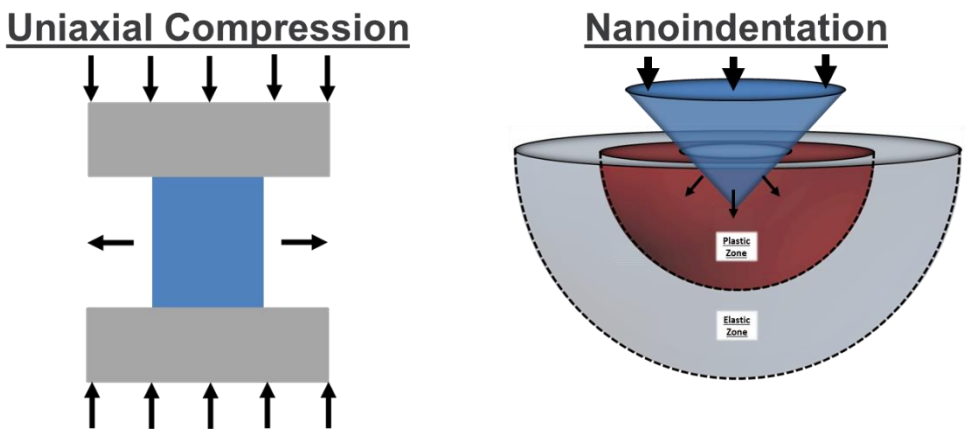

Figure 11. Comparison of uniaxial and nanoindentation test geometries.

resulting experimental data does not directly reflect the results which would be obtained from traditional uniaxial creep tests. This limits creep indentation data's use for engineering applications. Several attempts have been made to analyze indentation data using creep mechanism specific modeling, finite element simulations, and empirical fitting to limited success. As of yet, no well accepted, mechanism independent procedure for analyzing creep in indentation has been successfully demonstrated.

Early Experimental Measurement of Creep via Indentation

As mentioned earlier, the simple power law in equation 1 provides an accurate description for creep under uniaxial loading. It stands to reason that steady state creep under indentation loading should exhibit a similar power law of the form

$$\dot{\epsilon}_i = \beta (p_m)^n. \tag{3}$$

Here $\dot{\epsilon}_i$ is the indentation strain rate, β is the indentation pre-exponential factor, p_m is the mean pressure under the indenter driving deformation, and n is the material specific stress exponent just as in the uniaxial expression. What indentation strain rate actually means and how β relates to its uniaxial counterpart α remain open questions however. In order to use indentation for creep measurements, any creep theory must address these issues.

One of the first successful experimental attempts at quantifying power law creep using indentation this way was done by Chu and Li in 1977. In their experiments, they drove rigid, cylindrical flat punches under constant stress into

succinonitrile crystals. Over the course of their tests shown in Fig. 12, they observed that the indenters' penetration velocities would become constant signaling the existence of a steady state regime they referred to as "impression creep." To analyze the data, they constructed an empirical model, from finite element simulations, for the indenter's velocity $\dot{h}$ as a function of the contact pressure p_m and the indenter radius a described by the relation

$$\dot{h} = 2\alpha a \left(\frac{p_m}{m}\right)^n. \tag{4}$$

This expression can be written into the form of a strain rate equation by dividing both sides by a. Here the indentation strain rate is determined by the uniaxial material constants n and α as well as a parameter m representing something like the constraint factor present during the indentation experiment. Using data from their uniaxial compression experiments, Chu and Li determined experimentally that $m = 3.3$ for succinonitrile [5].

Radial Flow Model of Indentation Steady State Creep

Johnson elastic-perfectly plastic ECM theory

All existing ECM indentation models are built around applying Hill's elastic-plastic cavity model, illustrated in Fig. 13a, to indentation. The inspiration for this stems from the observation, shown in Fig. 13b, of numerous authors that cutting Hill's cavity in half creates an expanding hemisphere that looks remarkably similar to indentation. However, correctly correlating Hill's cavity equations with an indentation test initially proved elusive. Johnson eventually

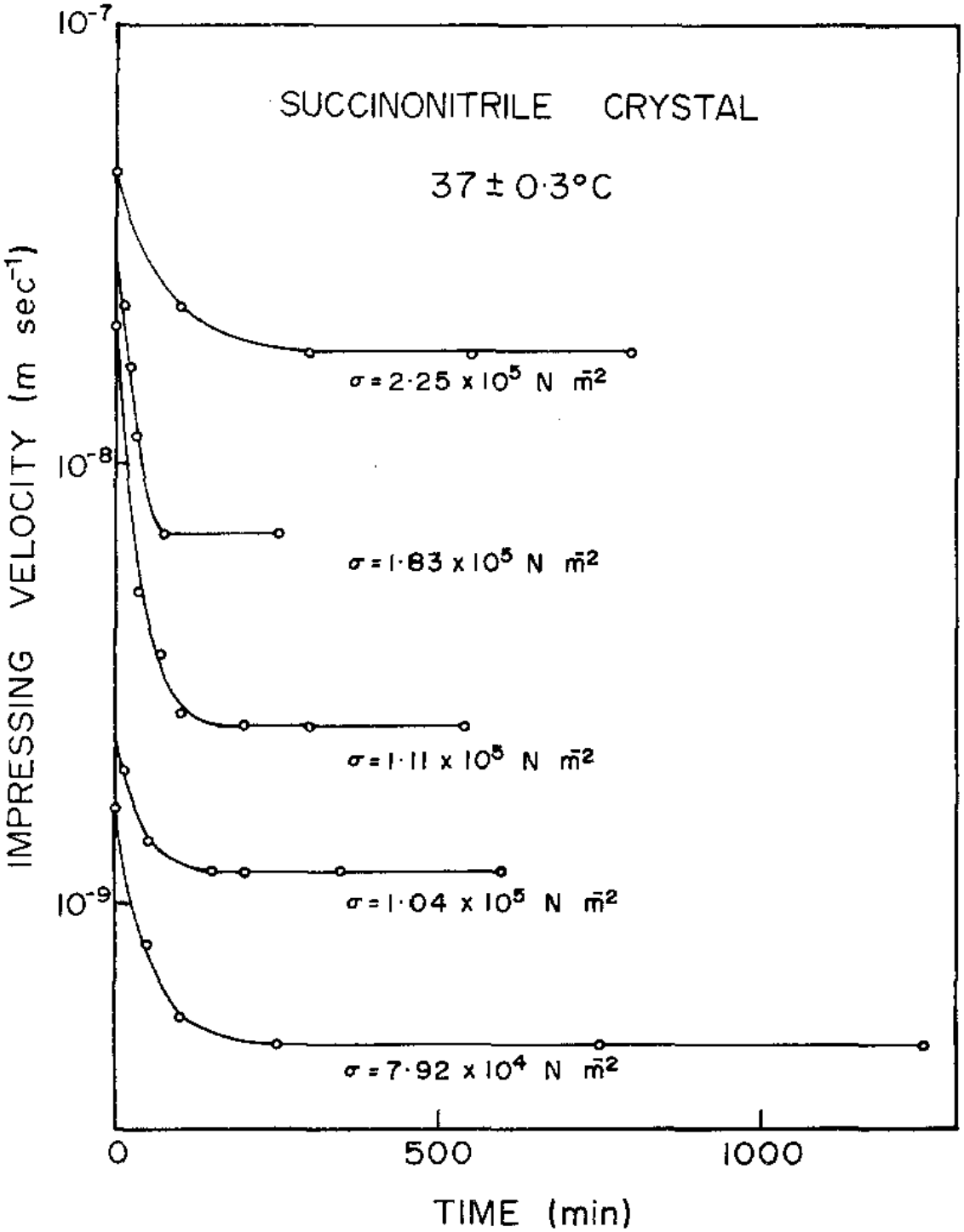

Figure 12. Steady state impression creep measured in succinonitrile crystals using a cylindrical flat punch [5].

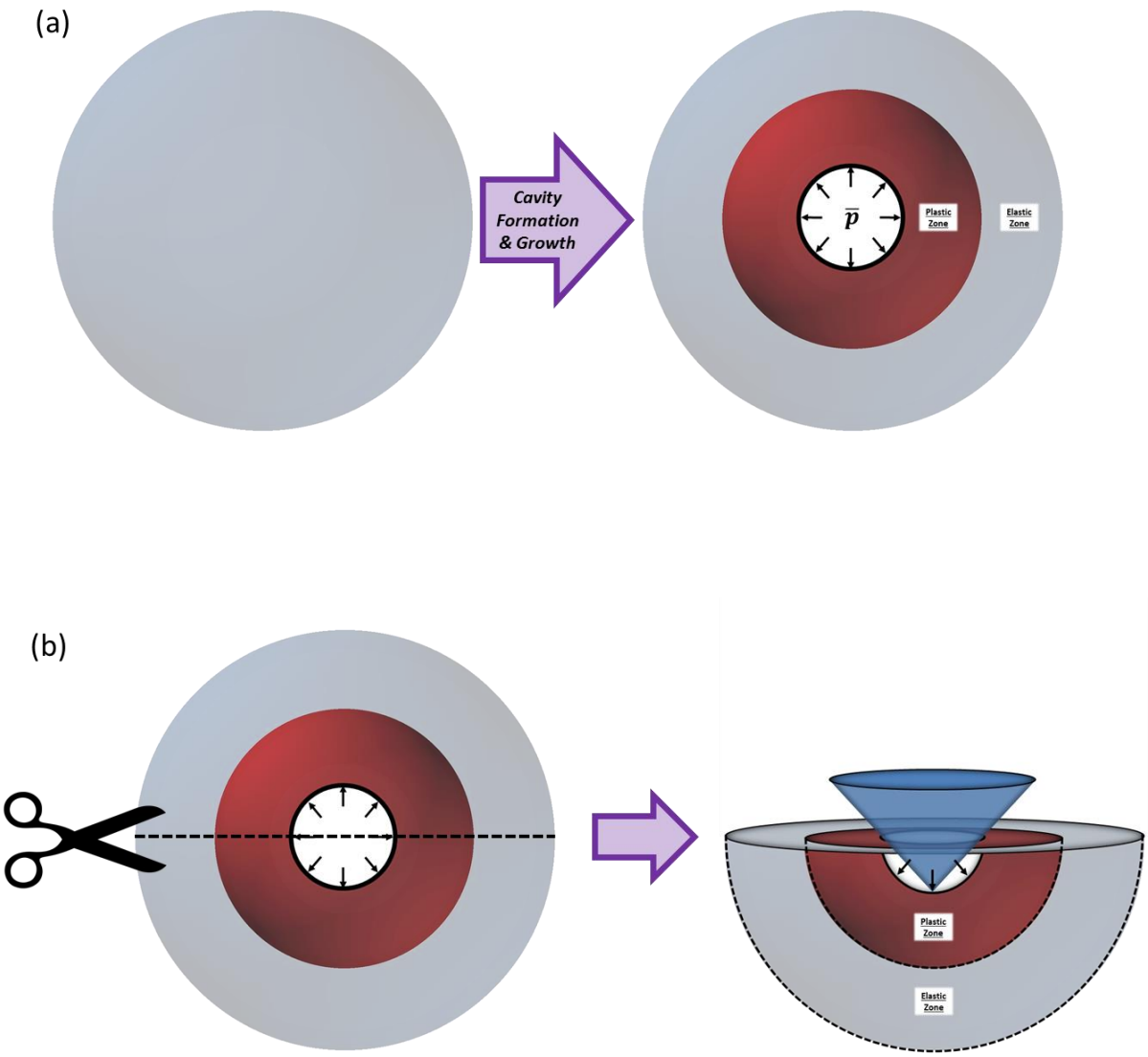

Figure 13. ECM theory constructed from (a) Hill's expanding elastic-perfectly plastic spherical cavity then (b) cut into a hemisphere similar in geometry to indentation.

solved the problem in an approximate way by setting the volume differential dV_{core} of the growing cavity equal to the $dV_{indenter}$ of material being displaced by an indenter. This final geometry, presented in Fig. 14a, allowed him to predict indentation pressures for a variety of materials provided they fell within his model's assumed elastic-plastic deformation regime.

To justify his volume differential relation, Johnson theorized that a hemispherical hydrostatic core must form around and encase the entire submerged portion of the indenter. He was able to corroborate this idea by demonstrating the formation of such a hemispherical zone in hard-drawn copper using a wedge indenter. The final size of the core resulted in it possessing the same radius as the projected contact area of the indenter ensuring $dV_{core} = dV_{indenter}$ with each increment of depth dh. This allowed Johnson to write a relationship between indenter mean pressure p_m represented by the uniform internal cavity pressure $\bar{p}$ normalized by material yield strength Y as a function of the parameter $E/(Y \tan\theta)$ where E is Young's modulus and θ is the indenter centerline to face angle. The resulting relation is

$$\frac{\bar{p}}{Y} = \frac{2}{3}\left[1 + \ln\left(\frac{1}{3}\frac{E}{Y\tan\theta}\right)\right]. \tag{5}$$

Plotting this relationship versus experimental data in Fig. 14b shows that materials deforming within the elastic-plastic regime closely agree with the elastic-plastic ECM predicted trend [2].

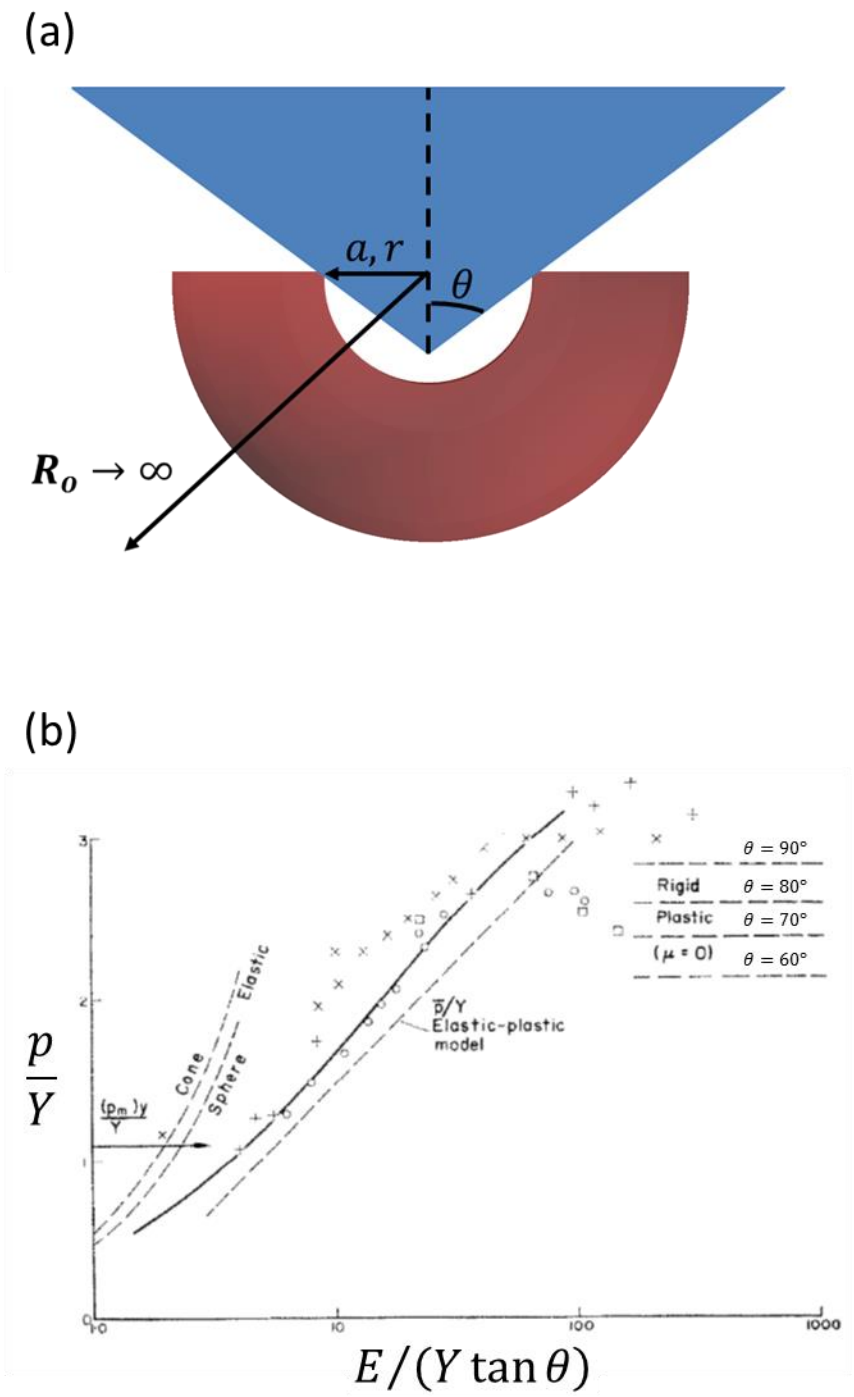

Figure 14. Johnson's (a) final ECM geometry used to develop equation 5 and (b) plotted against experimental indentation results [2].

Multiaxial stress treatment of steady state creep

Johnson's volume differential relationship is not limited only to the elastic-perfectly plastic case however. For example, as shown in the Appendix, Johnson's volume differential relationship can be applied to the case of a purely elastic indent resulting in the same predicted elastic behavior determined independently by Sneddon. More importantly though, this relationship can be adapted for steady state, time dependent behavior. This requires that a steady state creeping cavity be defined which itself requires an analysis of steady state creep under multiaxial stress. Such an analysis has already been provided by Finnie and Heller, which is extended here to describe indentation in a manner similar to Johnson. Their analysis shall be detailed below both for pedagogical reasons and to correct errors present in the formulae from the source text.

To begin, a few simplifying assumptions must be made. First, the principal axes of strain do not rotate during creep. Second, volume is conserved during plastic deformation. These allow the 3 principal strain rates to be related through

$$[(1+\epsilon_1)(1+\epsilon_2)(1+\epsilon_2)]_{plastic} = 1$$

$$[\epsilon_1 + \epsilon_2 + \epsilon_3]_{plastic} \cong 0$$

$$\dot{\epsilon}_1 + \dot{\epsilon}_2 + \dot{\epsilon}_3 = 0. \tag{6}$$

Third, the principal shear-strain rates are proportional to principle shear stresses by a constant J, as given by the relation

$$\frac{\dot{\gamma}}{\tau} = \frac{\dot{\epsilon}_1 - \dot{\epsilon}_2}{\sigma_1 - \sigma_2} = \frac{\dot{\epsilon}_2 - \dot{\epsilon}_3}{\sigma_2 - \sigma_3} = \frac{\dot{\epsilon}_3 - \dot{\epsilon}_1}{\sigma_3 - \sigma_1} = J. \tag{7}$$

J is constant at a given point in a stressed body, but may vary from point to point in the body and may change during the test. Fourth, the stressed body's mechanical properties are isotropic.

Starting with equations 6 and 7, a constitutive law equation for power law creep can begin to be developed as follows

$$\dot{\epsilon}_1 + \dot{\epsilon}_2 + \dot{\epsilon}_3 = 0$$

$$\dot{\epsilon}_1 = -\dot{\epsilon}_2 - \dot{\epsilon}_3$$

$$\dot{\epsilon}_1 + 2\dot{\epsilon}_1 = (\dot{\epsilon}_1 - \dot{\epsilon}_2) - (\dot{\epsilon}_3 - \dot{\epsilon}_1)$$

$$3\dot{\epsilon}_1 = J(\sigma_1 - \sigma_2) - C(\sigma_3 - \sigma_1)$$

$$\dot{\epsilon}_1 = \frac{J}{3}[\sigma_1 - \sigma_2 - \sigma_3 + \sigma_1]$$

$$\dot{\epsilon}_1 = \frac{J}{3}[2\sigma_1 - (\sigma_2 + \sigma_3)]$$

$$\dot{\epsilon}_1 = \frac{2}{3}J\left[\sigma_1 - \frac{1}{2}(\sigma_2 + \sigma_3)\right] \tag{8-1}$$

$$\dot{\epsilon}_2 = \frac{2}{3}J\left[\sigma_2 - \frac{1}{2}(\sigma_3 + \sigma_1)\right] \tag{8-2}$$

$$\dot{\epsilon}_3 = \frac{2}{3}J\left[\sigma_3 - \frac{1}{2}(\sigma_1 + \sigma_2)\right]. \tag{8-3}$$

In order to have a complete constitutive relationship, J must be determined. To do so, a stress σ^* and strain rate $\dot{\epsilon}^*$ are defined as the characteristic creep stress and strain rate achieved under a Von Mises flow criterion. These are given by

$$\sigma^* = \frac{1}{\sqrt{2}}[(\sigma_1 - \sigma_2)^2 + (\sigma_2 - \sigma_3)^2 + (\sigma_3 - \sigma_1)^2]^{1/2}$$

$$\epsilon^* = \frac{\sqrt{2}}{3}[(\epsilon_1 - \epsilon_2)^2 + (\epsilon_2 - \epsilon_3)^2 + (\epsilon_3 - \epsilon_1)^2]^{1/2}$$

$$\dot{\epsilon}^* = \frac{\sqrt{2}}{3}[(\dot{\epsilon}_1 - \dot{\epsilon}_2)^2 + (\dot{\epsilon}_2 - \dot{\epsilon}_3)^2 + (\dot{\epsilon}_3 - \dot{\epsilon}_1)^2]^{1/2}.$$

Under uniaxial conditions $\sigma_1 = \sigma^*, \sigma_2 = \sigma_3 = 0, \dot{\epsilon}_1 = \dot{\epsilon}^*$, which when inserted into equation 8-1, results in a definition for J in terms of characteristic stress and strain rate. This develops into the relation

$$\dot{\epsilon}_1 = \frac{2}{3}J\left[\sigma_1 - \frac{1}{2}(\sigma_2 + \sigma_3)\right]$$

$$\dot{\epsilon}^* = \frac{2}{3}J\left[\sigma^* - \frac{1}{2}(0 + 0)\right]$$

$$J = \frac{3}{2}\frac{\dot{\epsilon}^*}{\sigma^*}. \tag{9}$$

With J now defined in terms of characteristic creep strain rate and stress, one can apply a creep power law relationship to obtain the needed generalized, nonlinear creep law governing deformation. This law can be applied to equations 8-1,2,3 to determine the principal creep shear strain rates using [6]

$$\dot{\epsilon}^* = \alpha(\sigma^*)^n. \tag{10}$$

This then gives

$$J = \frac{3}{2}\frac{\dot{\epsilon}^*}{\sigma^*}$$

$$J = \frac{3}{2}\frac{\alpha(\sigma^*)^n}{\sigma^*}$$

$$J = \frac{\dot{\gamma}}{\tau} = \frac{3}{2}\alpha(\sigma^*)^{n-1} \tag{11}$$

$$\dot{\epsilon}_1 = \alpha(\sigma^*)^{n-1}\left[\sigma_1 - \frac{1}{2}(\sigma_2 + \sigma_3)\right] \tag{12-1}$$

$$\dot{\epsilon}_2 = \alpha(\sigma^*)^{n-1}\left[\sigma_2 - \frac{1}{2}(\sigma_3 + \sigma_1)\right] \tag{12-2}$$

$$\dot{\epsilon}_3 = \alpha(\sigma^*)^{n-1}\left[\sigma_3 - \frac{1}{2}(\sigma_1 + \sigma_2)\right]. \tag{12-3}$$

Thick-walled, creeping spherical pressure vessel

For a spherical pressure vessel with constant internal pressure, stress and strain rate conditions are defined as follows using a spherical coordinate geometry:

$$\sigma_1 \equiv \sigma_\theta = \sigma_t \qquad \dot{\epsilon}_1 \equiv \dot{\epsilon}_\theta = \dot{\epsilon}_t \qquad R_o \equiv \text{outer radius of body}$$

$$\sigma_2 \equiv \sigma_\varphi = \sigma_t \qquad \dot{\epsilon}_2 \equiv \dot{\epsilon}_\varphi = \dot{\epsilon}_t \qquad R_i \equiv \text{inner radius of vessel}$$

$$\sigma_3 \equiv \sigma_r \qquad \dot{\epsilon}_3 \equiv \dot{\epsilon}_r \qquad \bar{p} \equiv \text{internal cavity pressure.}$$

Using these conditions with volume conservation of equation 6, a relationship between tangential and radial strain can be defined. This relation can be further extended using strain rate compatibility to obtain an equation with tangential strain rate solely in terms of radius r of the form

$$\dot{\epsilon}_1 + \dot{\epsilon}_2 + \dot{\epsilon}_3 = 0$$

$$\dot{\epsilon}_r + \dot{\epsilon}_t + \dot{\epsilon}_t = 0$$

$$\dot{\epsilon}_r = -2\dot{\epsilon}_t \tag{13}$$

$$r\frac{d\dot{\epsilon}_t}{dr} = \dot{\epsilon}_r - \dot{\epsilon}_t$$

$$r\frac{d\dot{\epsilon}_t}{dr} = -3\dot{\epsilon}_t$$

$$\int \frac{d\dot{\epsilon}_t}{\dot{\epsilon}_t} = -3\int \frac{dr}{r}$$

$$\ln \dot{\epsilon}_t = -3\ln r + \ln W$$

$$\dot{\epsilon}_t = \frac{W}{r^3}. \tag{14}$$

Next, the spherical cavity stress and strain rate definitions are applied to the earlier defined Von Mises flow criterion to develop equations for characteristic creep stress and strain rate, respectively, giving

$$\sigma^* = \frac{1}{\sqrt{2}}\left[(\sigma_1 - \sigma_2)^2 + (\sigma_2 - \sigma_3)^2 + (\sigma_3 - \sigma_1)^2\right]^{1/2}$$

$$\sigma^* = \frac{1}{\sqrt{2}}\left[(\sigma_t - \sigma_t)^2 + (\sigma_t - \sigma_r)^2 + (\sigma_r - \sigma_t)^2\right]^{1/2}$$

$$\sigma^* = \frac{1}{\sqrt{2}}\left[2(\sigma_t - \sigma_r)^2\right]^{1/2}$$

$$\sigma^* = \sigma_t - \sigma_r \tag{15}$$

$$\dot{\epsilon}^* = \frac{\sqrt{2}}{3}\left[(\dot{\epsilon}_1 - \dot{\epsilon}_2)^2 + (\dot{\epsilon}_2 - \dot{\epsilon}_3)^2 + (\dot{\epsilon}_3 - \dot{\epsilon}_1)^2\right]^{1/2}$$

$$\dot{\epsilon}^* = \frac{\sqrt{2}}{3}\left[(\dot{\epsilon}_t - \dot{\epsilon}_t)^2 + (\dot{\epsilon}_t - \dot{\epsilon}_r)^2 + (\dot{\epsilon}_r - \dot{\epsilon}_t)^2\right]^{1/2}$$

$$\dot{\epsilon}^* = \frac{\sqrt{2}}{3}\left[2(\dot{\epsilon}_t - \dot{\epsilon}_r)^2\right]^{1/2}$$

$$\dot{\epsilon}^* = \frac{\sqrt{2}}{3}\left[2(3\dot{\epsilon}_t)^2\right]^{1/2}$$

$$\dot{\epsilon}^* = 2\dot{\epsilon}_t = 2\frac{W}{r^3}. \tag{16}$$

With the characteristic creep stress and strain rate now defined, a general expression for radial stress can be constructed. Doing so requires applying force equilibrium to equations 10, 15, and 16, or

$$r\left(\frac{d\sigma_r}{dr}\right) = 2(\sigma_t - \sigma_r)$$

$$d\sigma_r = 2\sigma^*\left(\frac{dr}{r}\right)$$

$$d\sigma_r = 2\left(\frac{\dot{\epsilon}^*}{\alpha}\right)^{1/n}\left(\frac{dr}{r}\right)$$

$$d\sigma_r = 2\left[\frac{2\frac{W}{r^3}}{\alpha}\right]^{1/n}\left(\frac{dr}{r}\right)$$

$$d\sigma_r = (2)^{1/n+1}\left(\frac{W}{\alpha}\right)^{1/n}\frac{dr}{r^{(3/n+1)}}$$

$$\int d\sigma_r = \int \frac{Gdr}{r^{(3/n+1)}}$$

$$\sigma_r = \frac{G}{r^{3/n}} + E.$$

The constants D and E can be solved for by applying the following boundary conditions for radial stress σ_r. These conditions yield the final equation for radial stress as a function of pressure vessel geometry and internal pressure.

Condition 1: $\sigma_r|_{r=R_o} = 0$

$$\sigma_r = \frac{G}{r^{3/n}} + E$$

$$0 = \frac{G}{(R_o)^{3/n}} + E$$

$$E = -\frac{G}{(R_o)^{3/n}}$$

Condition 2: $\sigma_r|_{r=R_i} = -\bar{p}$

$$\sigma_r = \frac{G}{r^{3/n}} + E$$

$$-\bar{p} = \frac{G}{(R_i)^{3/n}} + E$$

$$-\bar{p} = \frac{G}{(R_i)^{3/n}} - \frac{G}{(R_o)^{3/n}}$$

$$D = \frac{-\bar{p}(R_o R_i)^{3/n}}{{R_o}^{3/n} - {R_i}^{3/n}}$$

$$\sigma_r = \frac{G}{r^{3/n}} + E$$

$$\sigma_r = \frac{\left\{\frac{-\bar{p}(R_o R_i)^{3/n}}{{R_o}^{3/n} - {R_i}^{3/n}}\right\}}{r^{3/n}} + \left\{-\frac{\left[\frac{-\bar{p}(R_o R_i)^{3/n}}{{R_o}^{3/n} - {R_i}^{3/n}}\right]}{(R_o)^{3/n}}\right\}$$

$$\sigma_r = \frac{-\bar{p}[R_o R_i]^{3/n} - \left[-\bar{p}(R_i r)^{3/n}\right]}{\left[{R_o}^{3/n} - {R_i}^{3/n}\right] r^{3/n}}$$

$$\sigma_r = -\bar{p}\left[\frac{\left(\frac{R_o R_i}{r}\right)^{3/n} - {R_i}^{3/n}}{{R_o}^{3/n} - {R_i}^{3/n}}\right]$$

$$\sigma_r = -\bar{p}\left[\frac{\left(\frac{R_o}{r}\right)^{3/n} - 1}{\left({R_o}^{3/n} - {R_i}^{3/n}\right){R_i}^{-3/n}}\right]$$

$$\sigma_r = -\bar{p}\left[\frac{\left(\frac{R_o}{r}\right)^{3/n} - 1}{\left(\frac{R_o}{R_i}\right)^{3/n} - 1}\right] \tag{17}$$

By inserting equation 17 back into the force equilibrium equation, an expression for tangential stress σ_t can also be derived as follows

$$r\left(\frac{d\sigma_r}{dr}\right) = 2(\sigma_t - \sigma_r)$$

$$\sigma_t = \sigma_r + \frac{r}{2}\frac{d\sigma_r}{dr}$$

$$\sigma_t = \left\{-\bar{p}\frac{\left(\frac{R_o}{r}\right)^{3/n} - 1}{\left(\frac{R_o}{R_i}\right)^{3/n} - 1}\right\} + \frac{r}{2}\left\{\frac{3\bar{p}\left(\frac{R_o}{r}\right)^{3/n}}{rn\left[\left(\frac{R_o}{R_i}\right)^{3/n} - 1\right]}\right\}$$

$$\sigma_t = -\bar{p}\left\{\frac{\left(\frac{R_o}{r}\right)^{3/n} - 1}{\left(\frac{R_o}{R_i}\right)^{3/n} - 1} - \frac{3\left(\frac{R_o}{r}\right)^{3/n}}{2n\left[\left(\frac{R_o}{R_i}\right)^{3/n} - 1\right]}\right\}$$

$$\sigma_t = -\bar{p}\left[\frac{\left(\frac{R_o}{r}\right)^{3/n} - 3\left(\frac{R_o}{r}\right)^{3/n}(2n)^{-1} - 1}{\left(\frac{R_o}{R_i}\right)^{3/n} - 1}\right]$$

$$\sigma_t = -\bar{p}\left[\frac{\left(\frac{R_o}{r}\right)^{3/n}\left(1 - \frac{3}{2n}\right) - 1}{\left(\frac{R_o}{R_i}\right)^{3/n} - 1}\right]$$

$$\sigma_t = \bar{p}\left[\frac{\left(\frac{3-2n}{2n}\right)\left(\frac{R_o}{r}\right)^{3/n} + 1}{\left(\frac{R_o}{R_i}\right)^{3/n} - 1}\right]. \tag{18}$$

Equations 17 and 18 can be adapted to describe a spherical, uniformly pressurized cavity in an infinite medium, illustrated in Fig. 15, by setting $R_o = \infty$ (that is $\frac{R_o}{R_i} \gg 1$). This gives

$$\sigma_r = -\bar{p}\left[\frac{\left(\frac{R_o}{r}\right)^{3/n} - 1}{\left(\frac{R_o}{R_i}\right)^{3/n} - 1}\right]$$

$$\sigma_r = -\bar{p}\left[\left(\frac{R_o}{r}\right)^{3/n}\left(\frac{R_i}{R_o}\right)^{3/n}\right]$$

$$\sigma_r = -\bar{p}\left(\frac{R_i}{r}\right)^{3/n} \tag{19}$$

$$\sigma_t = \bar{p}\left[\frac{\left(\frac{3-2n}{2n}\right)\left(\frac{R_o}{r}\right)^{3/n} + 1}{\left(\frac{R_o}{R_i}\right)^{3/n} - 1}\right]$$

$$\sigma_t = \bar{p}\left[\left(\frac{3-2n}{2n}\right)\left(\frac{R_o}{r}\right)^{3/n}\left(\frac{R_i}{R_o}\right)^{3/n}\right]$$

$$\sigma_t = \bar{p}\left(\frac{3-2n}{2n}\right)\left(\frac{R_i}{r}\right)^{3/n}. \tag{20}$$

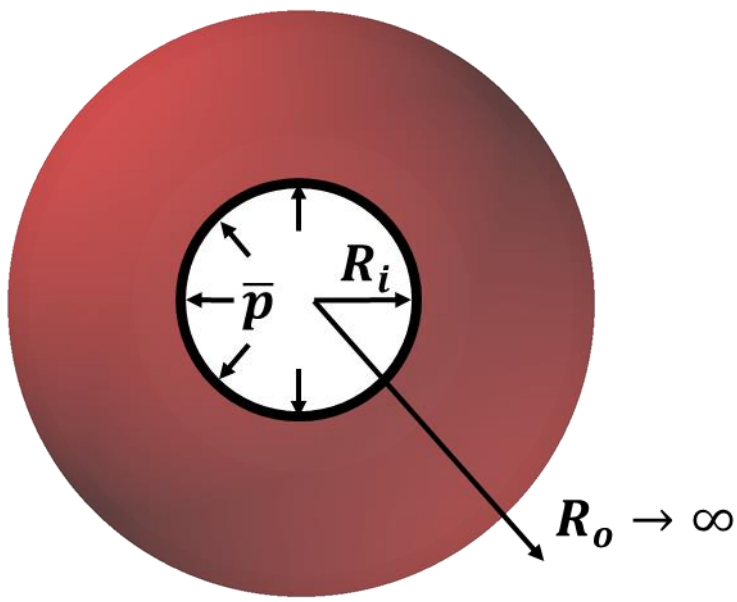

Figure 15. Finne and Heller's creeping spherical pressure vessel with infinite outer radius.

With all the parts now assembled, an expression for tangential strain rate $\dot{\epsilon}_t$ in terms of internal pressure $\bar{p}$, radius r, stress exponent n, and creep uniaxial coefficient α can be developed. Starting with constitutive relationship 12-1 and substituting in equations 15, 19, and 20, the tangential strain rate from the pressurized cavity's surface out to infinity is obtained by

$$\dot{\epsilon}_1 = \alpha(\sigma^*)^{n-1}\left[\sigma_1 - \frac{1}{2}(\sigma_2 + \sigma_3)\right]$$

$$\dot{\epsilon}_t = \alpha(\sigma_t - \sigma_r)^{n-1}\left[\sigma_t - \frac{1}{2}(\sigma_t + \sigma_r)\right]$$

$$\dot{\epsilon}_t = \alpha(\sigma_t - \sigma_r)^{n-1}\left[\frac{2\sigma_t - \sigma_t - \sigma_r}{2}\right]$$

$$\dot{\epsilon}_t = \frac{\alpha}{2}(\sigma_t - \sigma_r)^{n-1}(\sigma_t - \sigma_r)$$

$$\dot{\epsilon}_t = \frac{\alpha}{2}(\sigma_t - \sigma_r)^{n}$$

$$\dot{\epsilon}_t = \frac{\alpha}{2}\left[\bar{p}\left(\frac{3-2n}{2n}\right)\left(\frac{R_i}{r}\right)^{3/n} + \bar{p}\left(\frac{R_i}{r}\right)^{3/n}\right]^n. \tag{21}$$

In spherical coordinates, there is a specific relationship between tangential strain ϵ_t and the radial displacement vector u_r which represents the physical movement of material caused by the internal pressure $\bar{p}$. This equation can be arranged into a form directly relating tangential strain rate $\dot{\epsilon}_t$ to the time derivative of the radial displacement vector $\dot{u}_r$. By substituting this result into equation 21 and evaluating it at the surface of the cavity ($r = R_i$), one obtains an equation detailing the normalized growth rate of a cavity with radius R_i undergoing steady state creep controlled expansion as follows [6]:

$$\epsilon_{\varphi\varphi} = \frac{1}{r}\left(\frac{\partial u_\varphi}{\partial \varphi} + u_r\right)$$

$$\frac{\partial u_\varphi}{\partial \varphi} = 0, \quad \epsilon_{\varphi\varphi} = \epsilon_t$$

$$\epsilon_t = \frac{1}{r}(0 + u_r)$$

$$\epsilon_t = \frac{u_r}{r}$$

$$\dot{\epsilon}_t = \frac{\dot{u}_r}{r}$$

$$\dot{\epsilon}_t|_{r=R_i} = \frac{\alpha}{2}\left[\bar{p}\left(\frac{3-2n}{2n}\right)\left(\frac{R_i}{R_i}\right)^{3/n} + \bar{p}\left(\frac{R_i}{R_i}\right)^{3/n}\right]^n$$

$$\left.\frac{\dot{u}_r}{r}\right|_{r=R_i} = \frac{\alpha}{2}\left[\bar{p}\left(\frac{3-2n}{2n}\right) + \bar{p}\right]^n$$

$$\frac{\dot{R}_i}{R_i} = \frac{\alpha}{2}\left(\frac{3\bar{p}-2n\bar{p}+2n\bar{p}}{2n}\right)^n$$

$$\frac{\dot{R}_i}{R_i} = \frac{\alpha}{2}\left(\frac{3\bar{p}}{2n}\right)^n. \tag{22}$$

Indentation creep radial flow model

The question becomes how does one incorporate this creeping cavity behavior into an indentation model. Johnson's original differential volume equality needs to be reformulated for time dependent behavior by dividing each side by the time derivative dt. Setting $R_i = a$ like Johnson's original analysis and combining with equation 22 yields the solution for any circular cross-sectioned indenter undergoing steady state creep controlled by radial material flow, or

$$dV_{core} = dV_{indenter}$$

$$\frac{2\pi {R_i}^2 dR_i}{dt} = \frac{\pi a^2 dh}{dt}$$

$$\frac{\dot{R}_i}{R_i} = \left(\frac{1}{2}\right)\left(\frac{a}{R_i}\right)^2\left(\frac{\dot{h}}{R_i}\right)$$

$$\left(\frac{\alpha}{2}\right)\left(\frac{3\bar{p}}{2n}\right)^n = \left(\frac{1}{2}\right)(1)^2\left(\frac{\dot{h}}{a}\right)$$

$$\frac{\dot{h}}{a} = \alpha\left(\frac{3\bar{p}}{2n}\right)^n. \tag{23}$$

Equation 23 applies to any circular cross-sectioned indenter geometry from cylindrical flat punch to sphere. In the special cases of conical and spherical indenters, there is a geometric relationship between h and a. This allows equation 23 to be rewritten in terms of $\dot{h}/h$ using either $a = (Dh/2)^{1/2}$ where D is the diameter of the spherical indenter or $a = h\tan\theta$ where θ is the indenter centerline to face angle. This result suggests $\dot{h}/a$ as the more natural description of indentation creep, and yet analysis using the $\dot{h}/h$ metric is still perfectly valid for conical indentation. For spherical indentation equation 23 becomes

$$\frac{\dot{h}}{h} = 2\alpha\left(\frac{D}{a}\right)\left(\frac{3\bar{p}}{2n}\right)^n. \tag{24}$$

For conical indentation equation 23 becomes

$$\frac{\dot{h}}{h} = (\alpha\tan\theta)\left(\frac{3\bar{p}}{2n}\right)^n. \tag{25}$$

Bower's Analysis of Steady State Creep

A similar steady state indentation creep model has also been developed by Bower, et. al. To solve the problem, Bower started with the same generalized nonlinear creep law in equation 11 and used a transformation method proposed by Hill to convert the creep problem into a nonlinear elastic one. From this analysis, Bower found a similar characteristic strain rate for a creeping flat punch

controlled by the mean pressure under the indenter p_m and a dimensionless contact pressure parameter F of the form

$$\dot{\epsilon}_c = \frac{\dot{h}}{a} = \alpha \left(\frac{p_m}{F}\right)^n. \tag{26}$$

The advantage of Bower's approach is that it can incorporate free surface effects unlike the radial flow controlled model in equation 23. The downside is that F cannot be solved analytically for arbitrary n and indenter geometry. Because of this, to have the correct F value under arbitrary testing conditions would technically require an infinite number of finite element simulations. Because the indenter geometry dependence is fairly weak though, running simulations for a flat punch at a few representative stress exponents is sufficient to construct a polynomial fitted expression for an approximate F as a function of n that approximates most blunt indenters.

Unlike a flat punch with fixed contact area, the projected contact area for a cone or sphere can vary from that which would be expected purely from geometry owing to materials' individual tendencies to either pile-up or sink-in around the site of an indent. This geometric difference for a cone is illustrated in Fig. 16. Bower compensated for this by computing a sink-in/pile-up parameter c representing the ratio of the contact radius nominally expected from geometry to the true radius of contact. Just like F, c cannot be solved for analytically at arbitrary n, again requiring the computation of representative values fitted to a polynomial expression. Bower's tabulated values for F and c are listed in Tab. 1 and fitted to polynomials in Fig. 17. Using c, Bower's equation 26 can

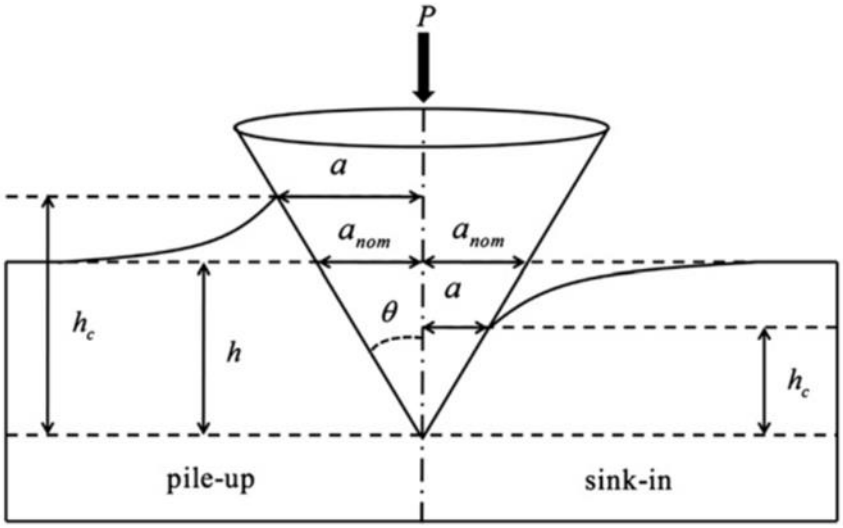

Figure 16. Geometry of a conical indent [8].

Table 1. Numerical results reported by Bower [7].

Tabulated Bower Coefficients			
1/n	**c, Cone**	**c, Sphere**	**F**
1	0.636	0.707	0.849
0.9	0.692	0.747	1.085
0.8	0.745	0.788	1.332
0.7	0.802	0.831	1.602
0.6	0.859	0.875	1.886
0.5	0.916	0.92	2.176
0.4	0.974	0.966	2.465
0.3	1.033	1.013	2.734
0.2	1.097	1.065	2.973
0.1	1.174	1.128	3.11
0.01	1.263	1.201	3.051

(a)

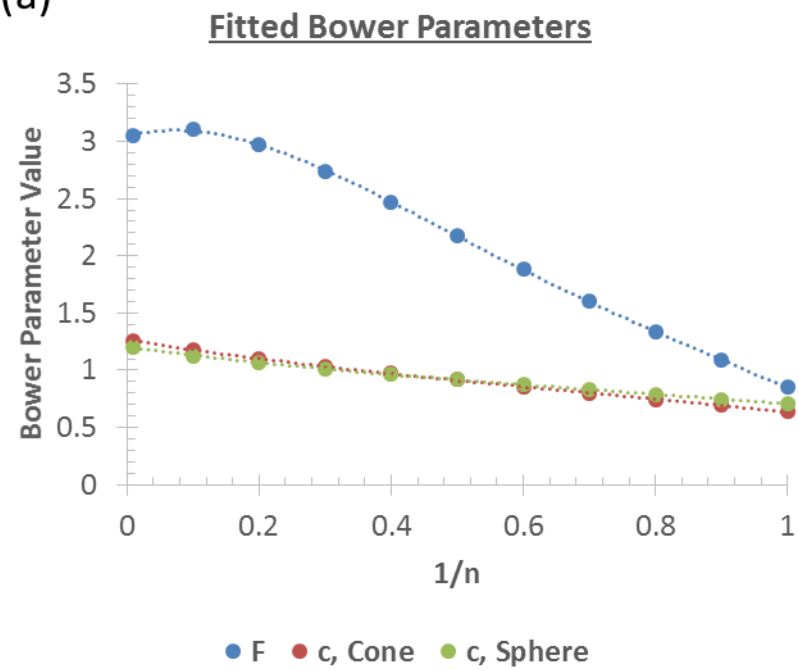

(b)

Bower Parameter Polynomial Fits
$F(n) = -4.4751\left(\frac{1}{n}\right)^4 + 12.191\left(\frac{1}{n}\right)^3 - 11.36\left(\frac{1}{n}\right)^2 + 1.4398\left(\frac{1}{n}\right) + 3.0477$
$c, Cone(n) = -0.2923\left(\frac{1}{n}\right)^3 + 0.5907\left(\frac{1}{n}\right)^2 - 0.9323\left(\frac{1}{n}\right) + 1.2671$
$c, Sphere(n) = -0.2309\left(\frac{1}{n}\right)^3 + 0.4971\left(\frac{1}{n}\right)^2 - 0.7663\left(\frac{1}{n}\right) + 1.2043$

Figure 17. Bower tabulated results from Tab. 1 (a) plotted as a function of inverse stress exponent (b) with polynomial fitted expressions.

be adjusted for conical indentation, which can be used to describe Berkovich indentation using its ~70° conical equivalent [7]. The relation is

$$\frac{\dot{h}}{h} = \alpha c \tan\theta \left(\frac{p_{nom}}{c^2 F}\right)^n. \tag{27}$$

Steady State Indentation Creep Theory Experimental Analysis

Flat punch experimental data treatment

For an initial test of the two models' validity, one can apply both theories to Chu and Li's original cylindrical flat punch succinonitrile crystal data. After extracting the raw indentation and uniaxial compression stress-strain rate data from Fig. 18 and 19, log-log plots of the uniaxial compression and indentation strain rates versus flow stress and hardness can be constructed. If the indentation and uniaxial characteristic strain rates are equated as one universal characteristic strain rate, both radial flow theory and Bower's model predict uniaxial flow stress by adjusting the measured indentation hardness. Practically speaking, this results in the raw indentation data being laterally shifted onto the uniaxial data. For initial estimation purposes, $\bar{p}$ in equation 23 can be treated as equal to the mean pressure under the indenter p_m.

This allows for a direct graphical comparison of uniaxially measured results with the predicted results from indentation testing. From Fig. 20, it is clear that both models approximately capture the measured uniaxial behavior. This suggests the starting steady state nonlinear creep law from equation 11 is a valid theoretical description of the impression creep regime. What's more, the

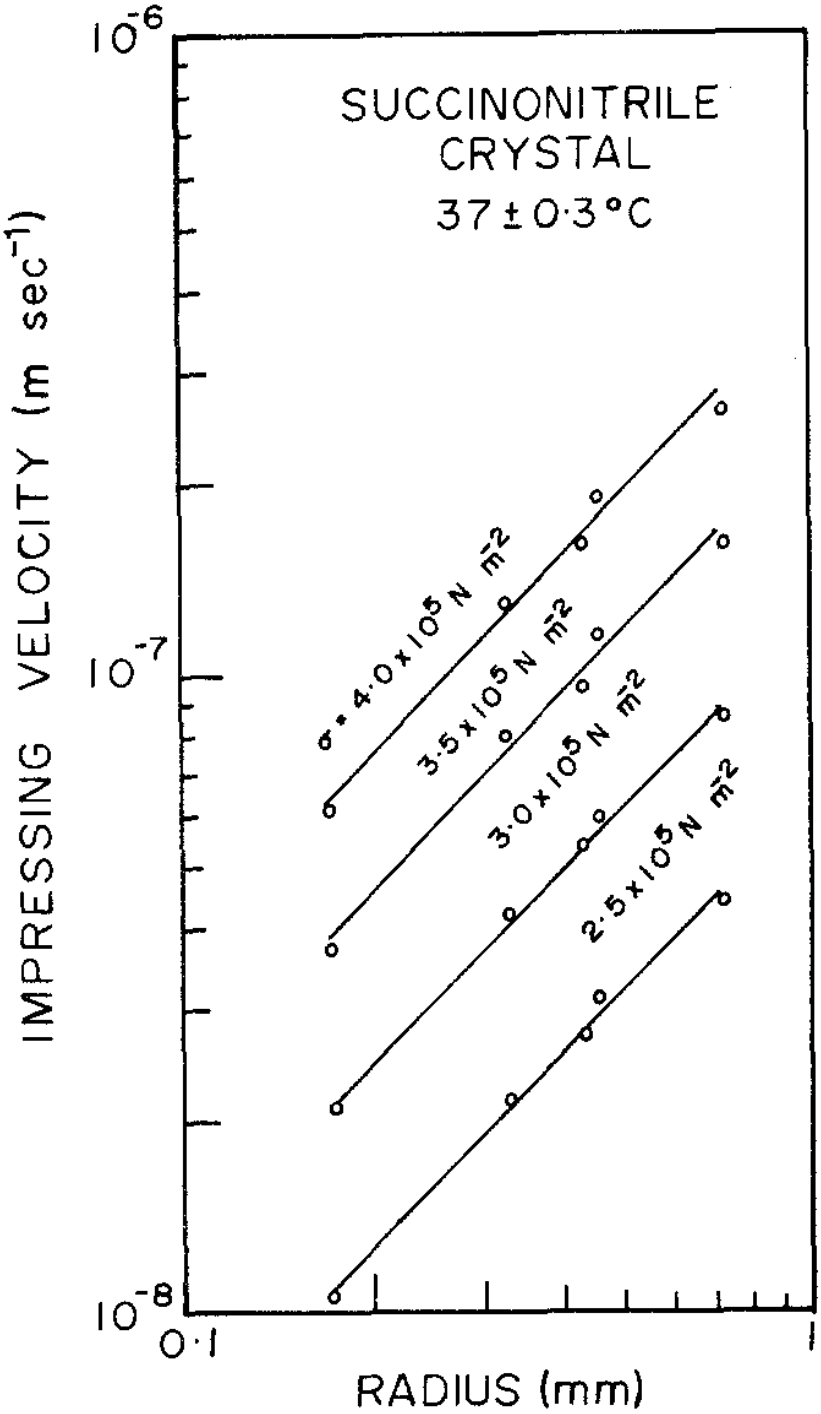

Figure 18. Chu and Li's succinonitrile indentation data [5].

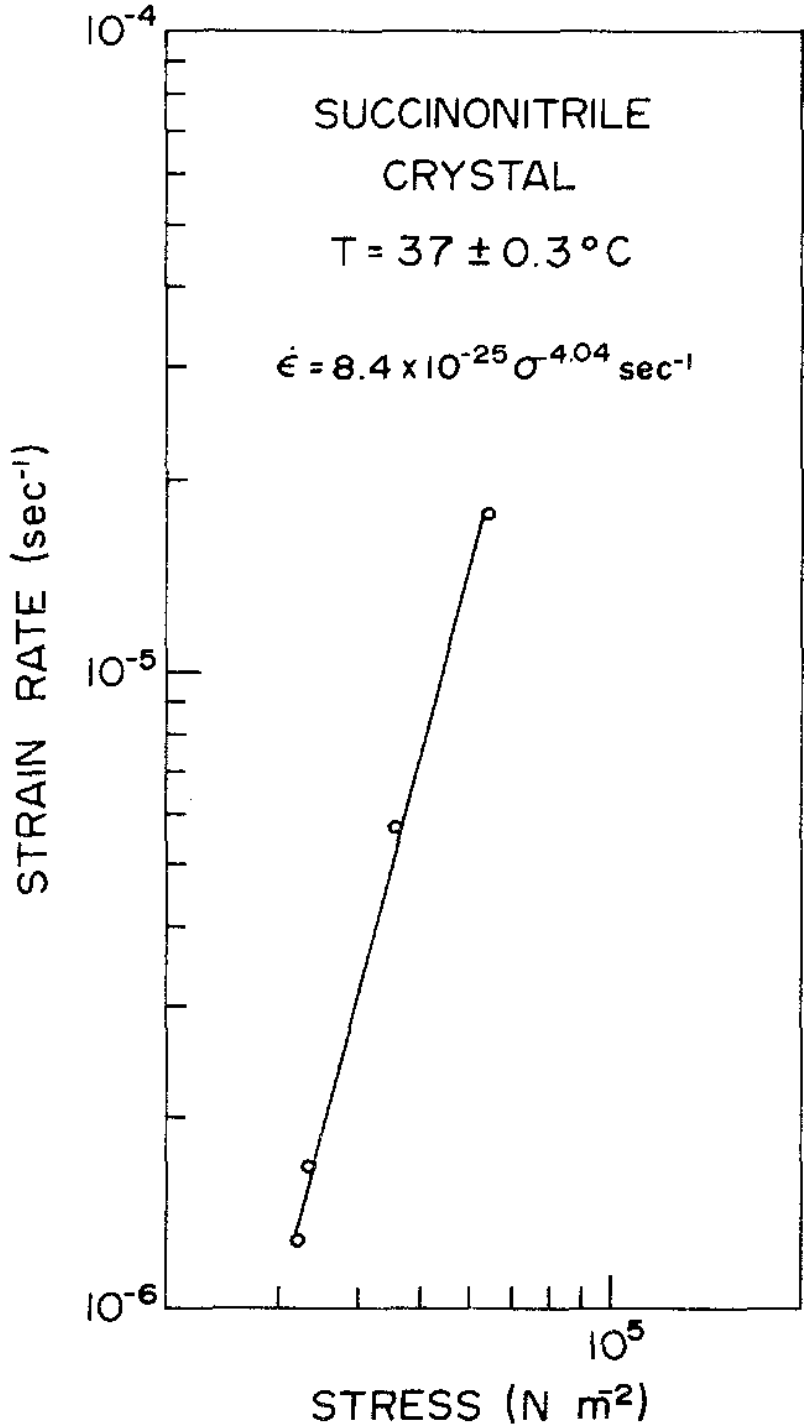

Figure 19. Chu and Li's succinonitrile uniaxial compression data [5].

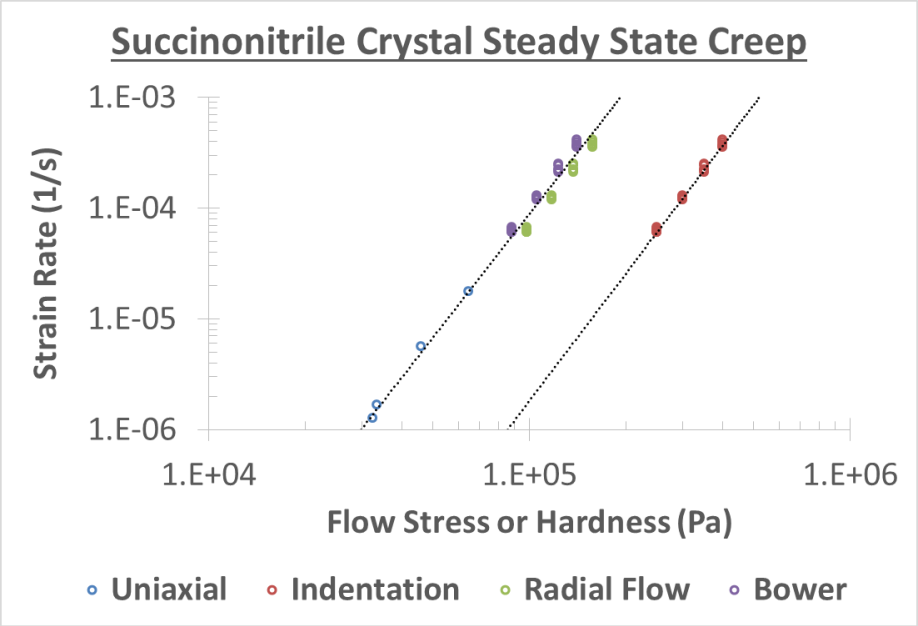

Figure 20. Plot of succinonitrile steady state creep results: uniaxial, indentation, and indentation predicted uniaxial.

agreement between the radial flow model and Bower's model suggest radial flow is dominate for $n = 4$.

Conical/Berkovich indenter experimental data treatment

The same approach used to compare the radial flow and Bower predictions for a flat punch can also be utilized to analyze conical equivalent indentation. For this, the Berkovich creep tests of Su, et. al. in amorphous selenium are analyzed by treating the Berkovich tip as its ~70° conical equivalent. From Su, amorphous selenium's uniaxial parameters were found from Fig. 21a to be $\alpha = 1.04 \times 10^{-12} Pa^{-1.15} s^{-1}$ and $n = 1.15$ while the most reliable corresponding indentation experiments from Fig. 21b showed $\beta = 1.53 \times 10^{-12} Pa^{-1.12} s^{-1}$ and $n = 1.12$. Running the indentation data through both the radial flow and Bower models shows, in Fig. 22, both models correctly predict the measured uniaxial behavior. The agreement is so close one can't even see the uniaxially measured and radial flow predicted data points beneath the Bower model predictions. This again suggests that the underlying nonlinear steady state creep law used to form both models remains valid for creeping materials when using a cone or Berkovich indenter. It also suggests radial flow continues to dominate creep for $n = 1$ [8].

Another Berkovich experimental dataset of interest is available for high purity indium. The uniaxial data for indium in Fig. 23 was originally collected back in 1960 by Weertman, long before nanoindentation was developed [9]. The indentation creep results in Fig. 24 would later be collected by Lucas and Oliver

(a) **Berkovich Indent Data**

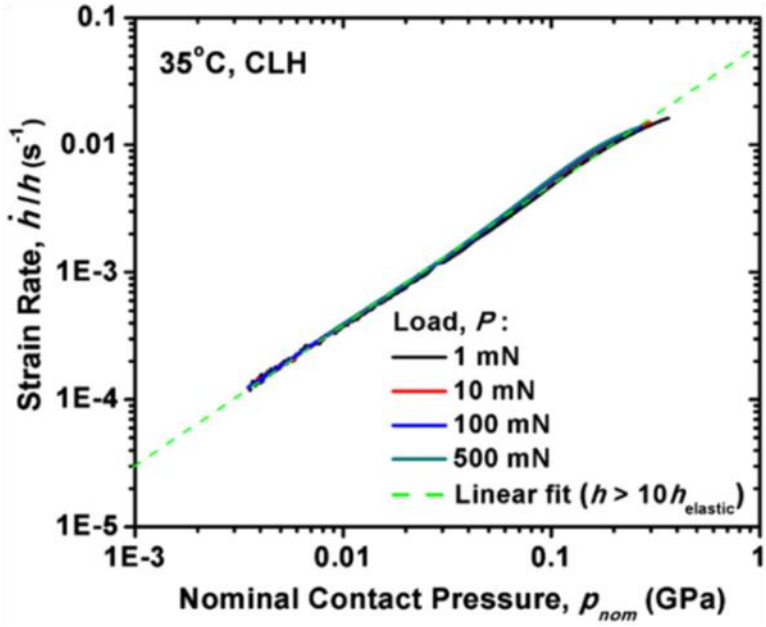

(b) **Uniaxial Compression Data**

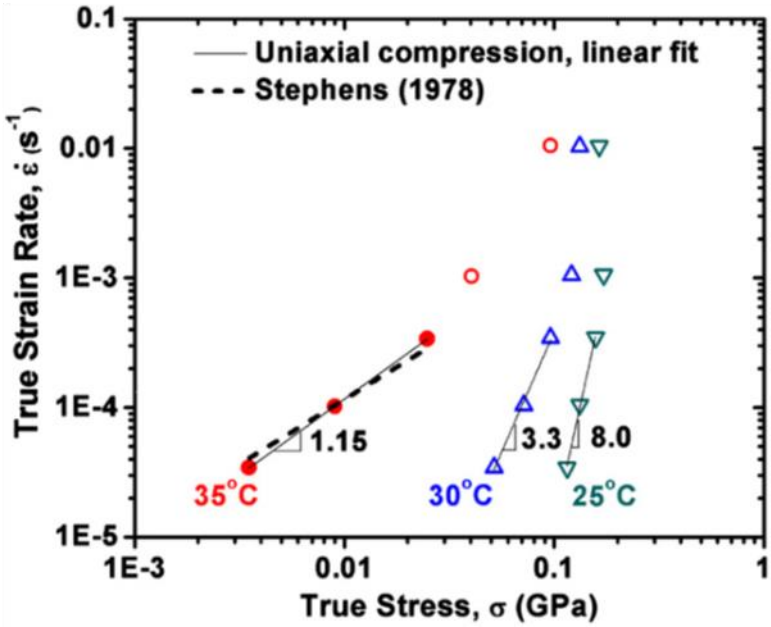

Figure 21. Su, et. al. amorphous selenium (a) Berkovich indentation data and (b) uniaxial compression data [8].

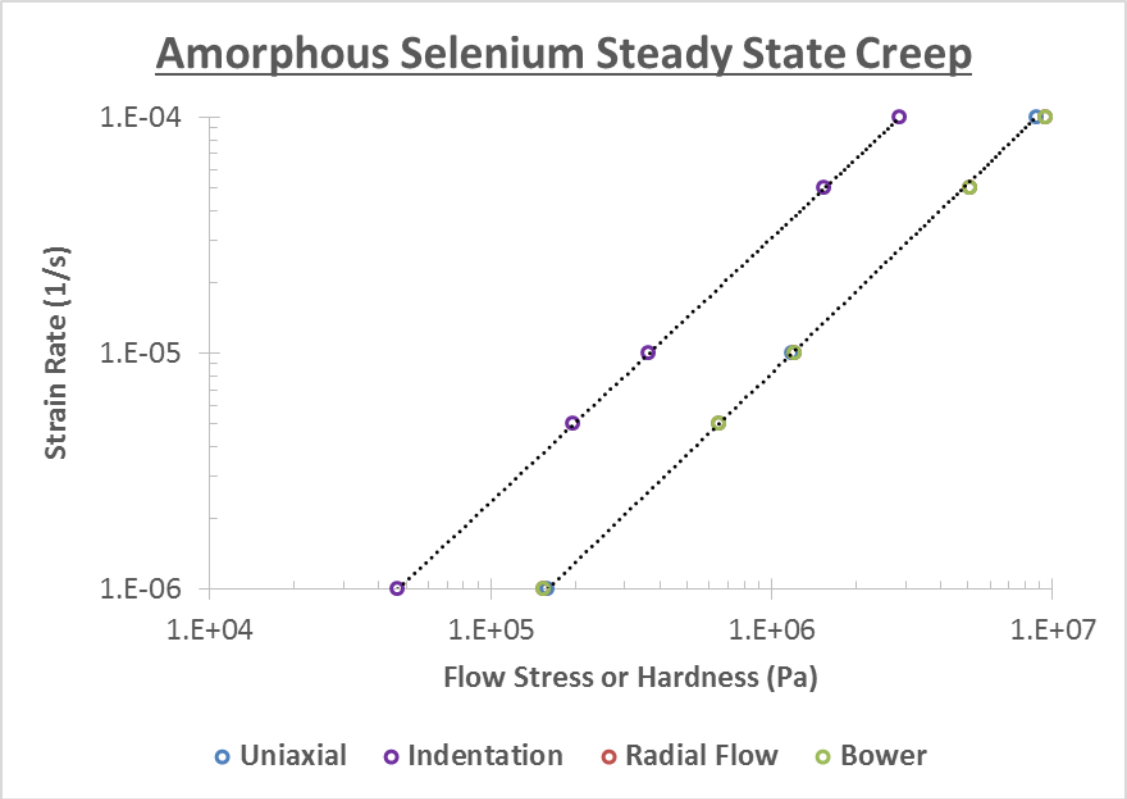

Figure 22. Amorphous selenium creep results: uniaxial, indentation, and indentation predicted uniaxial.

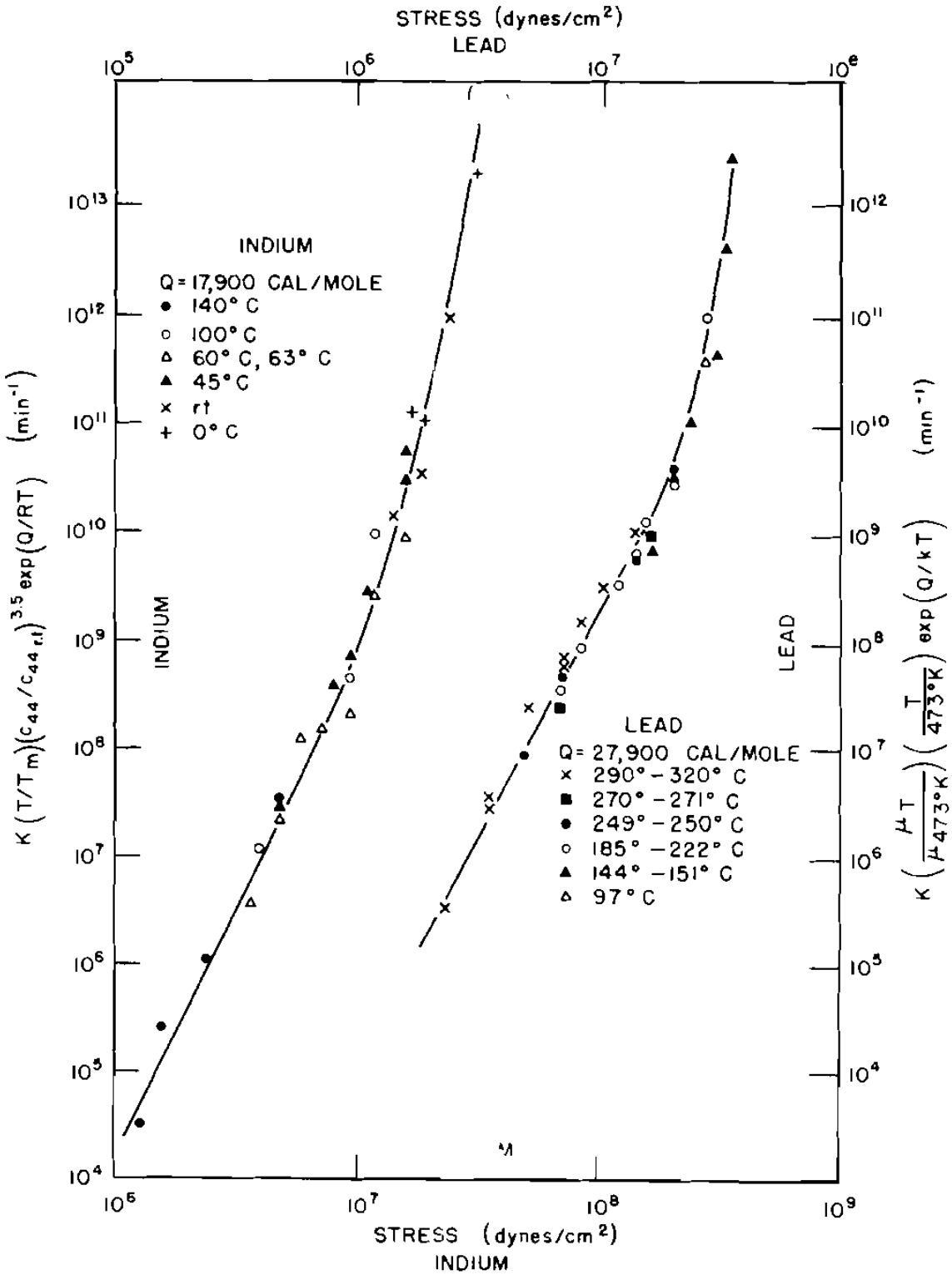

Figure 23. Uniaxial creep experimental results in pure indium from Weertman [9].

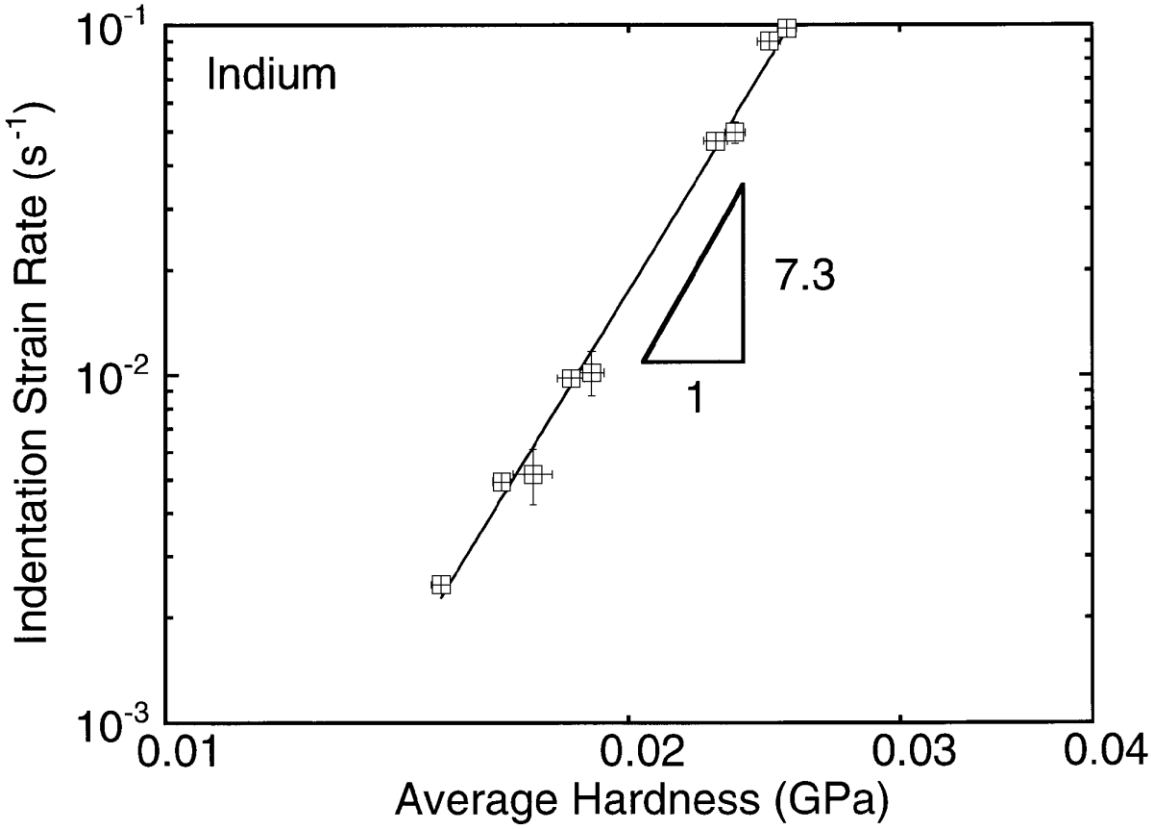

Figure 24. Indentation creep results in pure indium from Lucas and Oliver [10].

in 1992 [10]. If the same indentation to uniaxial analysis is performed as before on the indium experimental data, both indentation creep models get relatively close to predicting the uniaxial results in Fig. 25. Though the two models appear to have a higher degree of inaccuracy compared to the succinonitrile and amorphous selenium data, this variation has to be taken with a grain of salt as the indium experimental data sets were taken 40 years apart by two different research groups on two different source materials. The relative agreement does provide further evidence though that the underlying nonlinear steady state creep law works for cones/Berkovich indenters and that radial flow still mostly dominates even at $n \cong 7$.

The α/β parameter comparison

Given how well both the radial flow model and Bower's model work with each experimental dataset thus far, it is important to find under what conditions, if any, the two models begin to deviate. This can be accomplished for arbitrary n by setting each model's prediction expression for indentation creep equal to the basic indentation power law in equation 3. These equalities can be rearranged to show how each model predicts the α/β ratio between uniaxial and indentation pre-exponentials as a function of n. The relevant equations for a cone are

$$\dot{\epsilon}_i = \beta(p_{nom})^n = \alpha c \tan\theta \left(\frac{p_{nom}}{c^2 F}\right)^n$$

$$\left(\frac{\alpha}{\beta}\right)_{Bower,Cone} = (c^2 F)^n \left(\frac{1}{c \tan\theta}\right) \tag{32}$$

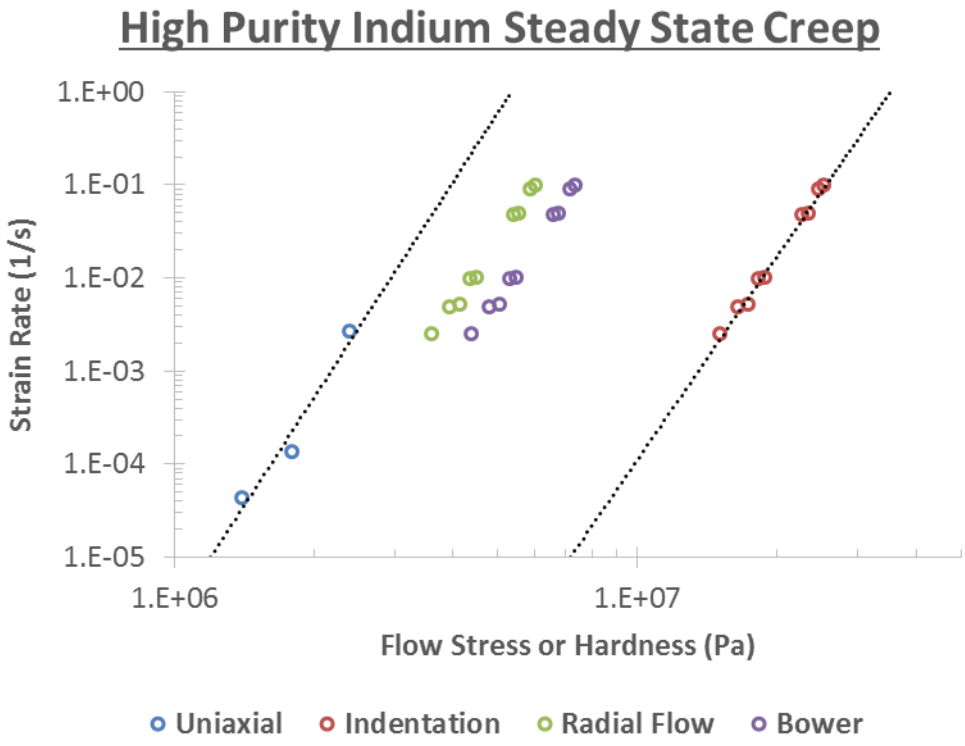

Figure 25. High purity indium creep results: uniaxial, indentation, and indentation predicted uniaxial.

$$\dot{\epsilon}_i = \beta(p_{nom})^n = \alpha \, tan\,\theta \left(\frac{3\bar{p}}{2n}\right)^n$$

$$\left(\frac{\alpha}{\beta}\right)_{radial\ flow\ model,Cone} = \left(\frac{2n}{3}\right)^n \left(\frac{1}{tan\,\theta}\right). \tag{33}$$

Taking the ratio of the two models' α/β parameters and looking for where the ratio is equal to or near unity shows where their respective predictions most closely agree. Figure 26's plot shows the two models agree to within factor of 3 for $n \cong 1 - 7$ for both a 70° cone and a cylindrical flat punch. This implies for these values of stress exponent radial flow dominates creep deformation, and beyond this region surface flow begins to have significant effects. Interestingly, there also appears to be a peak near $n \cong 3$ which corresponds roughly to where Bower's c parameter equals unity (i.e. no sink-in/pile-up). The exact reason for this is uncertain, but it may stem from the earlier assumption that the creeping cavity's $\bar{p}$ is equivalent to the mean pressure under the indenter p_m.

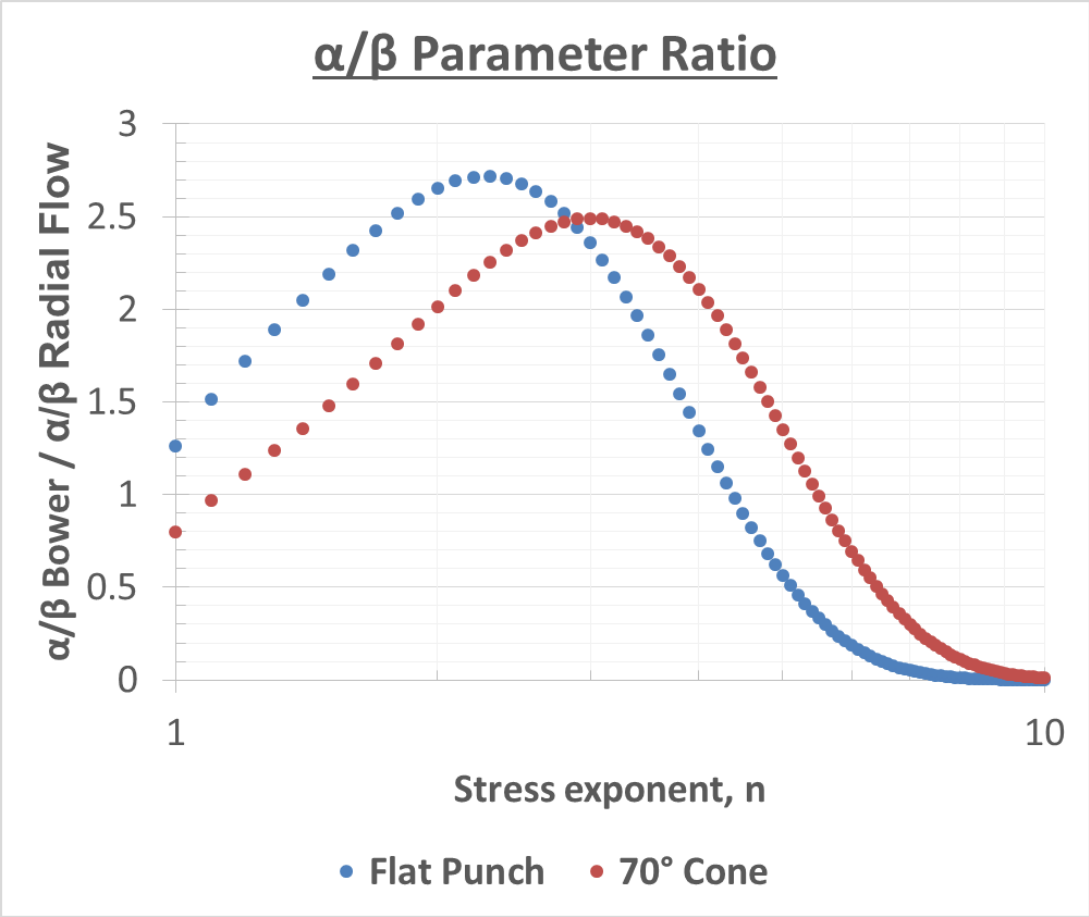

Figure 26. Plot of Bower versus radial flow model α/β parameter ratios for both a cylindrical flat punch and a 70° conical indenter.

References

[1] Harding, J. W. and I. N. Sneddon (1945). "THE ELASTIC STRESSES PRODUCED BY THE INDENTATION OF THE PLANE SURFACE OF A SEMI-INFINITE ELASTIC SOLID BY A RIGID PUNCH." Proceedings of the Cambridge Philosophical Society **41**(1): 16-26.

[2] Johnson, K. L. (1970). "CORRELATION OF INDENTATION EXPERIMENTS." Journal of the Mechanics and Physics of Solids **18**(2): 115-126.

[3] Prandtl, L. (1920). “Concerning the hardness of plastic bodies.” Nachrichten von der Gesellschaft der Wissenschaften zu Goettingen 74-80.

[4] Oliver, W. C. and G. M. Pharr (2004). "Measurement of hardness and elastic modulus by instrumented indentation: Advances in understanding and refinements to methodology." Journal of Materials Research **19**(1): 3-20.

[5] Chu, S. N. G. and J. C. M. Li (1977). "IMPRESSION CREEP - NEW CREEP TEST." Journal of Materials Science **12**(11): 2200-2208.

[6] Finnie, I. and W. R. Heller (1959). Creep of Engineering Materials. New York, McGraw-Hill.

[7] Bower, A. F., et al. (1993). "INDENTATION OF A POWER LAW CREEPING SOLID." Proceedings of the Royal Society-Mathematical and Physical Sciences **441**(1911): 97-124.

[8] Su, C. J., et al. (2013). "Measurement of power-law creep parameters by instrumented indentation methods." Journal of the Mechanics and Physics of Solids **61**(2): 517-536.

[9] Weertman, J. (1960). "CREEP OF INDIUM, LEAD, AND SOME OF THEIR ALLOYS WITH VARIOUS METALS." Transactions of the American Institute of Mining and Metallurgical Engineers **218**(2): 207-218.

[10] Lucas, B. N. and W. C. Oliver (1999). "Indentation power-law creep of high-purity indium." Metallurgical and Materials Transactions a-Physical Metallurgy and Materials Science **30**(3): 601-610.

Appendix

Consider the case of a purely elastically deforming cavity using the same core to indenter relating principles as Johnson's original model for conical indentation. First, Johnson's original differential volume equality is rearranged the same way needed to impose an elastic-perfectly plastic description. a represents the radius of the projected area of contact of the indenter, u_R is the radial movement of strained material, and θ is the indenter centerline to face angle. Just like in Johnson's original analysis, the radius of the hypothetical hemispherical core $R_i = a$ and developed into

$$dV_{core} = dV_{indenter}$$

$$2\pi R^2 du_R(R) = \pi a^2 dh = \pi a^2/\tan\theta\, da$$

$$\frac{du_R(a)}{da} = \frac{1}{2\tan\theta}.$$

Hooke's law in spherical coordinates can be simplified using $\sigma_1 = \sigma_2 = \sigma_t$ due to the modeled cavity's spherical symmetry requiring the two tangential strains be equal to each other. The remaining principal stress σ_3 becomes the radial stress σ_r. To match Johnson's elastic-plastic model approach, a Poisson's ratio of 0.5 is imposed further simplifying the expression for tangential strain into

$$\epsilon_1 = \frac{1}{E}[\sigma_t - \nu(\sigma_t + \sigma_r)]$$

$$\epsilon_t = \frac{1}{2E}(\sigma_t - \sigma_r).$$

From Lame, the stress equations for an elastic, thick walled spherical pressure vessel with uniform internal pressure $\bar{p}$ are known. R_i and R_o represent

the inner and outer surface respectively of the spherical vessel containing the cavity, and r represents the distance measured from the spherical cavity center yielding

$$\sigma_t = \frac{\bar{p}{R_i}^3}{{R_o}^3 - {R_i}^3}\left(1 + \frac{{R_o}^3}{2r^3}\right)$$

$$\sigma_r = \frac{\bar{p}{R_i}^3}{{R_o}^3 - {R_i}^3}\left(1 - \frac{{R_o}^3}{r^3}\right).$$

From infinitesimal strain theory, a specific relationship exists between tangential strain ϵ_t and the radial movement of material u_r. Because $\partial u_\varphi / \partial \varphi = 0$ from the cavity's spherical symmetry, one can evaluate for ϵ_t at the cavity's surface in terms of u_r and R_i yielding

$$\epsilon_t = \frac{1}{r}\left(\frac{\partial u_\varphi}{\partial \varphi} + u_r\right)$$

$$\epsilon_t|_{r=R_i} = \frac{u_r(R_i)}{R_i}.$$

Evaluating at $r = R_i$ when $R_o = \infty$, differentiating with respect to r, substituting into Johnson's differential volume relation, and rewriting in terms of $E/\tan\theta$ gives the final ECM description for the purely elastic regime. The final elastic ECM result is

$$\bar{p}_{Elastic\ ECM} = \frac{2}{3}\frac{E}{tan\ \theta}.$$

This matches exactly with the well-established elastic behavior predicted by Sneddon

$$p_{Sneddon} = \frac{2}{3}\frac{E}{tan\ \theta}.$$

CHAPTER II

THE MEASUREMENT AND ANALYSIS OF SUPERPROTONIC CHS MECHANICAL PROPERTIES

Abstract

The steady state creep behavior for CHS was measured using both uniaxial compression and nanoindentation. To interpret the nanoindentation results, the expanding cavity based radial flow model and Bower's model are used. The low flow stresses and fast creep rates measured suggest creep is a serious engineering issue when using solid acids in FC applications. The calculated power law creep parameters found disagree with previously reported values in the literature and suggest a dislocation based mechanism as driving creep deformation.

CHS Steady State Creep Experimentation

To date, there have been no reliable studies of the compressive creep behavior of solid acids. This oversight in the literature is rather important because of the compressive loading they can experience when used in fuel cell applications. Solid acid specimens are typically produced as thin, flat discs for fuel cell membrane assemblies rendering traditional uniaxial compression testing suboptimal for measuring bulk creep properties. Overcoming this limitation in existing specimens requires measuring these properties using a different testing method, namely nanoindentation. Alternatively, traditional uniaxial methods can be used by producing substantially larger specimens with correct aspect ratios for experiments. Testing in this study focused on CHS because it has historically

been the model material system in which scientific work in solid acids is first demonstrated.

Material production and sample fabrication

All CHS used was produced in batches using aqueous chemistry. For each batch, 210 g cesium carbonate, 99% (Alfa Aesar) was dissolved in 105 mL deionized water to which 133.4 g sulfuric acid, ACS, 95.0-98.0% (Alfa Aesar) was added dropwise while stirring. This mixture was then added to 1.2 L Methanol, ACS, absolute, low acetone, 99.8+% (Alfa Aesar) with the resulting CHS precipitate separated off via vacuum filtration. The filtered CHS powder was further rinsed with methanol then baked overnight at 60°C in Teflon lined container. The temperature was then raised to 110°C, and the mixture further baked for at least ~4-5 days. During the extended baking period, the CHS powder was ground daily using a mortar and pestle. The final fine powder was then uniaxially pressed under at least 125 MPa in ambient conditions into either 6 mm diameter x 2.8 mm thick disc specimens for nanoindentation or 0.75 inch diameter x 1.88 inch tall cylinders, shown in Fig. 27, for uniaxial compression. All specimens used for testing ranged from 96%-99% of theoretical density. All specimens were stored at 110°C under ambient atmosphere when not being processed or tested and baked for at least a continuous 24 hours before being tested. This extensive baking was necessary to ensure all CHS started in Phase II before converting to the superprotonic Phase I of interest.

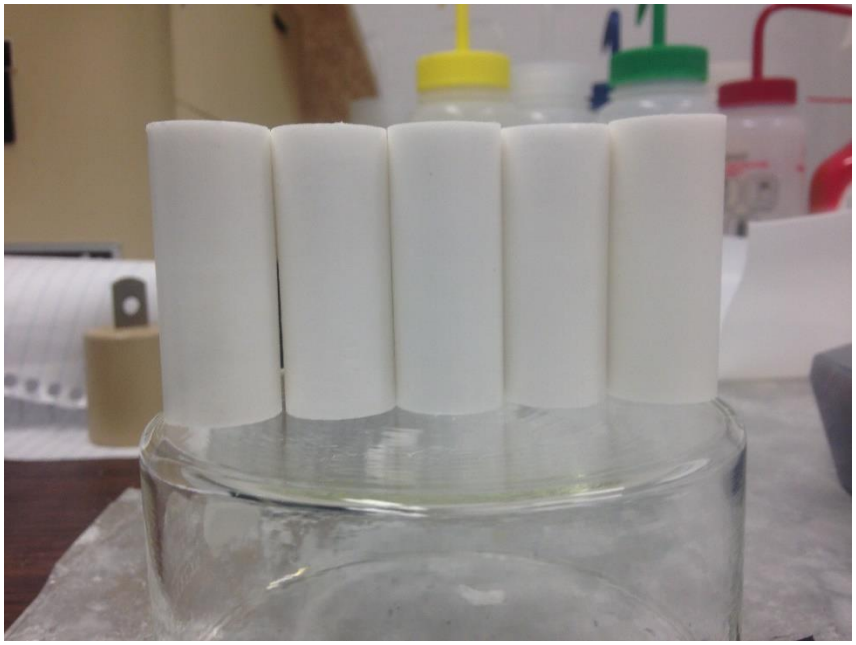

Figure 27. Uniaxial test specimen cylinders, aspect ratio 2.5.

For final testing preparations, all that was done for uniaxial testing was the application of DuPont Krytox GPL 205 grease between the test platens and sample to reduce frictional effects. Indentation specimens on the other hand required extensive surface polishing before testing. These specimens where hand ground sequentially on P1500, P2500, and P4000 SiC MicroCut grit paper (Buehler) and with a light fine grinding on 0.3 μm alumina FiberMet abrasive discs (Buehler). The ground specimens were then placed on a vibratory polisher and allowed to fine polish in a 0.05 μm MicroPolish alumina powder (Buehler) and high purity mineral oil slurry for at least 24 hours. The polished specimens were sonicated in toluene, anhydrous, 99.8% (Alfa Aesar) blasted with dry nitrogen, and then baked overnight at 110°C before testing the next day. The resulting surface is shown in representative Fig. 28.

One final concern for testing is that CHS begins to form a nonconductive dehydrant phase after being taken into the superprotonic phase I without sufficient environmental water partial pressure to thermodynamically suppress the decomposition. Unlike many other superprotonic solid acids though, this process is shown to be exceptionally slow for CHS in Fig. 29 which reveals minimal water loss, and therefore minimal decomposition to dehydrant phases, at the temperatures used in testing. For the longest testing period of ~5 hours at superprotonic temperatures, CHS decomposition is a nonissue [1].

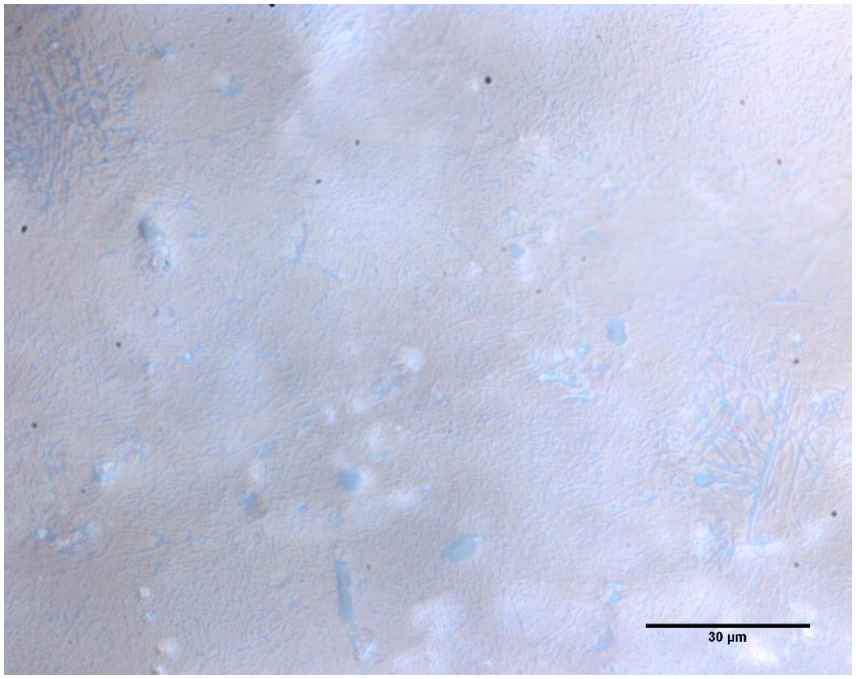

Figure 28. Example micrograph of polished CHS indentation specimen surface.

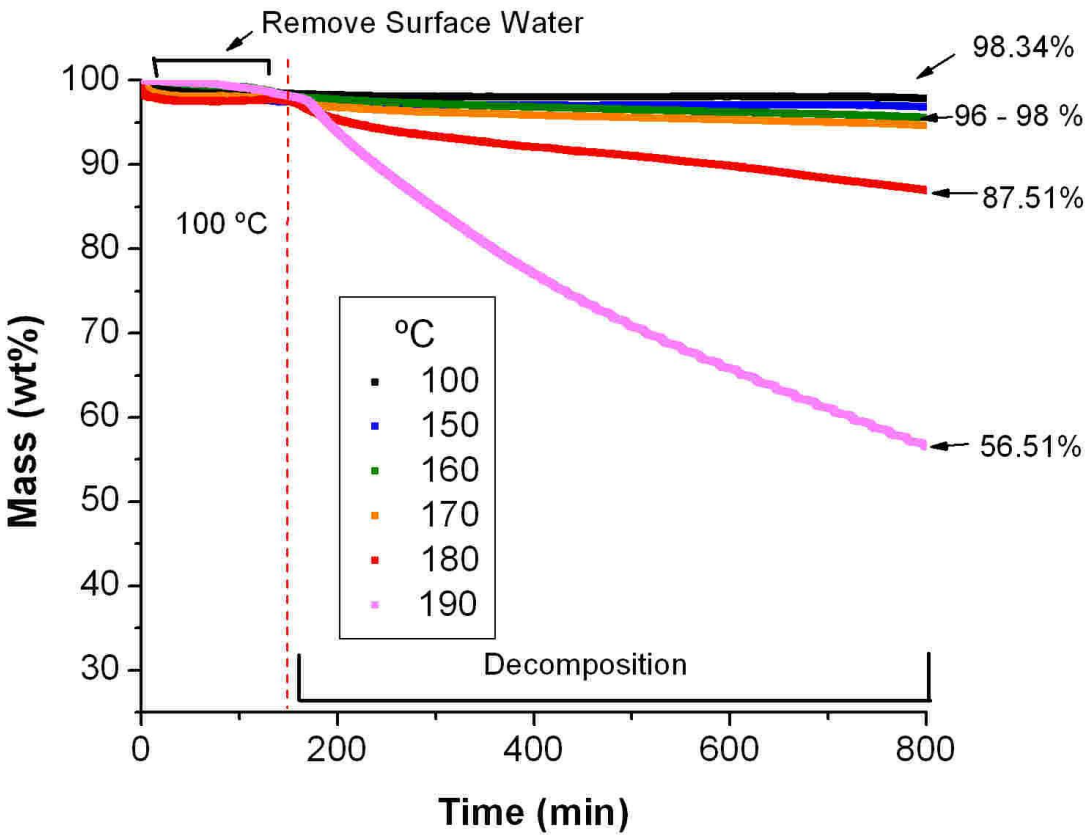

Figure 29. Thermogravimetric analysis of CHS in flowing argon corresponding to superprotonic phase decompositon [1].

Uniaxial compression experimental methodology

All uniaxial testing was done with the MTS 10/GL screw driven uniaxial tension and compression load frame in Fig. 30. Temperature was controlled by the environmental chamber affixed to the load frame. Creep tests were conducted using a constant displacement rate (CDR) method and variable displacement rate (VDR) method. For the CDR approach, the crosshead velocity was fixed, and the specimen deformed to a total engineering strain cutoff of 10%. For VDR, the crosshead velocity was held constant during set strain segments of the test but was periodically stepped up to capture more strain rate conditions with a given specimen. Under these testing methods, steady state is considered achieved when the flow stress needed to drive a given strain rate becomes constant. While creep is traditionally measured using constant stress tests, performing constant strain rate tests makes the uniaxial experiments more akin to the indentation testing which is done using a constant strain rate method due to physical device limitations.

Crosshead velocity was set to achieve a constant engineering strain rate with an attached 10,000 lbf rated load cell measuring applied load. Crosshead displacement and load were used to determine engineering stress and strain over the course of a test. Contributions from the load frame, etc. to deformation were ignored as the MPa/kPa scale flow stresses are very small compared to the steel test fixtures' multi GPa scale Young's moduli meaning other system strain contributions are negligible. Engineering stress and strain are converted to

Figure 30. MTS 10/GL screw driven uniaxial tension and compression load frame with attached environmental chamber.

true stress, strain, and strain rate through volume conservation and uniform deformation assumptions.

Nanoindentation experimental methodology

Nanoindentation tests were done on a custom built high temperature indenter under vacuum. Both specimen and indenter tip were independently heated to the temperature of interest. The area function of the diamond Berkovich tip used for testing was characterized by indenting fused silica producing the load-displacement curves in Fig. 31a. These curves are used to fit an area function yielding a constant modulus of 72 GPa in Fig. 31b. The constant stiffness squared over load value of ~700 N/m^2 in Fig. 31c indicates the nanoindenter's load and displacement outputs were correctly calibrated. The fused silica indents achieved depths of only about 2 μm, which is problematic however as 10 μm deep indents were needed for successful CHS creep testing. The silica area function's validity was verified out to the needed depths by also indenting polycarbonate producing load-displacement curves in Fig. 32a. No changes in modulus, Fig. 32b, or stiffness squared over load, Fig. 32c, with depth were exhibited in the polycarbonate indents indicating that the silica area function was still accurate to the desired depths. The silica fitted area function also matched with the manufacturer, MicroStar, measured area function in Fig. 33 providing further validation.

Testing was conducted using a constant strain rate (CSR) test method. Here, the indenter is driven into a material where loading rate $\dot{P}$ is controlled to

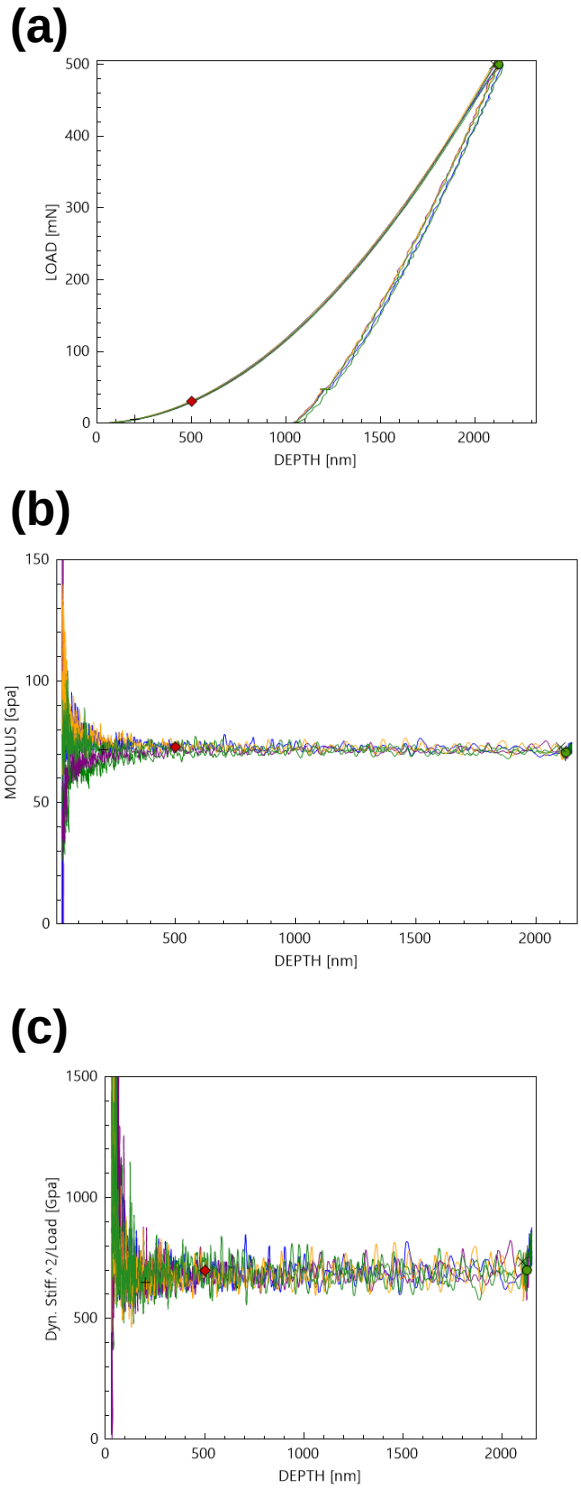

Figure 31. Fused silica (a) load-displacement curves, (b) Young's modulus using the calibrated area function, and (c) stiffness squared over load data.

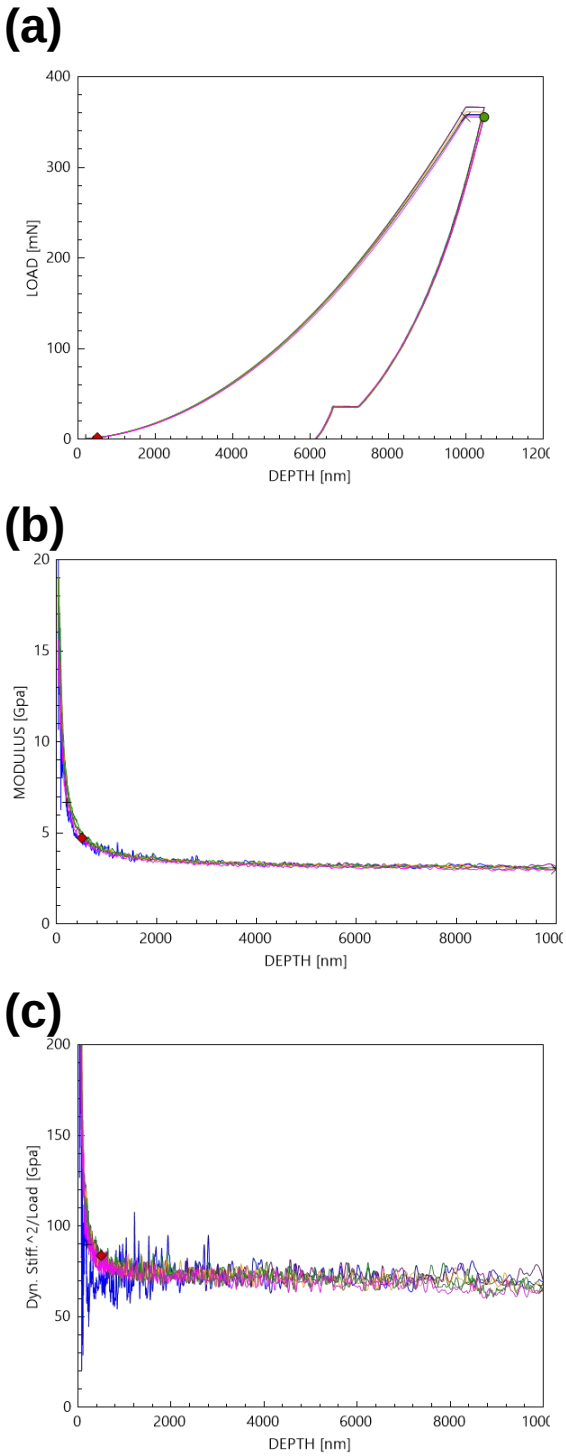

Figure 32. Polycarbonate (a) load-displacement curves, (b) Young's modulus data, and (c) stiffness squared over load data.

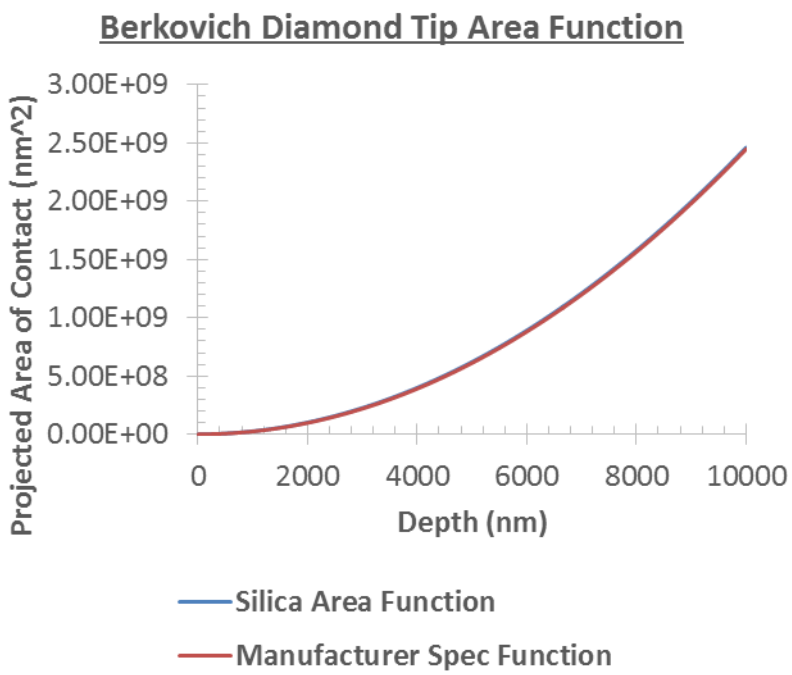

Figure 33. Measured area function versus manufacturer reported.

make $\dot{P}/P$ a constant. Doing this for a homogenous material with uniform hardness results in effectively imposing a constant strain rate $\dot{h}/h$ that is $0.5\,\dot{P}/P$ [2]. When steady state is achieved, the hardness (i.e. the indenter contact pressure) will become constant. The Oliver-Pharr CSM method was also run during testing to measure Young's modulus simultaneously [3].

Uniaxial Compression Testing, Results, and Analysis

Preliminary testing

Initially, several preliminary CDR tests were run to see if the results matched those of Kislitsyn. The sub-superprotonic 120°C specimens, while seeming to achieve some form of steady state deformation from their stress-strain curves in Fig. 34, exhibited large, non-uniform deformation in the form of double barreling as well as large crack formation in the samples' top and bottom surfaces. This combination of non-uniformity and fracture, shown in Fig. 35, means a power law steady state creep description was not appropriate for the sub-superprotonic data. The superprotonic CDR tests, however, did not exhibit these issues, and so further testing was solely focused on the superprotonic phase.

The first superprotonic tests were done at 160°C to directly compare with Kislitsyn's results. Figure 36 of the resulting stress-strain curves indicates steady state creep does exist and that a power law description can be applied. In Fig.

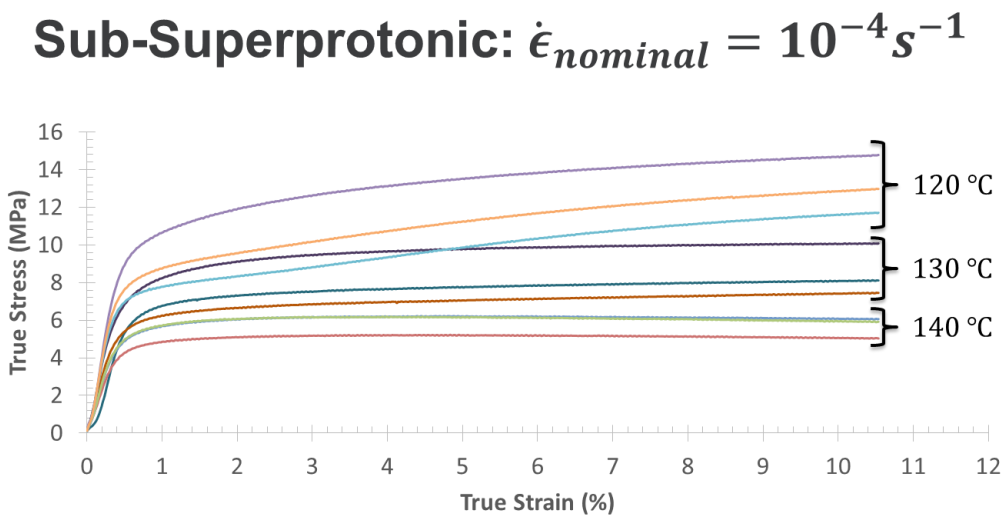

Figure 34. CHS sub-superprotonic phase II stress-strain curve uniaxial CDR method measured data.

(a)

(b)

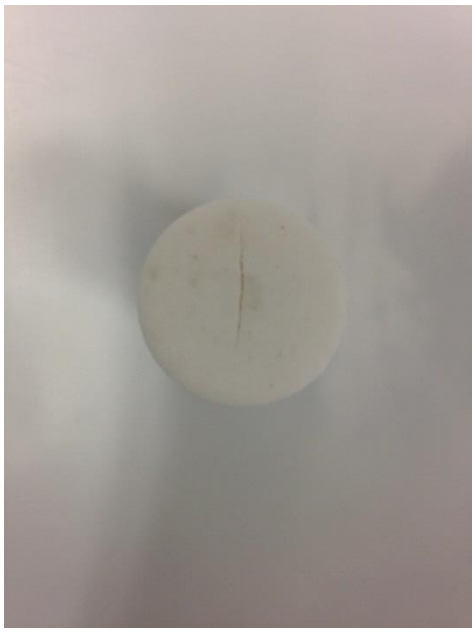

Figure 35. Examples in CHS below superprotonic transition of (a) double-barreling and (b) fracture.

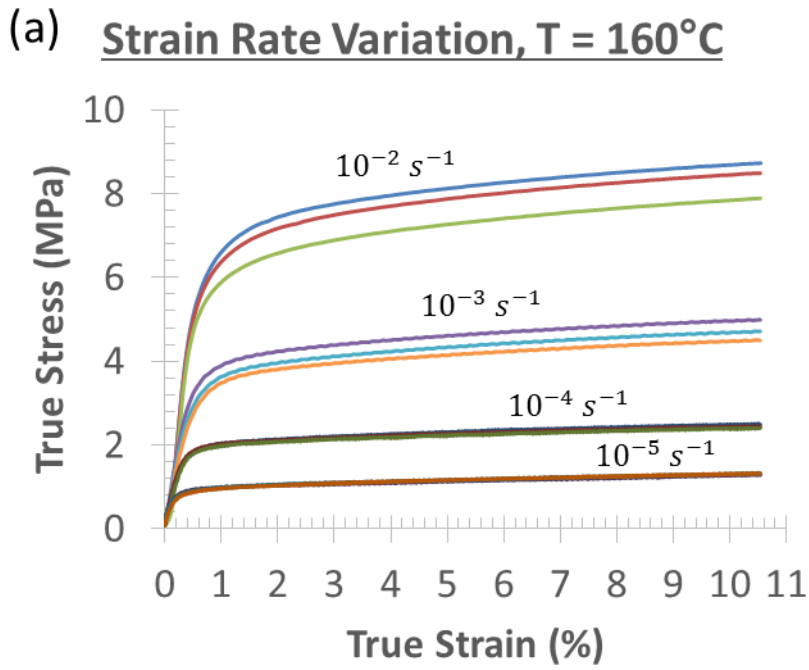

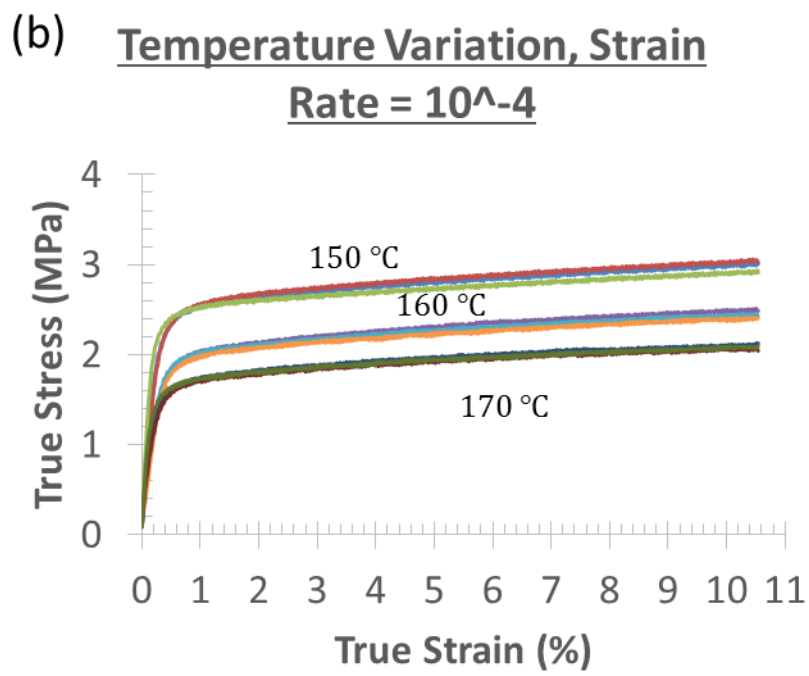

Figure 36. Initial CDR measured uniaxial stress-strain data in superprotonic CHS for (a) strain rate variation and (b) temperature variation.

37a the stress exponent was found to be $n = 3.63$. By taking additional $10^{-4}\ s^{-1}$ strain rate data at 150°C and 170°C and assuming $n = 3.6$, the relative creep activation energy of $Q = 1.03\ eV = 99.4\ kJ/mol$ was calculated in Fig. 37b. Fig. 37b also shows a clear shift in behavior before and after the superprotonic phase change. Because of the clear disagreement with the creep results of Kislitsyn, more testing was done to obtain a complete picture of CHS's creep deformation behavior.

Variable displacement rate (VDR) tests

To efficiently collect data for a wide range of creep conditions, the uniaxial test method was shifted to a VDR approach. Samples started being deformed at $10^{-5}\ s^{-1}$ and were then bumped up to 10^{-4}, 10^{-3}, and $10^{-2}\ s^{-1}$ over course of a test. Samples were deformed at 145°C, 150°C, and 160°C. Three tests were run at each testing condition. Figure 38 shows the resulting stress strain curves. Plotting up the final flow stress test results in Fig. 39 shows the VDR tests create the appearance of stress exponent varying with temperature, $n \cong 4.3 - 3.7$. Additionally, the activation energy $Q = 2.08\ eV = 200\ kJ/mol$ matches closely with that reported by Kislitsyn [1].

The disagreement with the initial CDR results left something of a conundrum as to which results should be believed. Ultimately, it was decided that the matching of the measured activation energy with Kistlitsyn's reported value and the higher than expected, changing stress exponents suggested some sort

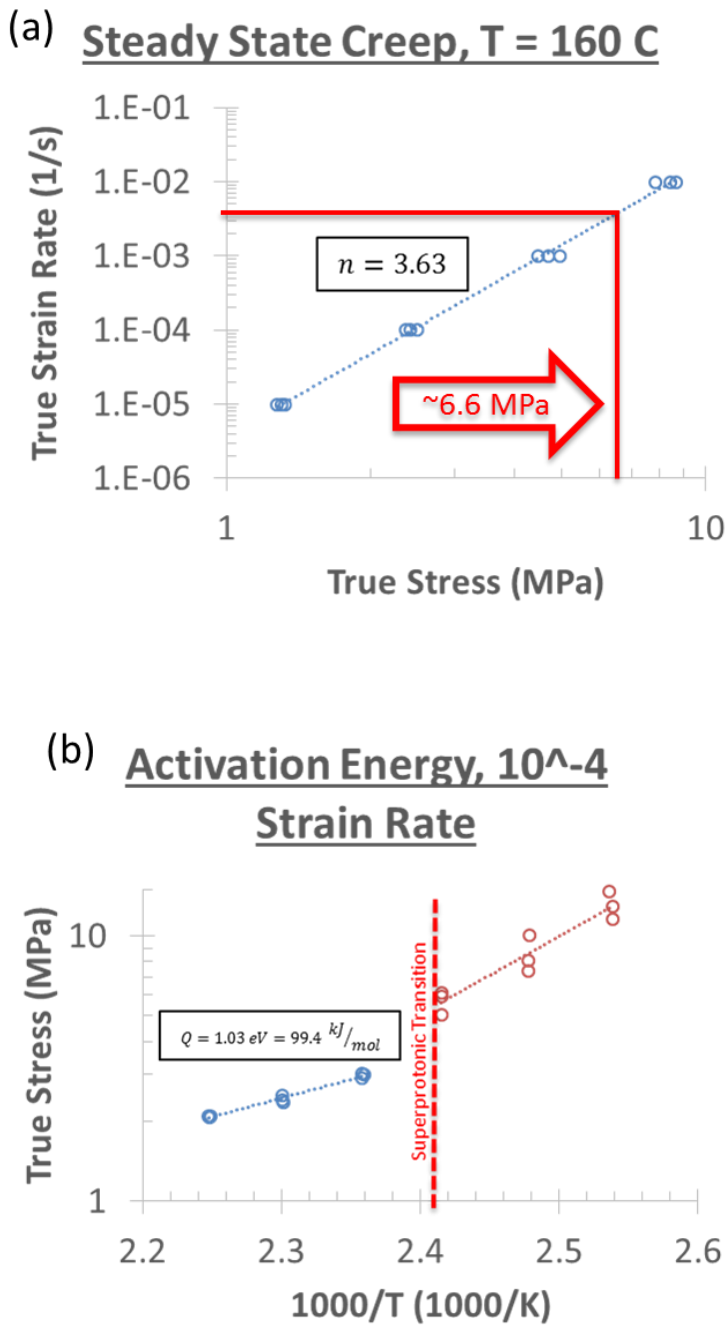

Figure 37. Initial CHS CDR creep results for (a) stress exponent with example FC compressive load and (b) activation energy with shift at superprotonic phase transition.

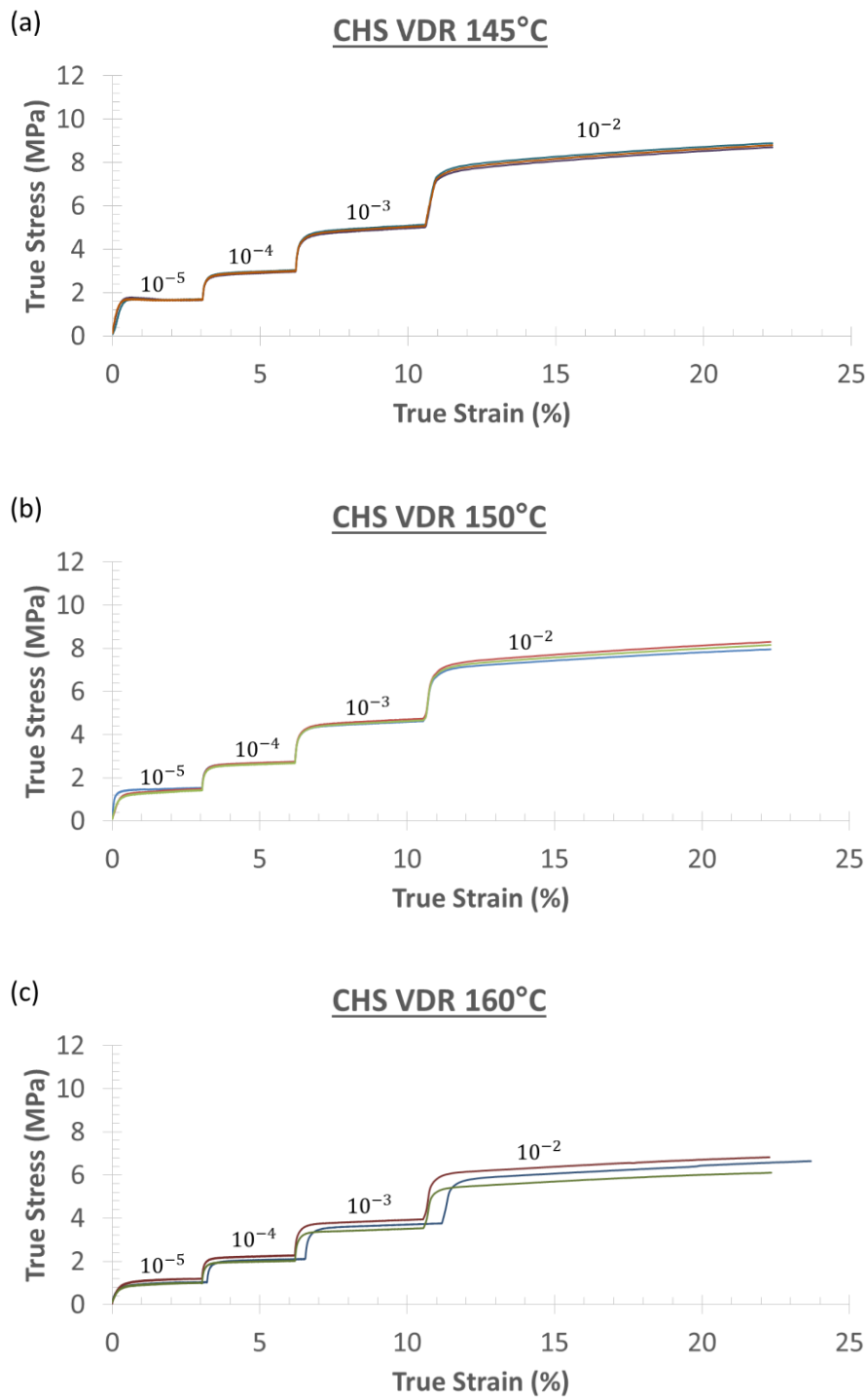

Figure 38. VDR measured uniaxial stress-strain curves with strain rates denoted in 1/s for (a) 145°C, (b) 150°C, and (c) 160°C.

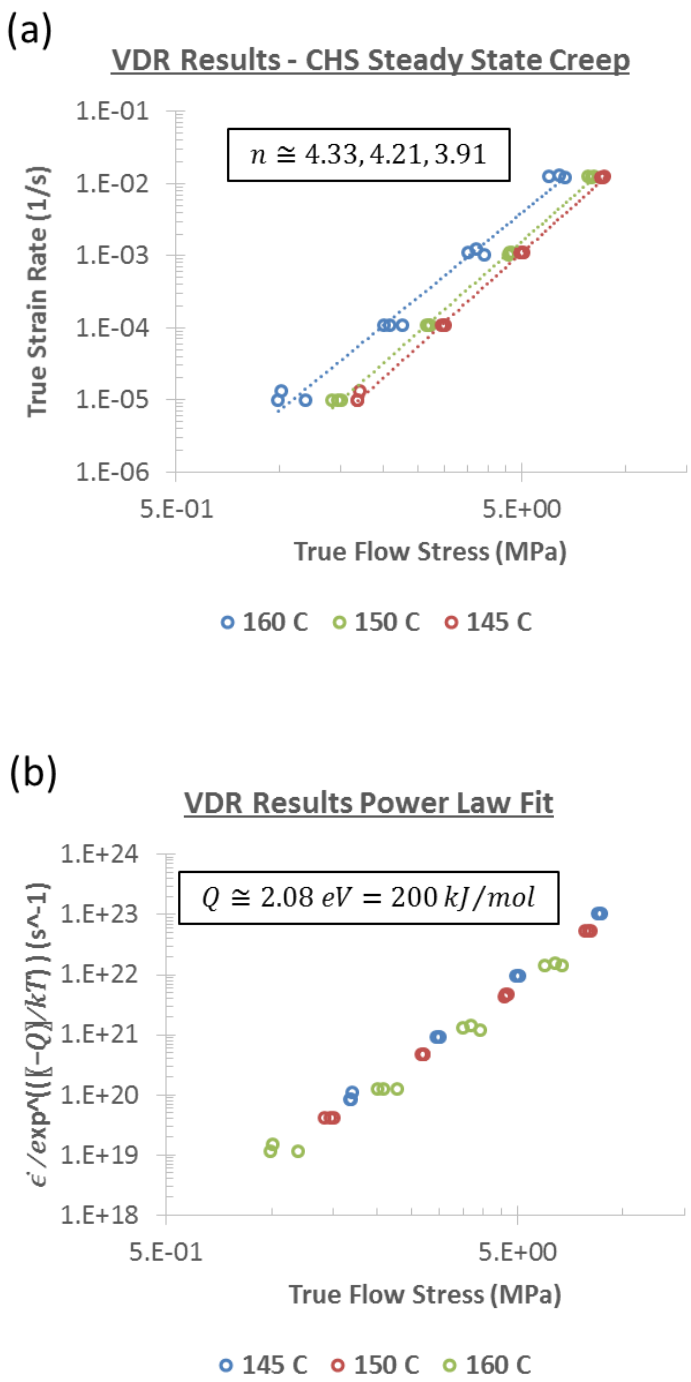

Figure 39. CHS uniaxial VDR method (a) measured creep results for stress exponent and (b) relative activation energy normalized creep results.

of non-steady state effect could be in play. In order to make a final determination, CDR testing for all the same conditions was required.

Constant displacement rate (CDR) tests

Further CDR testing was conducted at 145°C, 150°C, and 160°C at nominal strain rates of 10^{-5}, 10^{-4}, 10^{-3}, and $10^{-2}\ s^{-1}$. Three tests were run at each testing condition. The resulting stress-strain curves are presented in Fig. 40. The final CDR results in Fig. 41 reveal a stress exponent of $n \cong 3.6$ and activation energy $Q \cong 1.02\ eV = 99\ kJ/mol$. These results agree with and confirm the preliminary CDR uniaxial results from before. Because of the simpler nature of the CDR testing method, the fact that the CDR stress exponent is essentially stable, and that the VDR activation energy is closer to Kislitsyn's reported non-steady state results, the CDR data is to be preferred in describing CHS's steady state creep regime.

Focusing on the CDR results, the stress exponent of $n \cong 3.6$ would suggest a dislocation based mechanism controlling creep. Whether or not the activation energy of $Q \cong 1.02\ eV = 99\ kJ/mol$ supports this assessment is open to interpretation. While the author is unaware of any self-diffusion activation energies in the literature for superprotonic CHS, information does exist for deuterated CHS just below the transition at 120°C. Comparison of the CDR measured Q with this data in Fig. 42 shows that while Q is larger than the self-diffusion energies for hydrogen and cesium, it is still reasonably close enough to support the possibility of a diffusion assisted dislocation creep mechanism driving

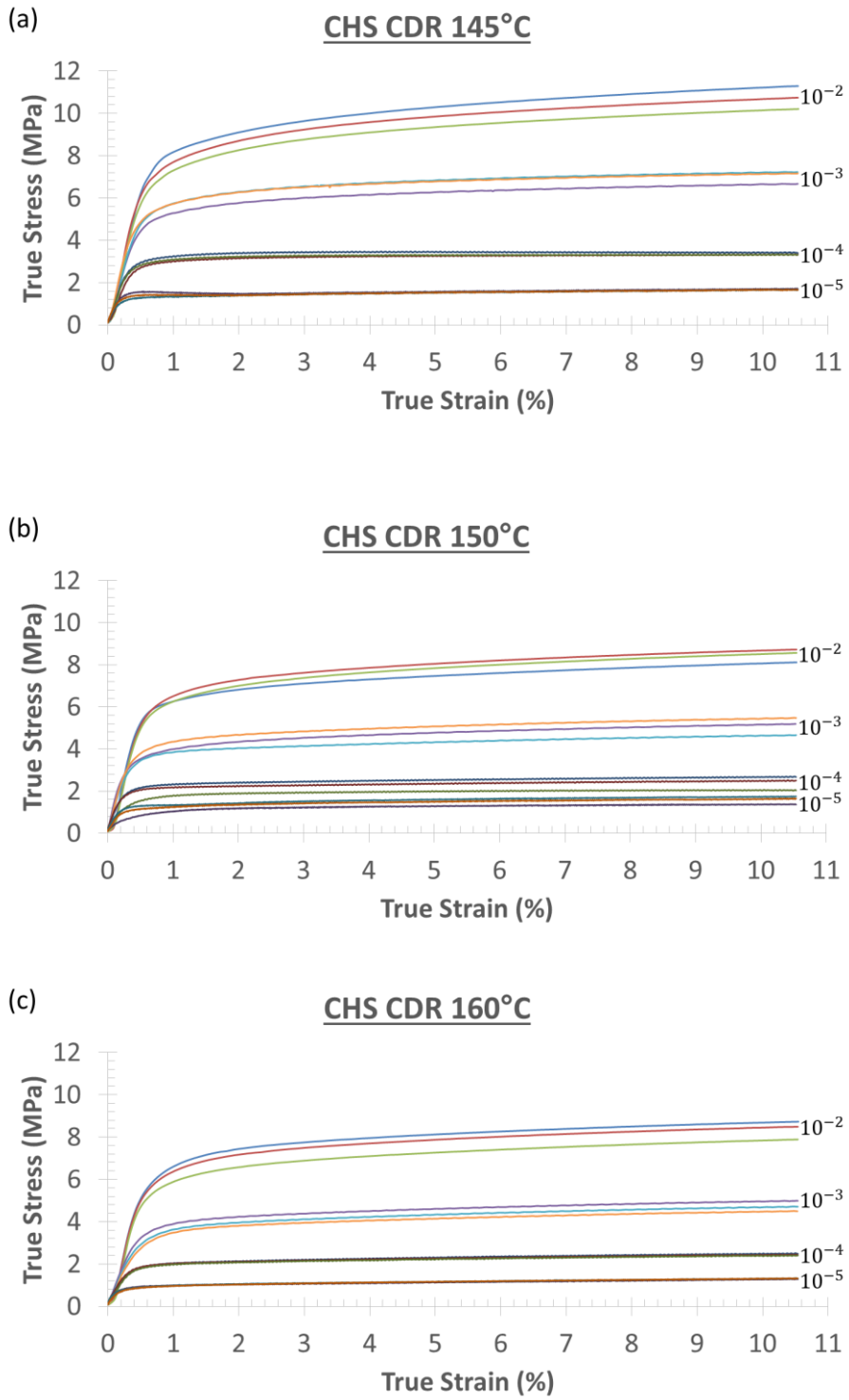

Figure 40. CDR measured uniaxial stress-strain curves with strain rates denoted in 1/s for (a) 145°C, (b) 150°C, and (c) 160°C.

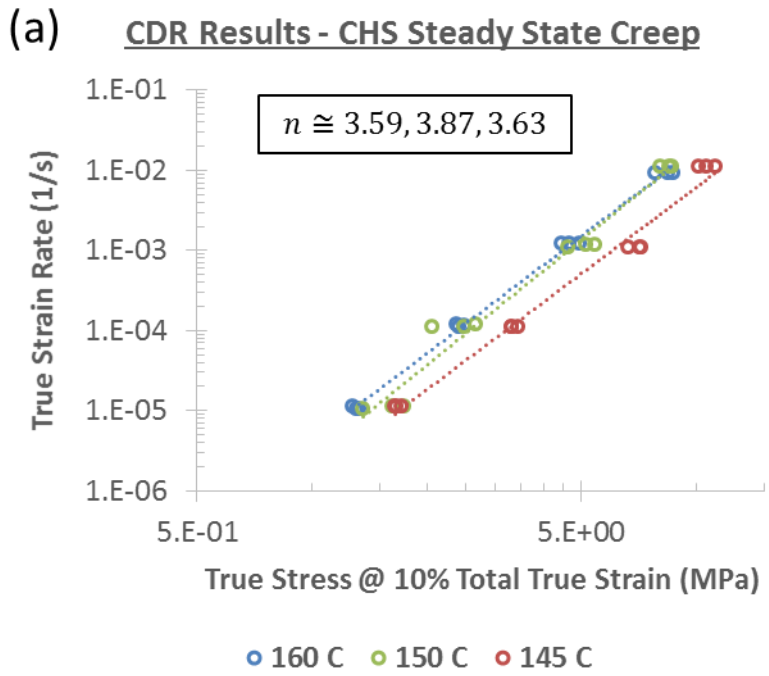

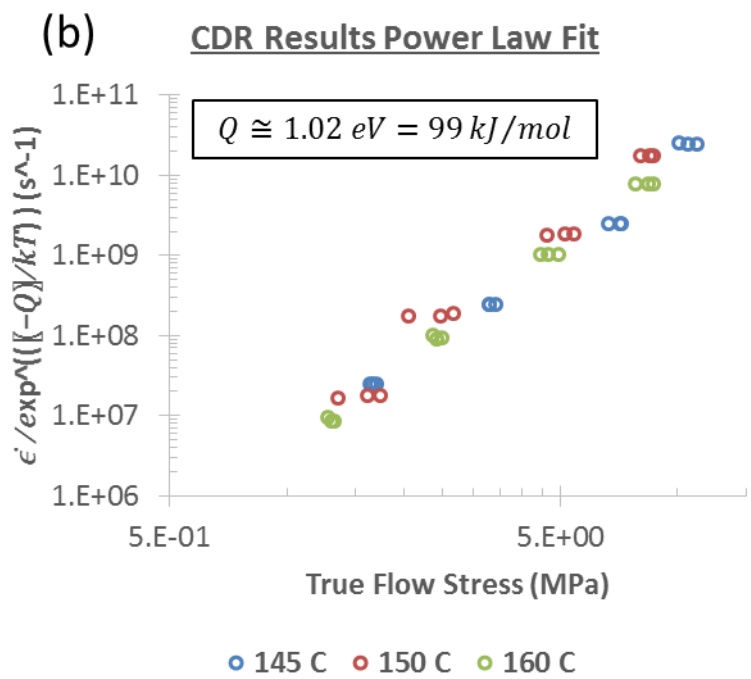

Figure 41. CHS uniaxial CDR method (a) measured creep results for stress exponent and (b) relative activation energy normalized creep results.

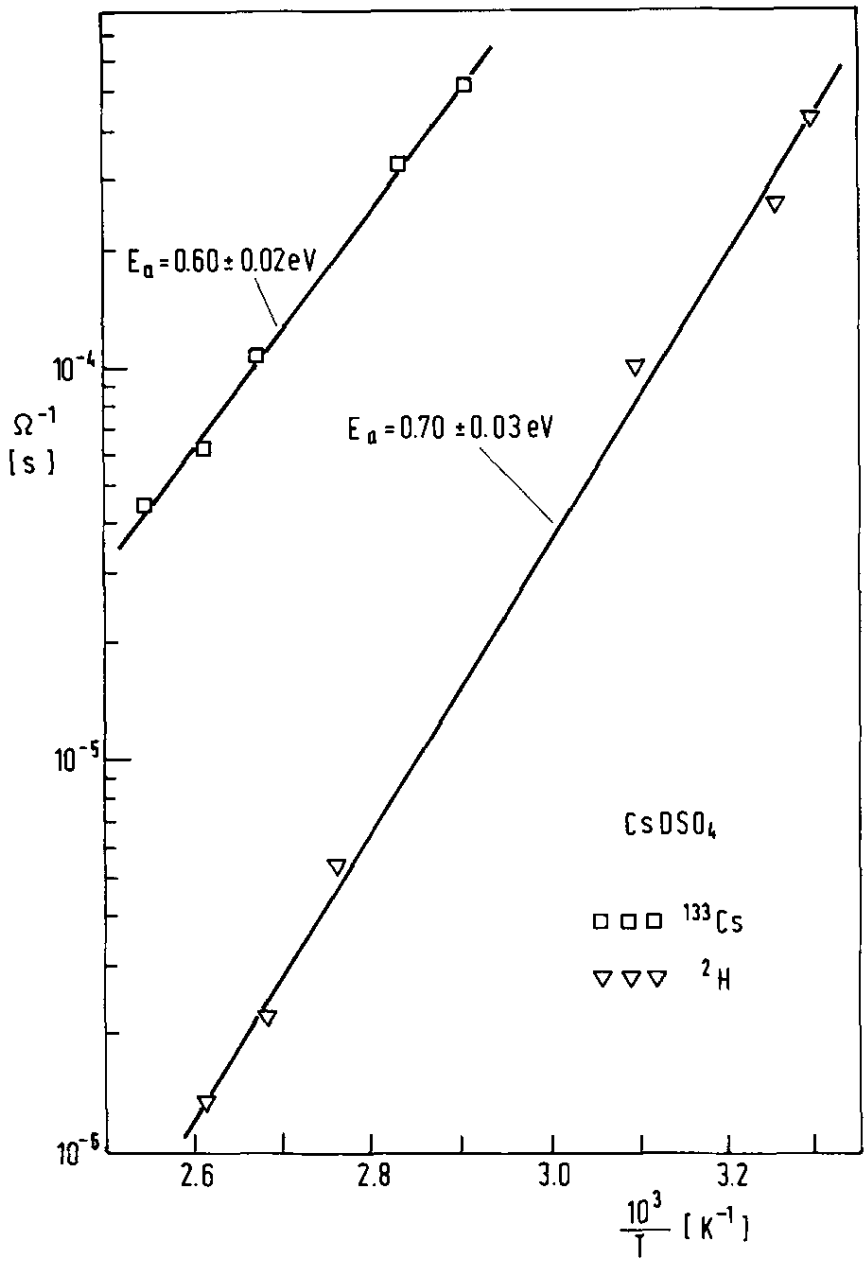

Figure 42. Phase II sub-superprotonic deutrated CHS NMR measured self-diffusion energies for hydrogen and cesium [4].

creep deformation [4]. Given the larger value of Q, it seems likely the rate limiting diffusing species is tied to the migration of the sulfate tetrahedron.

Nanoindentation Testing, Results, and Analysis

CSR indentation tests were conducted at 145°C, 150°C, and 160°C with constant $\dot{P}/P$'s of 0.200, 0.020, and 0.002 s^{-1}. The data for 145°C and $\dot{P}/P$ of 0.200 is presented in Fig. 43 as an example with the remaining experimental data presented in the Appendix. Figure 43a shows that the desired constant $\dot{P}/P$ is achieved for the majority of an indentation test. The reason for the non-constant $\dot{P}/P$ at the test start stems from the fact that at the test beginning P is zero leaving $\dot{P}/P$ undefined. To deal with this, at the test start a fixed loading rate is applied until P grows sufficiently large to achieve the desired $\dot{P}/P$ for the test at which point loading rate is adjusted on the fly to maintain $\dot{P}/P$. While loading the specimen, load-displacement data is recorded in Fig. 43b until a depth of 10 μm is reached. Focus is then placed on the deeper region of the tests, 5 to 10 μm, where $\dot{P}/P$ has been constant long enough for the system to have achieved or be near achieving steady state. The displacement data of Fig. 43b is then used to calculate $\dot{h}/h$ in Fig. 43c. These plots show a stable, constant indentation strain rate is indeed achieved during testing. The nominal hardness p_{nom} was calculated using the load data from the test divided by the fused silica determined area function in Fig. 43d. As p_{nom} also becomes essentially constant along side $\dot{h}/h$, steady state creep is achieved during testing.

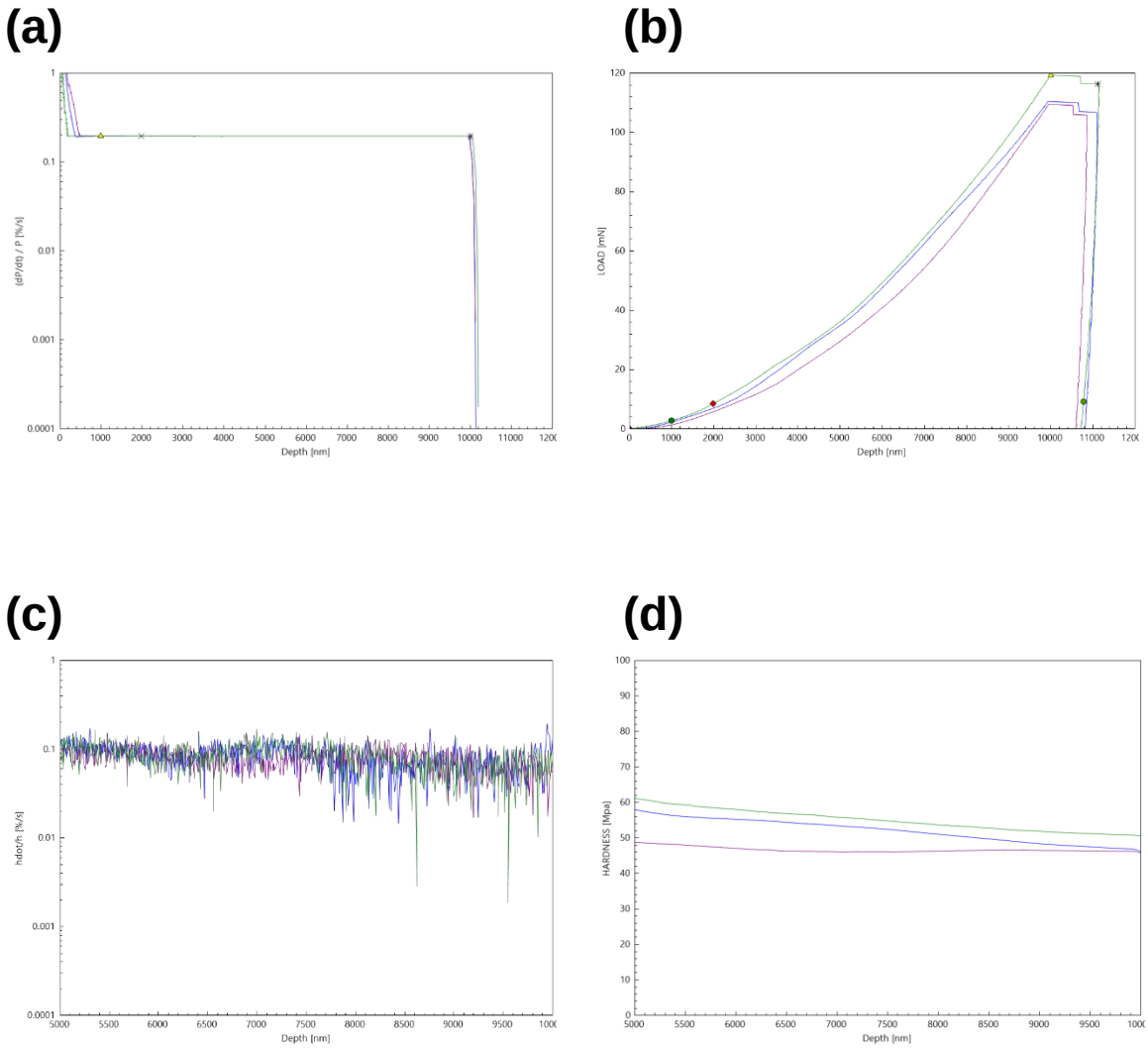

Figure 43. 145°C CSR indentation $(dP/dt)/P = 0.200\ s^{-1}$: (a) $(dP/dt)/P$, (b) load-displacement curves, (c) $(dh/dt)/h$, and (d) nominal hardness.

To construct the usual creep log-log plots for power law fitting, the values for $\dot{h}/h$ and p_{nom} were obtained by averaging across the last micron of each test. These plots of indentation strain rate versus hardness reveal in Fig. 44 that $n \cong 3.5$, very similar to the CDR uniaxial result. Indentation results also show a relative activation energy of $Q \cong 1.06\ eV = 103\ kJ/mol$ in Fig. 45a which compares favorably with its CDR uniaxial counterpart in Fig. 45b by applying the radial flow and Bower models.

All existing experimental data is presented in its totality in Fig. 46. From this it is easy to see that the CSR indentation results noticeably differ from the suspect data of the VDR method and that reported by Kislitsyn. The indentation testing results closely mirror the same steady state creep values of stress exponent and relative activation energy as the CDR uniaxial method. Through the use of both radial flow and Bower's models, the CDR uniaxial creep behavior is successfully approximated.

As mentioned earlier, elastic modulus was simultaneously measured at temperature as a function of depth during testing in Fig. 47. For comparison, modulus tests were also run at room temperature with a diamond Berkovich tip on an MTS Nanoindenter XP. Figure 48 shows that in the phase II monoclinic room temperature state CHS $E \cong 22\ GPa$. Figure 49 shows that after heating well past the phase I superprotonic transition modulus drops by over a factor of five to $E \cong 4\ GPa$. This suggests time independent elastic deformation may also need to be taken into account when designing a solid acid FC device.

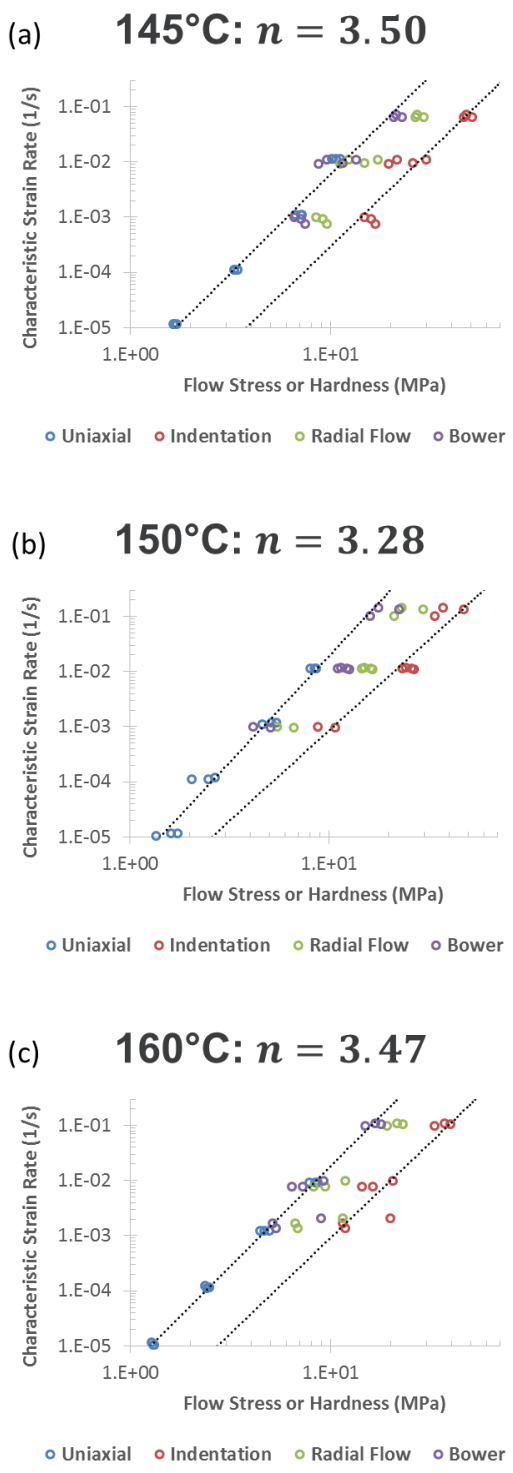

Figure 44. Indentation versus CDR uniaxial superprotonic creep stress exponent results at (a) 145°C, (b) 150°C, and (c) 160°C.

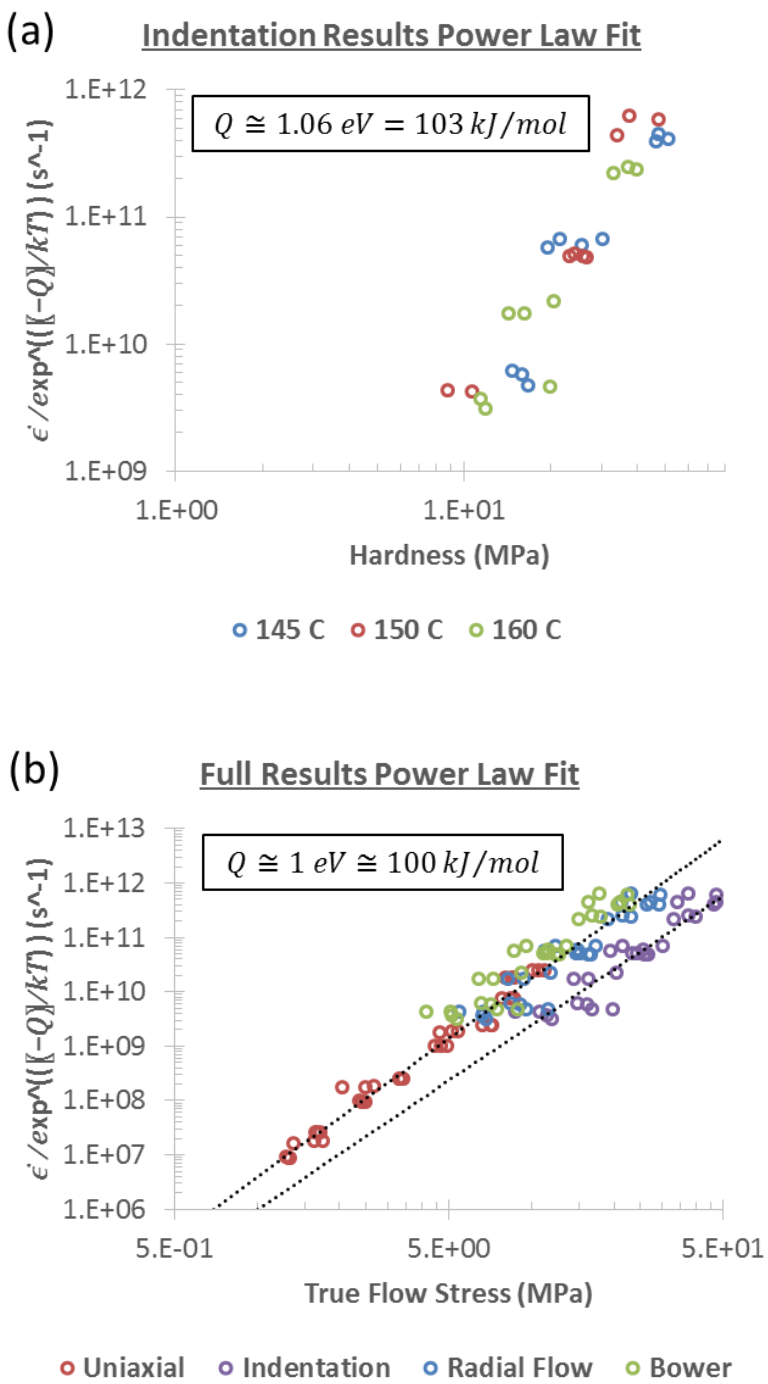

Figure 45. Superprotonic CHS indentation (a) measured relative activation energy normalized results (b) compared with CDR uniaxial data using both radial flow and Bower models.

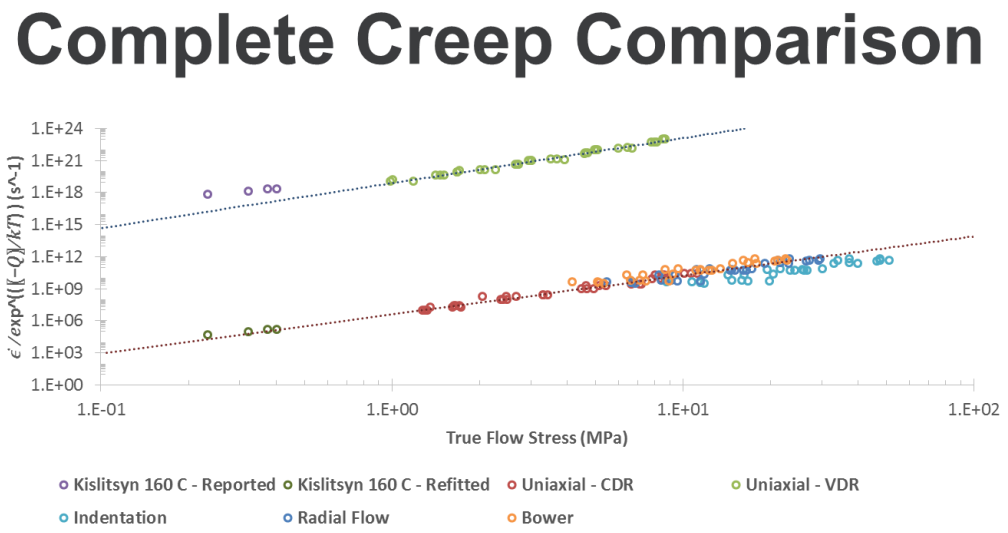

Figure 46. Superprotonic CHS creep relative activation energy normalized results compilation.

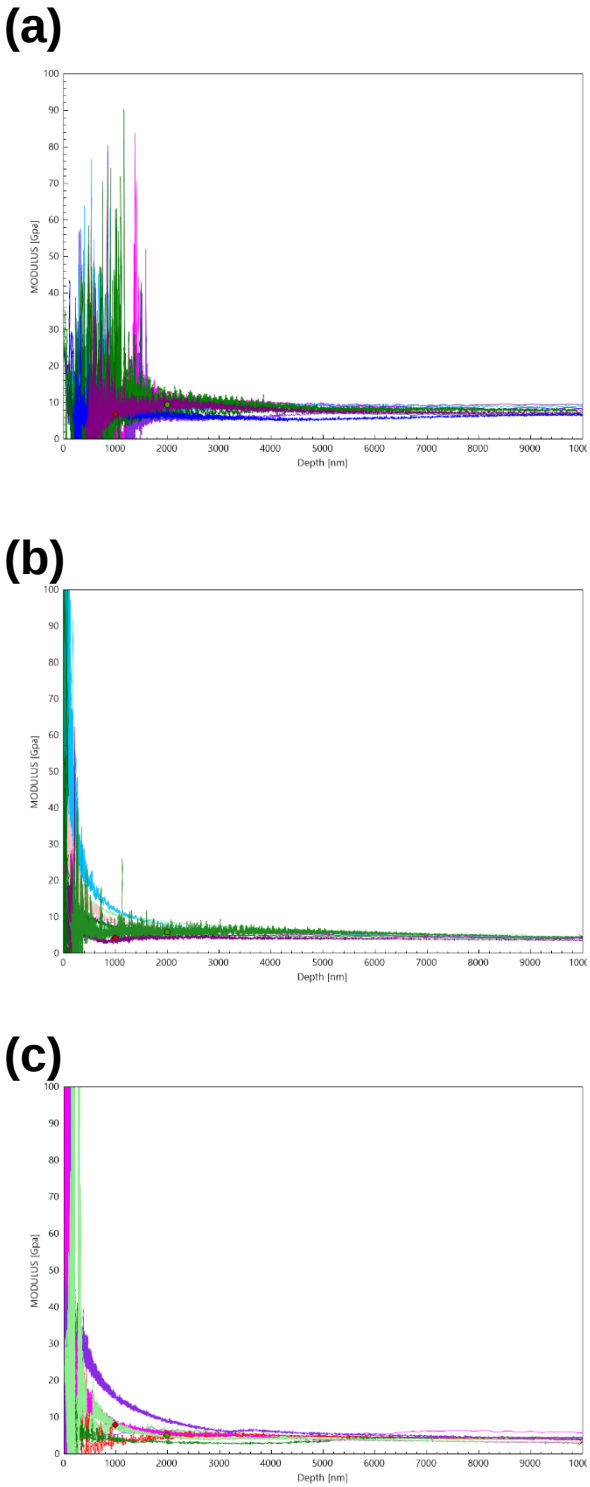

Figure 47. Superprotonic CHS indentation measured Young's modulus for (a) 145°C, (b) 150°C, and (c) 160°C.

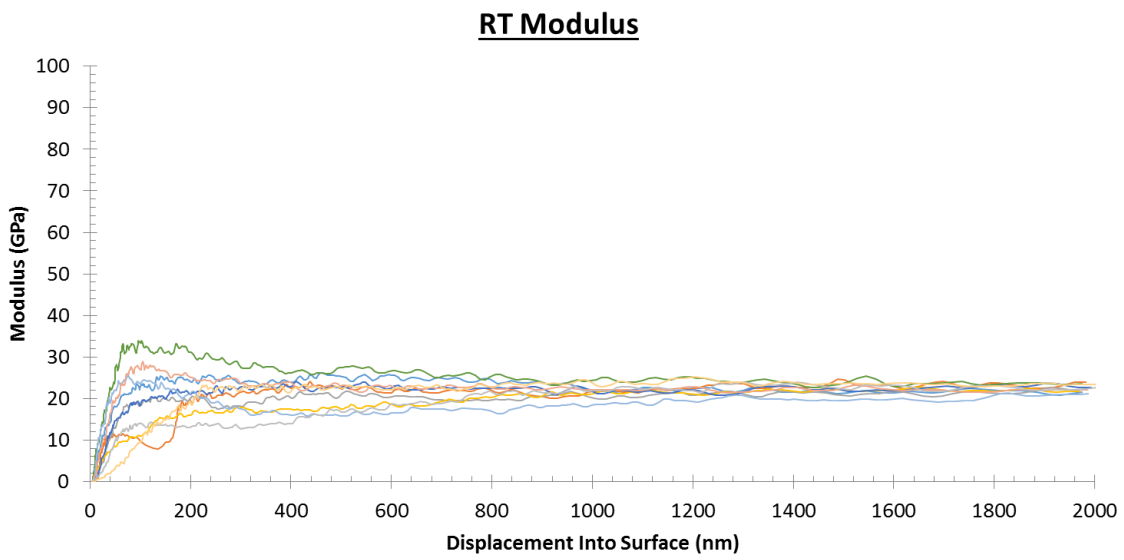

Figure 48. CHS room temperature indentation measured Young's modulus.

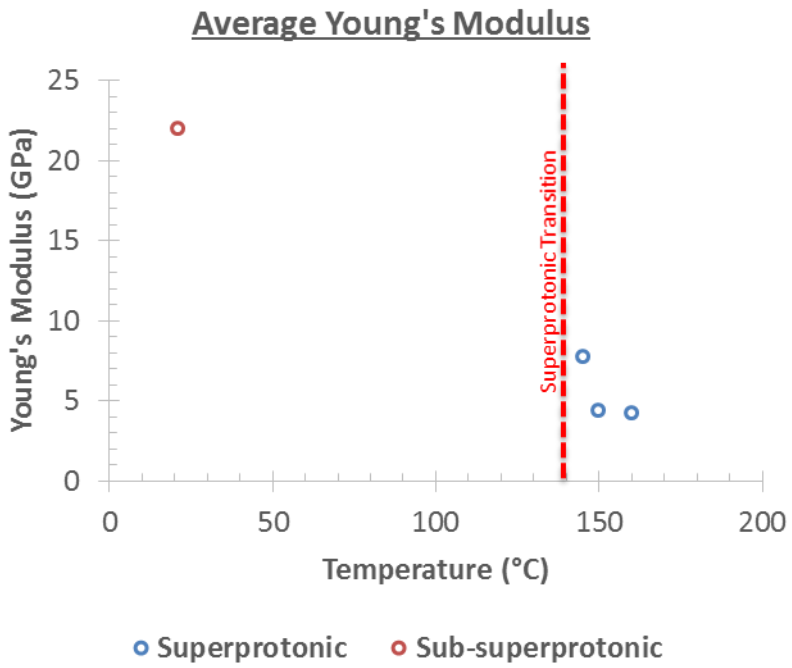

Figure 49. CHS Young's modulus shift with temperature and superprotonic phase change.

References

[1] Kislitsyn, M. N. (2009). Materials Chemistry of Superprotonic Acids. Materials Science. Pasadena, CA, California Institute of Technology. **Ph. D.:** 181.

[2] Lucas, B. N. and W. C. Oliver (1999). "Indentation power-law creep of high-purity indium." Metallurgical and Materials Transactions a-Physical Metallurgy and Materials Science **30**(3): 601-610.

[3] Oliver, W. C. and G. M. Pharr (2004). "Measurement of hardness and elastic modulus by instrumented indentation: Advances in understanding and refinements to methodology." Journal of Materials Research **19**(1): 3-20.

[4] Dolinsek, J., et al. (1986). "CS-133 AND DEUTERON NMR-STUDY OF THE SUPERIONIC TRANSITION IN CSDSO4." Solid State Communications **60**(11): 877-879.

Appendix

During uniaxial experimentation, both CDR and VDR method testing was performed on CHS at 170°C. However, when indentation testing was attempted at that same temperature, the CHS became so gooey that it began to stick to the indenter preventing any accurate measurements from being made at 170°C. To ensure a true apples to apples comparison between the indentation and uniaxial results, only the 145°C, 150°C, and 160°C uniaxial data was used for the dissertation creep analysis. In the interest of full disclosure, the uniaxial stress-strain curves obtained at 170°C are included here in Fig. 50.

To avoid cluttering the earlier discussion, most of the raw CSR indentation creep data was relocated into the appendix. Test results from indentation testing conducted at 145°C, 150°C, and 160°C with constant $\dot{P}/P$'s of 0.200, 0.020, and 0.002 s^{-1}, except those shown earlier in Fig. 43, are presented in Fig. 51-58. From these figures, one can see that constant $\dot{P}/P$ is successfully imposed producing constant h/h and p_{nom} indicating steady state is achieved by the end of each test.

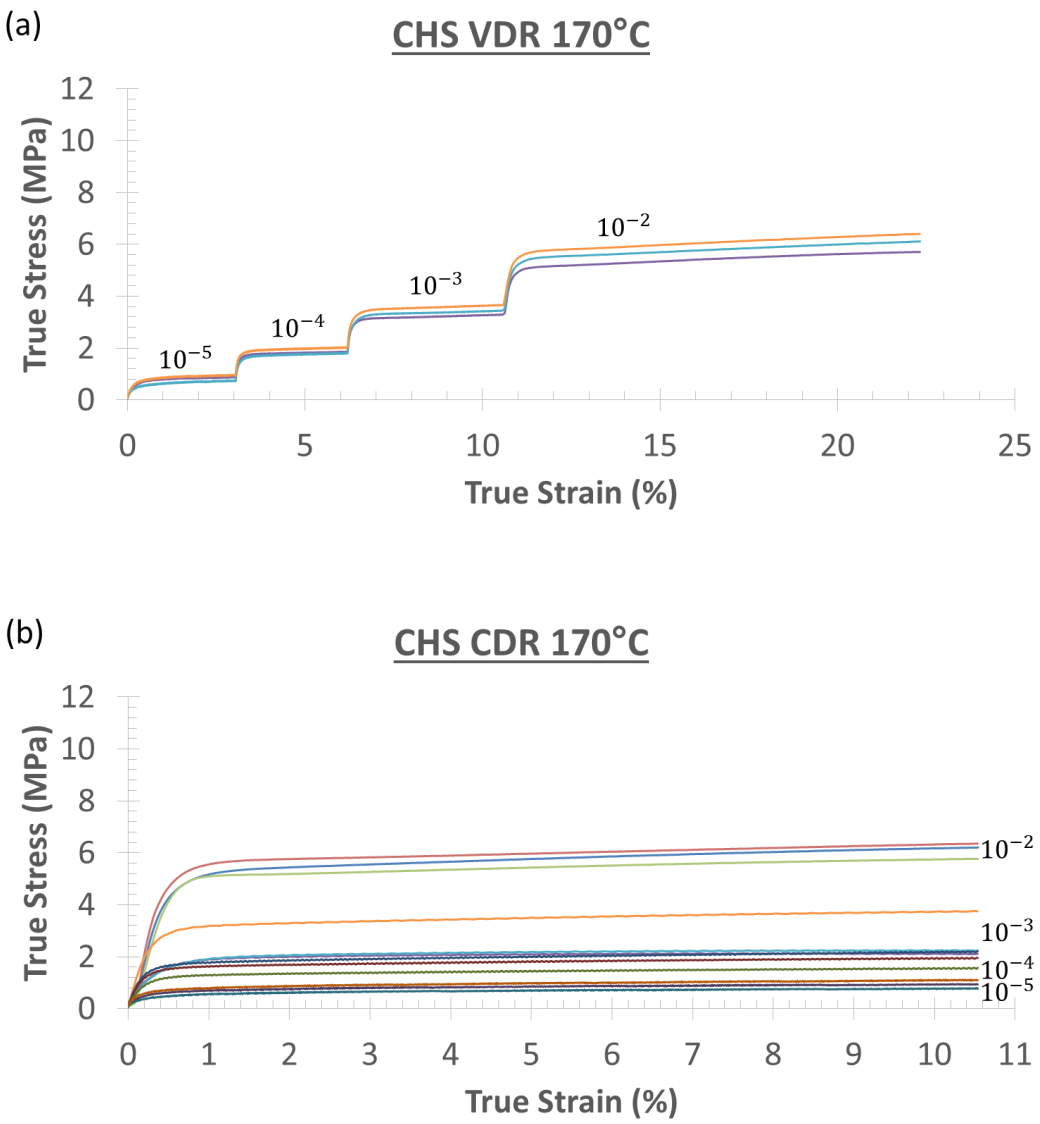

Figure 50. 170°C stress-strain curves with strain rates denoted in 1/s for (a) the VDR method and (b) the CDR method.

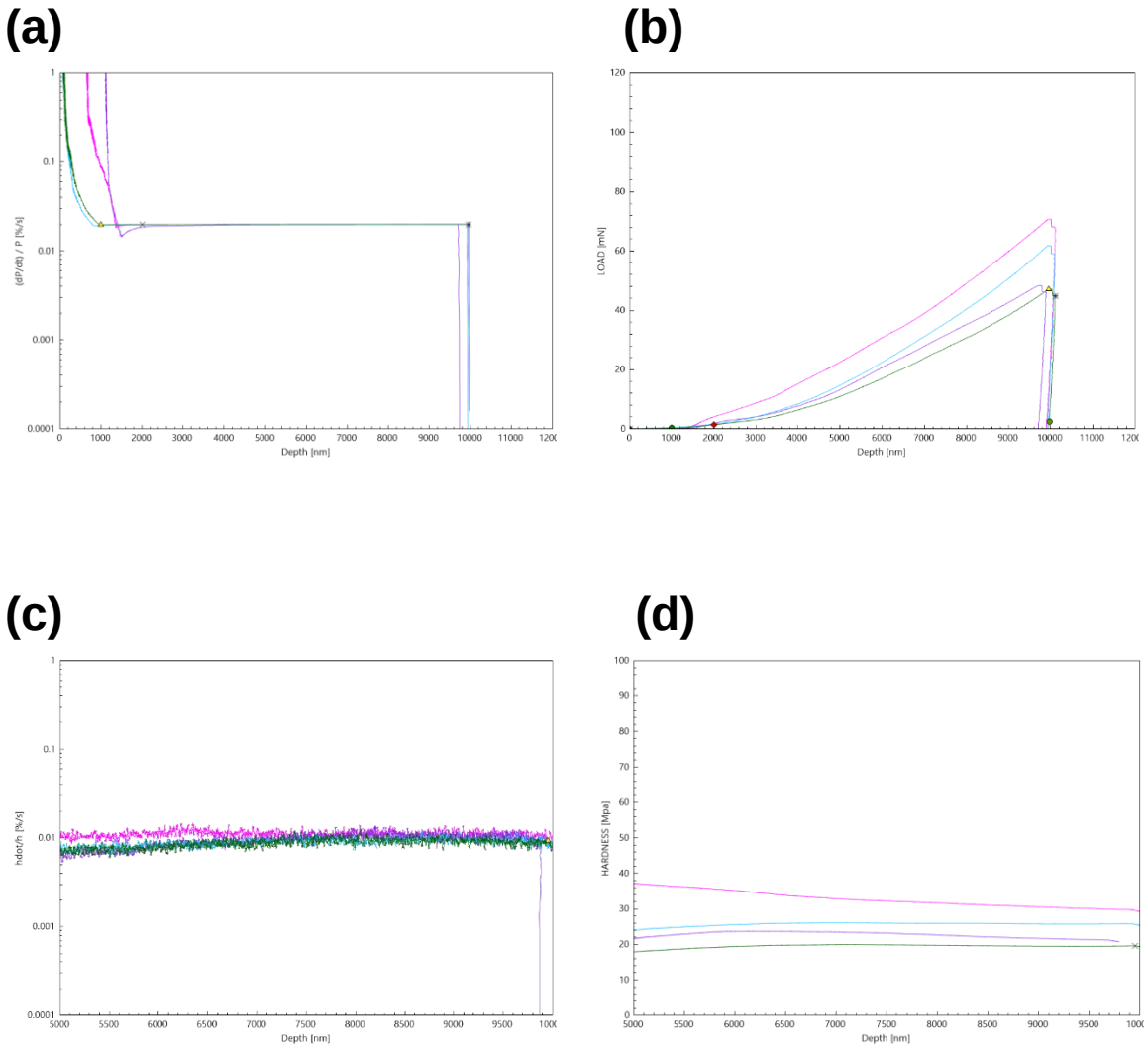

Figure 51. 145°C CSR indentation $(dP/dt)/P = 0.020\ s^{-1}$: (a) $(dP/dt)/P$, (b) load-displacement curves, (c) $(dh/dt)/h$, and (d) nominal hardness.

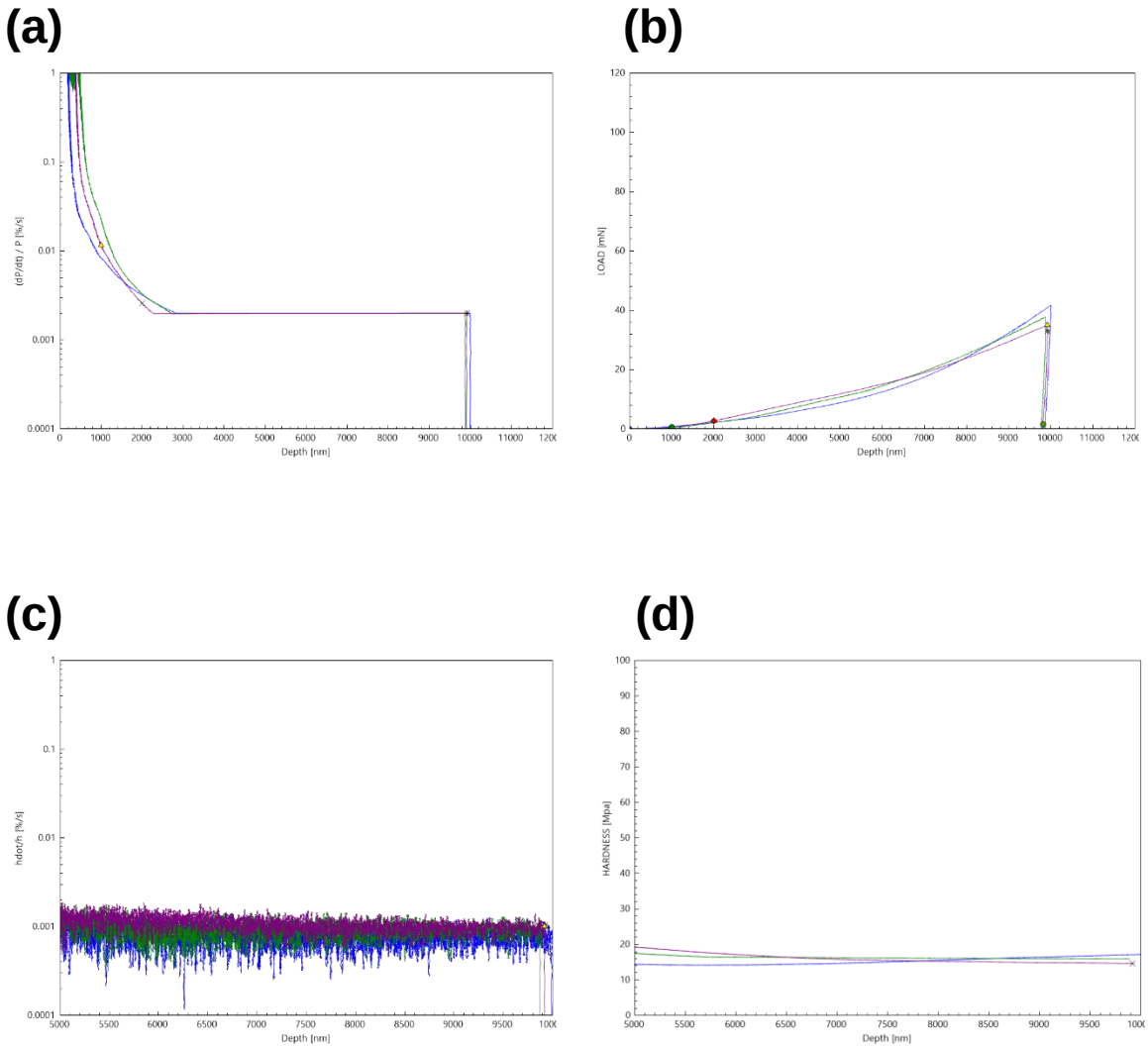

Figure 52. 145°C CSR indentation $(dP/dt)/P = 0.002\ s^{-1}$: (a) $(dP/dt)/P$, (b) load-displacement curves, (c) $(dh/dt)/h$, and (d) nominal hardness.

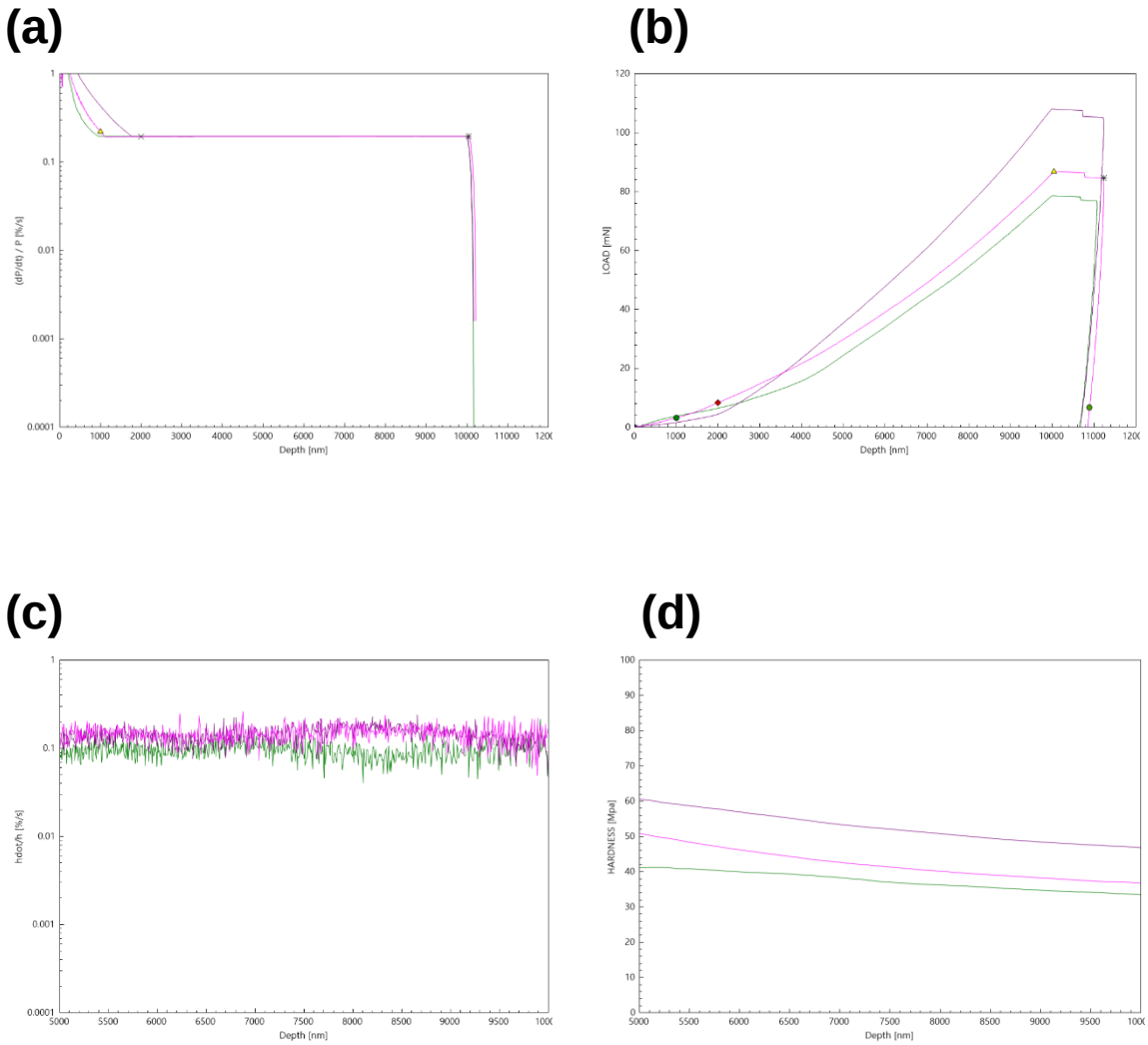

Figure 53. 150°C CSR indentation $(dP/dt)/P = 0.200\ s^{-1}$: (a) $(dP/dt)/P$, (b) load-displacement curves, (c) $(dh/dt)/h$, and (d) nominal hardness.

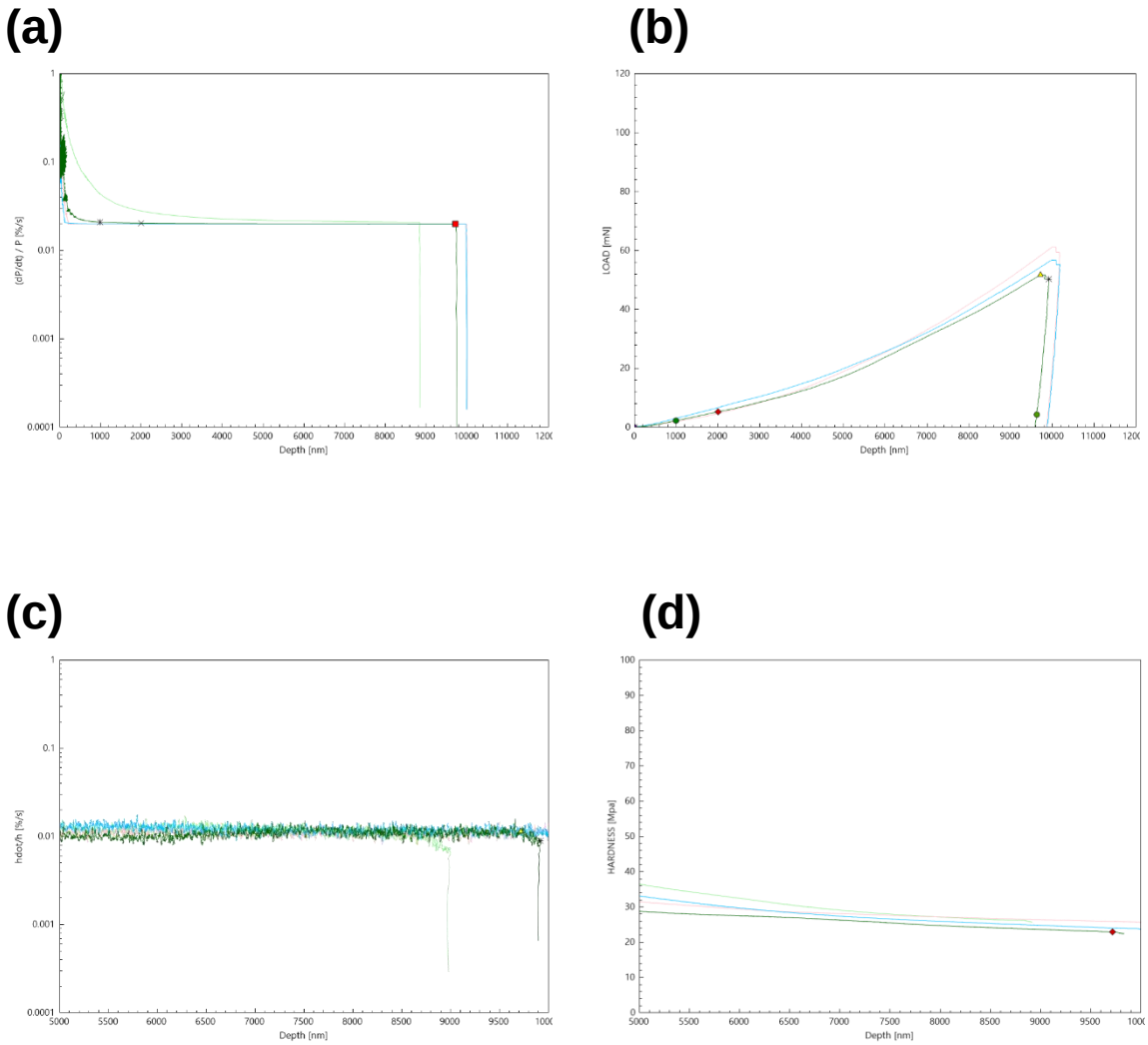

Figure 54. 150°C CSR indentation $(dP/dt)/P = 0.020\ s^{-1}$: (a) $(dP/dt)/P$, (b) load-displacement curves, (c) $(dh/dt)/h$, and (d) nominal hardness.

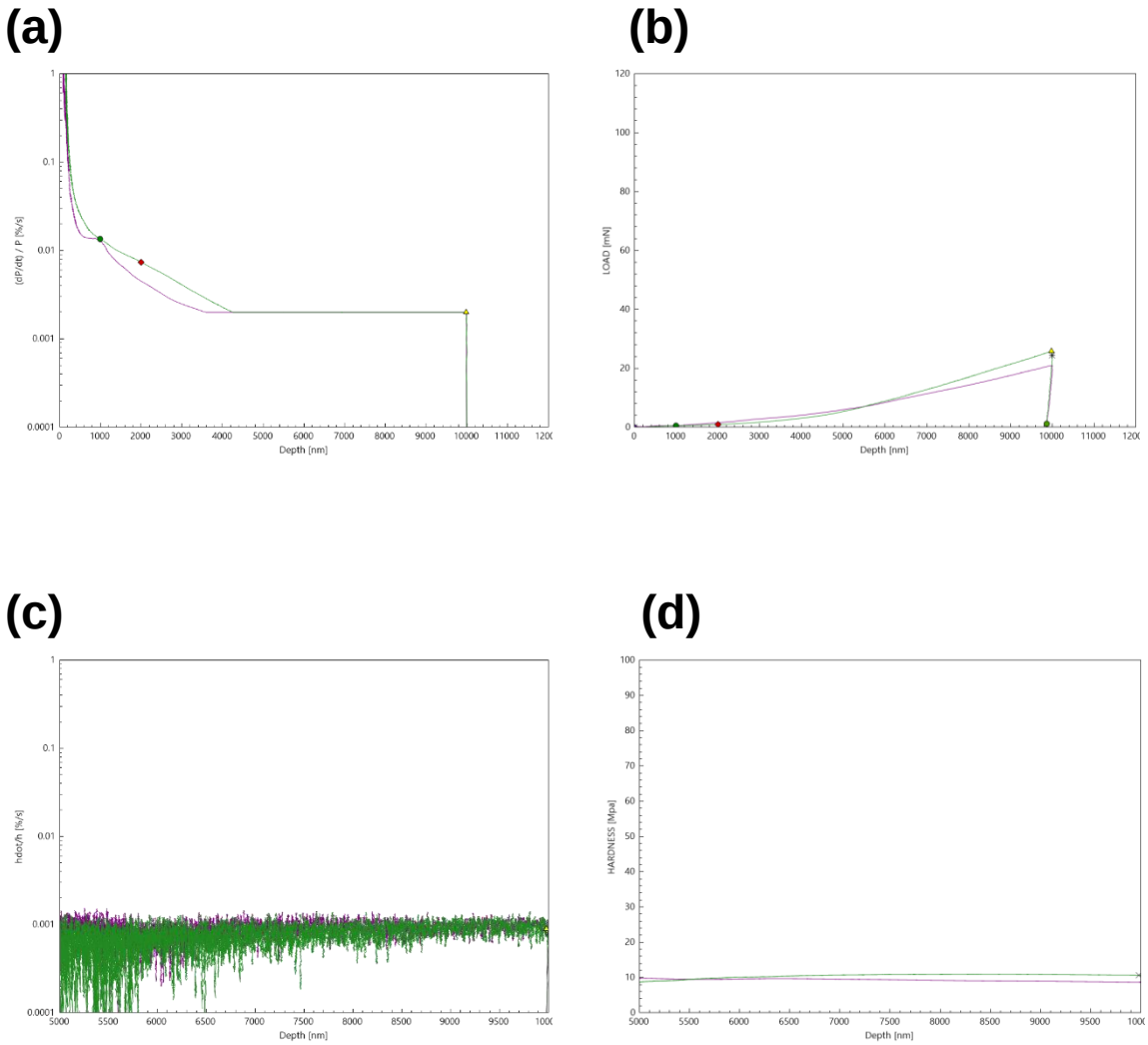

Figure 55. 150°C CSR indentation $(dP/dt)/P = 0.002\ s^{-1}$: (a) $(dP/dt)/P$, (b) load-displacement curves, (c) $(dh/dt)/h$, and (d) nominal hardness.

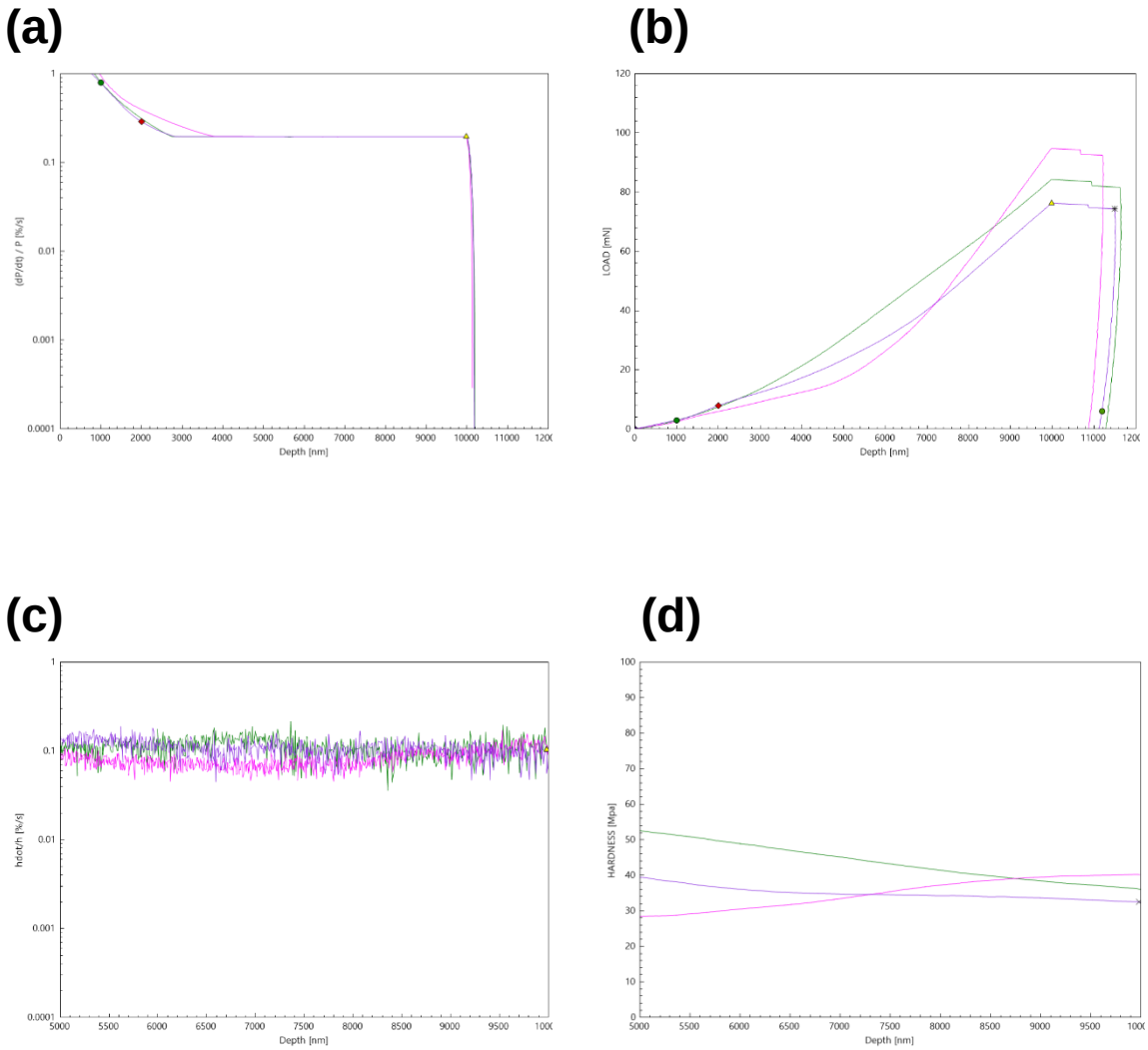

Figure 56. 160°C CSR indentation $(dP/dt)/P = 0.200\ s^{-1}$: (a) $(dP/dt)/P$, (b) load-displacement curves, (c) $(dh/dt)/h$, and (d) nominal hardness.

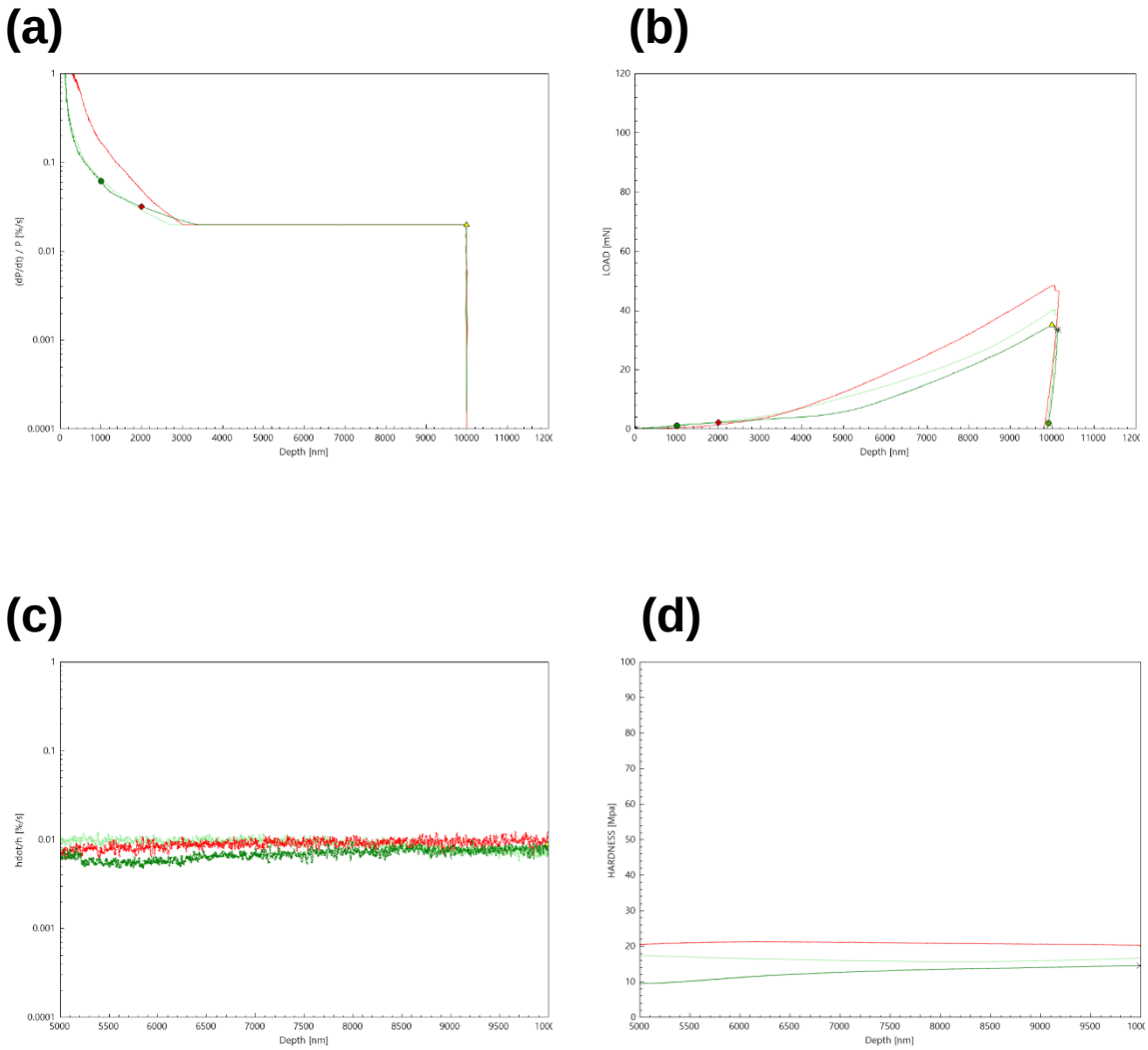

Figure 57. 160°C CSR indentation $(dP/dt)/P = 0.020\ s^{-1}$: (a) $(dP/dt)/P$, (b) load-displacement curves, (c) $(dh/dt)/h$, and (d) nominal hardness.

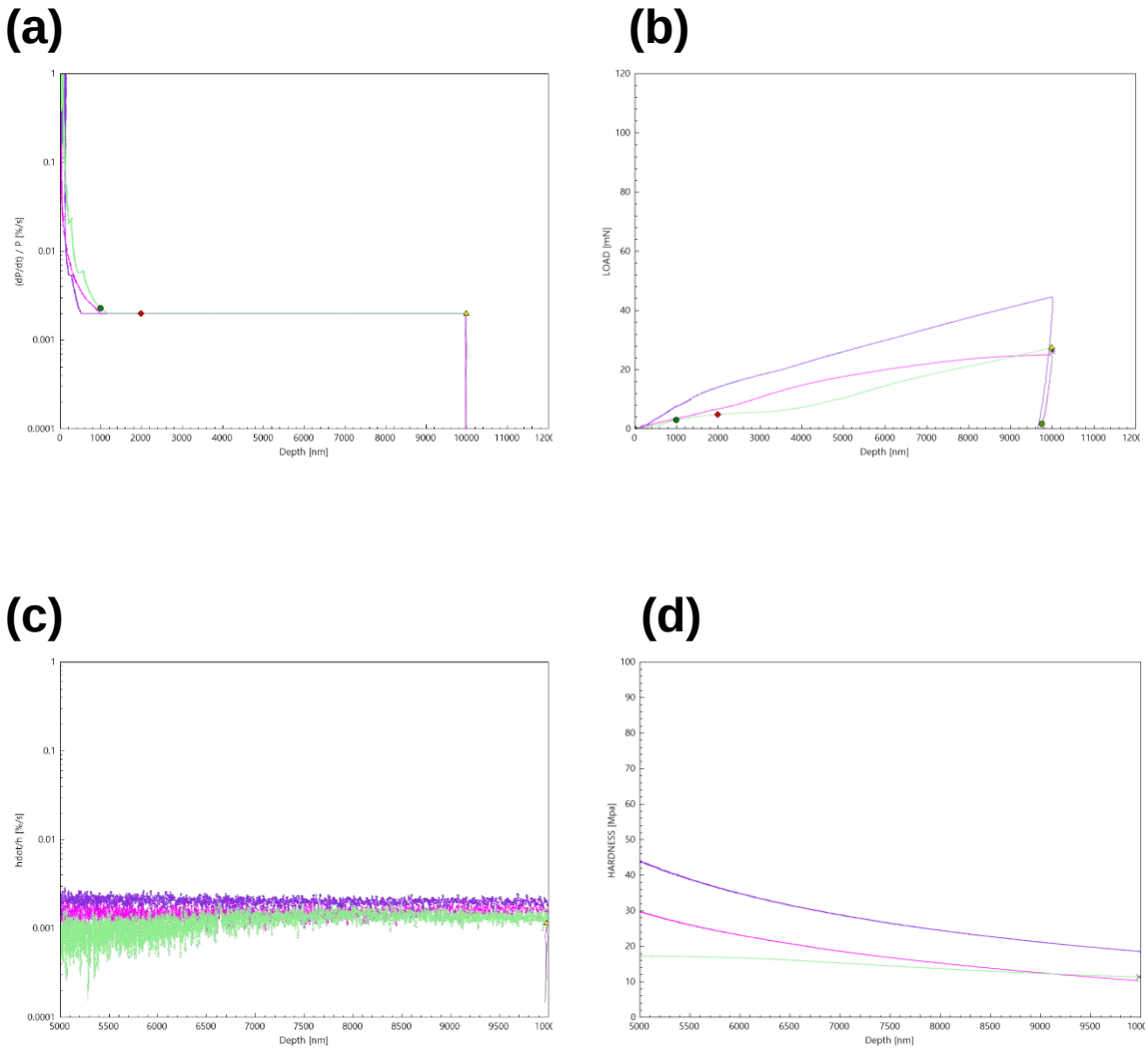

Figure 58. 160°C CSR indentation $(dP/dt)/P = 0.002\ s^{-1}$: (a) $(dP/dt)/P$, (b) load-displacement curves, (c) $(dh/dt)/h$, and (d) nominal hardness.

FINAL CONCLUSIONS

The main goal of this dissertation was to accurately characterize the dramatic shift in deformation behavior that accompanies the superprotonic shift in the solid acid model material CHS. An analysis of pre-existing literature data revealed traditional uniaxial compression testing unable to provide reliable data using typical thin disc, small aspect ratio FC specimens. To overcome this, the relatively new technique of nanoindentation was selected as an alternative because of its ability to probe only small volumes. However, nanoindentation has not typically been used for the measurement of creep and so no widely accepted approach to interpret the data currently exists. A theory of power law indentation creep governed by radial flow was therefore developed, compared with the related model from Bower's analysis, and shown to work for different axisymmetric indenter geometries and stress exponents using available experimental data. The indentation data collected and analyzed for CHS was compared with data collected from uniaxial compression tests on much larger aspect ratio CHS specimens fabricated for this exact purpose. Because of the lack of microstructural data in the literature, definitive identification of the underlying creep mechanism was not possible; however, the obtained mechanical data does provide useful insight into CHS's mechanical behavior as well as implications for the continued use of nanoindentation in measuring steady state creep behavior.

CHS Mechanical Behavior

(1) Creep appears to be a serious problem under compressive loading for CHS. This problem most likely extends to all superprotonic solid acids to varying extents.

(2) CHS's stress exponent $n \cong 3.5 - 3.6$ and relative activation energy $Q \cong 1eV = 100\,kJ/mol$, measured by both uniaxial compression and nanoindentation, are consistent with the traditional creep interpretation of a dislocation based mechanism. Whether or not this interpretation, based on creep in metals, is valid for CHS remains unclear. What is clear though is that the measured data directly contradict the results of Kislitsyn which suggested grain boundary sliding as the dominate creep mechanism.

(3) Elastic modulus was found to decrease by over a factor of five when heated into the superprotonic phase from room temperature. This suggests elastic deformation may also need to be taken into account during the design of solid acid FCs.

Steady State Theory of Indentation Creep

(1) A nonlinear, steady state creep model of spherically symmetric radial flow provides a relatively simple, closed form approximation for indentation power law creep. This relation's general form is as follows:

$$\frac{\dot{h}}{a} = \alpha \left(\frac{3\bar{p}}{2n}\right)^n.$$

(2) When compared with Bower's related numerical indentation creep model, both models are found to provide accurate predictions of uniaxial results from indentation data suggesting both that their underlying steady state creep law is valid and that radial flow dominates indentation creep for stress exponents $n = 1 - 7{,}8$.

(3) From the various experimental datasets available, nanoindentation appears able to successfully probe both time-independent and time-dependent properties simultaneously using small volumes.

VITA

Ryan S. Ginder was born November 25, 1988. He lived in both New York and Virginia as a young child until moving to Memphis, TN in the 2nd grade where he primarily grew up. After graduating from Houston High School in 2007, Ryan attended Northwestern University graduating with his Bachelor's degree in Materials Science and Engineering in 2011. During his tenure in graduate school, Ryan has served as the vice-president of the Materials Research Society's University of Tennessee student chapter and was awarded the National Defense Science and Engineering Graduate Fellowship.